THAYER SCHOOL OF ENGINEERING
DARTMOUTH COLLEGE

ICE RESEARCH

Agenda and Abstracts

for the

15th Annual

Advisory Board Meeting

of the

Ice Research Program

at Dartmouth College

June 3 and 4, 1997

IRL Abstracts
Table of Contents

Table of Contents (continued)

AGENDA

15TH ANNUAL ICE RESEARCH ADVISORY BOARD MEETING

Thayer School of Engineering, Dartmouth College
Hanover, New Hampshire

3 and 4 June 1997

Thayer School Conference Room

Tuesday, June 3

		CLOSED SESSION
8:00	--	Coffee and Fruit Juice
8:15	--	Welcoming Remarks Dean Elsa Garmire
8:30	--	Overviews: Progress and Plans • Ice Physics (Ian Baker and Victor Petrenko) • Ice Mechanics (Bill Hibler and Erland Schulson)
9:15	--	Discussion and Comments by Advisory Board
10:00	--	COFFEE BREAK
		OPEN SESSION
GUEST LECTURE 10:30	--	*"In-Situ* Measurements of Stresses in Pack Ice" Jackie Richter-Menge, USA-CRREL
		ICE MECHANICS
11:30	--	"On Modeling the Flow and Fracture of Cracked Sea Ice" William D. Hibler, III
12:00	--	LUNCH

Tuesday, June 3

ICE MECHANICS (continued)

1:30	--	"Flow and Fracture of Ice on Scales Large and Small" Erland Schulson
1:50	--	"The Effect of Pre-Existing Flaws Upon the Compressive Fault Pattern in Columnar Ice" Daniel Iliescu and Erland Schulson
2:10	--	"The Brittle Compressive Failure of Columnar S2 Ice: A Comparison of Fresh-Water and Salt-Water Ice" Eric Gratz and Erland Schulson
2:30	--	"The Ductile Compressive Strength of Columnar Saline Ice: A Comparison of Behavior Under Proportional and Conventional Triaxial Loading" Jeff Melton and Erland Schulson
2:50	--	"The Brittle-to-Ductile Transition in Ice Under Compression: The Effect of Temperature" Suogen Qi and Erland Schulson
3:10	--	COFFEE BREAK
3:30	--	"Effect of Confinement on Brittle Indentation Failure of Ice" Johan Grape and Erland Schulson
3:50	--	"Brittle Indentation Failure of Ice" Sang-Ryong Ko
4:10	--	"A New Method to Achieve Increased Hydrostatic Loading Using the Multiaxial Testing System" Jeff Melton and Erland Schulson
4:30	--	"The Deformation of Cubes of Frozen Soil Under Triaxial Compression" Eric Gratz and Erland Schulson
4:50	--	"Inertial Oscillations in Interacting Pack Ice" W.D. Hibler III and Petra Heil
5:10	--	Tour of the IRL Facilities
5:40	--	ADJOURN

****

6:30	--	Cocktails and dinner for advisory board, faculty and students -- Dowd's Country Inn, Lyme, New Hampshire

Wednesday, June 4 — **OPEN SESSION**

8:15	--	Coffee and Fruit Juice

ICE PHYSICS

8:30	--	"Effect of Electric Fields on Adhesion of Ice to Metals" Victor Petrenko
8:50	--	"Physical Mechanisms of Ice Adhesion" Victor Petrenko
9:10	--	"The Effect of HCL on the Mechanical Properties of Ice" Daniel Cullen and Ian Baker
9:30	--	"X-Ray Topography of Notched Ice" Xiaohong Hu and Ian Baker
9:50	--	"Study of Photoplastic Effect in Ice" Niyaz Khusnatdinov and Victor Petrenko
10:15	--	COFFEE BREAK

CLOSED SESSION

10:30	--	Wrap-up Discussion
12:00	--	Meeting Adjourned

On Modeling the Fracture and Flow of Cracked Sea Ice

W. D. Hibler, III
Thayer School of Engineering
Dartmouth College
Hanover, NH 03755

Sea ice on the large scale is characterized by leads and ridges which typically have a given orientation. Because of various flaws we would expect that the ice will form oriented leads and ice thickness characteristics which control the heat and moisture fluxes into the atmosphere. Prediction of these oriented leads, ridges and slip lines is relevant to understanding the role of ice mechanics in global climate change as the leads play a significant role in the ice thickness distribution.

To examine the effects of fracture based failure on lead formation a model for the dynamical treatment of leads (Hibler and Schulson, 1997) and oriented flaws in sea ice has been developed. The basic concept is to consider one or more oriented weak leads in thick ice and then self consistently solve the non linear equations to obtain the failure stresses for this system under biaxial loading numerical experiments. Considering a random set of oriented leads occupying the same region, the theory predicts a preferred failure of particular leads with intersection angles ranging from 18-36° for low confinement ratios $R = \sigma_{xx}/\sigma_{yy}$ less than about 0.06 (see Figure 1). For higher confinement ratios up to about 0.3, the failure is much more weakly dependent upon lead orientation with the most likely failure occurring at intersection angles of about 80°.

Using this oriented lead model as a framework for anisotropic response of an element of sea ice, numerical experiments are currently underway to determine failure patterns for an oriented flaw imbedded in stronger pack ice. Initial results involving thicker ice both with and without tensile stress bill be presented. This presentation will also include an analysis of the essential physics of the failure accounting for certain oriented leads preferentially occurring in a single stressed element (see Figure 1).

Failure vs Flaw Angle for different Confinement Ratios

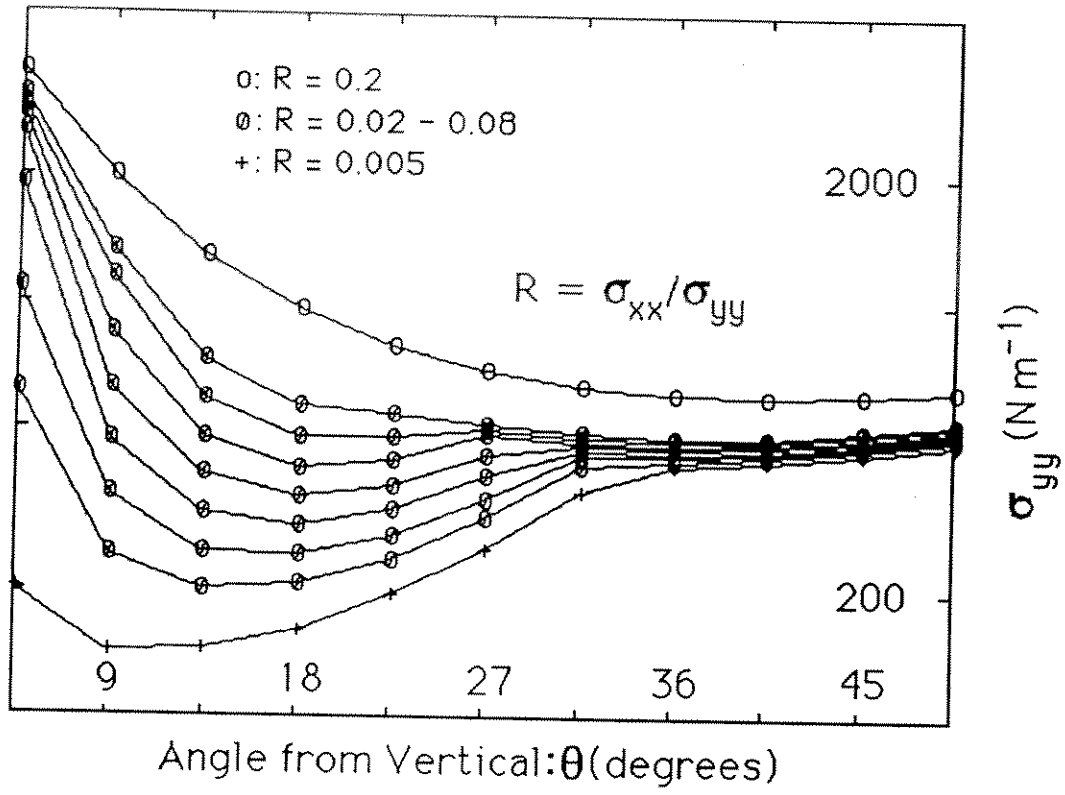

Figure 1: Failure stress for two symmettric intersecting leads intersecting at angle 2θ for different stress confinement ratios $R = \sigma_{xx}/\sigma_{yy}$. The leads each comprise 0.4% of the area and have a strength equal to 1% of the thick ice strength P which is equal to 10^5N m^{-1}.

The effect of pre-existing flaws upon the compressive fault pattern in columnar ice

by Daniel Iliescu and E.M. Schulson

Thayer School of Engineering
Dartmouth College

The goal of the present paper is to provide a qualitative description of the local and long range interactions between the stress fields induced by an array of through-thickness "randomly" oriented initial flaws. These interactions, once understood, will lead to the prediction of crack growth and, on a larger scale, the dynamics of the faulting patterns in sheets of columnar ice.

Uniaxial and biaxial compression experiments were conducted at -10° C on orthotropic, S2 fresh-water columnar ice which contained a random array of precursor cracks. Although the focus of these experiments was on the brittle behavior of ice, two tests involving ductile failure were also performed for a better understanding of the aspects that may influence the crack pattern.

Specimens were milled to a nominal size of 6 x 6 x 1 inches (152.4 x 152.4 x 25.4 mm) and contained 16 through-thickness teflon inserts, each of 0.5 inches (12.7 mm) width. The thickness of the teflon inserts was 0.001 inches (0.025 mm), sufficiently small to avoid the alteration of the local stress fields. The distribution pattern of the initial flaws is shown in figure 1.

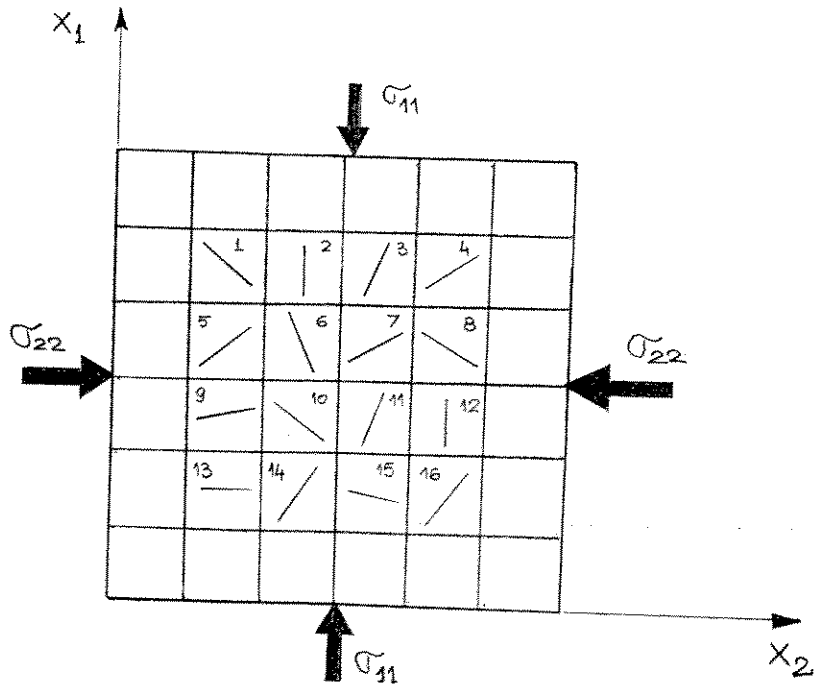

Fig. 1

A sketch of the growing device is shown in figure 2.

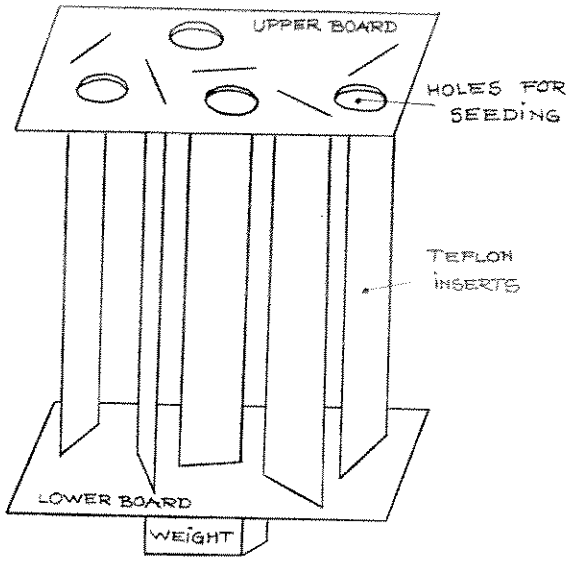

Fig. 2

Pucks of columnar ice of 13 inches (330.2 mm) diameter and approximately 10 inches (254 mm) thickness were grown using unidirectional cooling. A 25-liter tank was placed in a room at -40° C and filled with filtered tap-water, equilibrated to 0° C. The growing device was mounted on top of the tank and then the water was seeded with 0.6 mm diameter snow powder in order to minimize the grain size. The sides of the tank were insulated and heated with an electric blanket in order to avoid any radial heat transfer. The temperature between the insulation and the tank wall was maintained at 0° C. The pucks were removed from the tank after 3 days.

The specimens were cut out of the trimmed puck so that the columns were parallel to the thickness. The out of plane C-axis angle was contained within 20° of the horizontal and the grain size ranged from 1.5 mm at the top of the puck to about to 5 mm at the bottom.

The samples were mounted on the testing machine in a vertical position so that the stresses σ_{11} and σ_{22} were perpendicular to the columnar shaped grains (Fig. 3). The sample orientation was as shown in figure 1 for the majority of the tests. Two tests (# 16 and 17) were performed after rotating the sample 90° CCW.

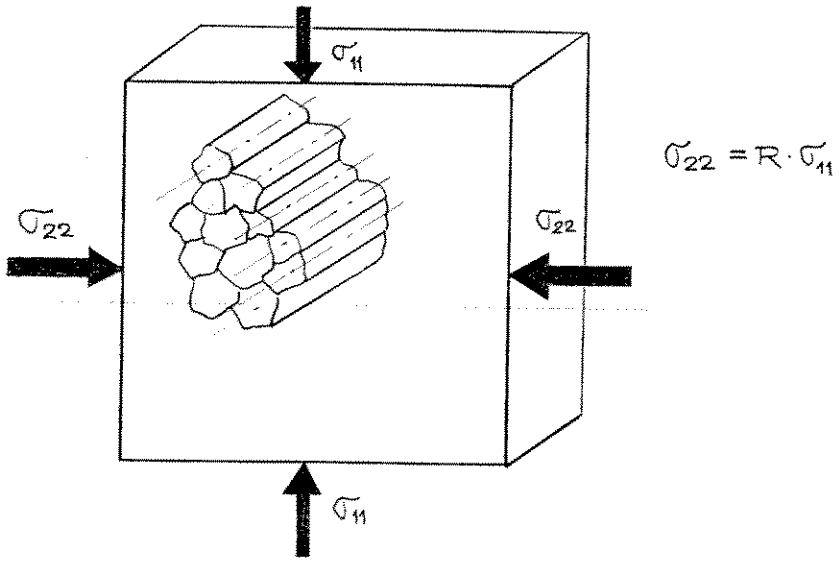

Fig. 3

In most of the tests sand-paper was applied on the loading surfaces in order to confine the displacements of these surfaces and minimize the influence of local flaws upon the main faulting pattern. In some cases, tests were run without sand-paper for comparison.

The loading cycle was of triangular shape with the unloading path performed at the same strain rate as the loading path. For comparison, monotonic as well as pulse loading tests were performed.

In the case of pulse loading tests, besides strain rate and confinement ratio, the amplitude of the initial loading cycle was modified. The amplitudes of the subsequent cycles increased by integer multiples of the amplitude of the initial cycle until failure occurred (see table 1).

In all the biaxial tests proportional loads were applied, i.e. the ratio of σ_{11} and σ_{22} was maintained constant during each test. Different combinations of strain rate and confinement ratio were sought to ensure the brittle behavior of the specimen.

Results:

For each loading step the dependencies of stresses (σ_{11} and σ_{22}) and strains (ε_{11} and ε_{22}) vs. time and stresses vs. strains were recorded. Also pictures of the cracking pattern were taken at the end of each loading step. Later these pictures were used to recreate the development of the faulting pattern for each sample. Finally, detailed pictures of each sample after failure were taken.

Initially a dependence between the inclination angle of the main fault and the degree of confinement ($R=\sigma_{22}/\sigma_{11}$) was sought. As the experiments went on, and the development of the faulting pattern was studied, it became clear that a simple relationship between the inclination angle and the degree of confinement could not be achieved. Additional factors had to be taken into account.

Due to the variations in the strain rate, degree of confinement and orientation of the teflon insert pattern, various fault patterns were obtained. Although a quantitative influence of each factor mentioned above upon the fault pattern is fairly difficult to establish, a qualitative understanding of the mechanism has been achieved.

A close study of the pictures of the intermediate loading steps revealed that in spite of the difference in loading (uniaxial vs. biaxial), strain rates and degree of confinement, some tests have a common initial fault linking the same teflon inserts in a similar manner. Figures 5 through 8 show, in a sequential manner, the nucleation and the growth of this fault for four different tests (please note that the pictures are mirrored).

Two other important observations were also made.

First, the fault angle for the biaxial compression did not show a systematic variation over a confinement range of 5% to 15% (strain rates for these tests ranged between $4*10^{-3}$ and $4.1*10^{-2}$ s^{-1}). See figures 9 through 13. Note that in almost all the cases the main fault links directly inserts number 1, 5, 10 and 15.

Secondly, when the position of the initial flaw pattern with respect to the direction of the maximum compressive stress was changed (rotated 90° CCW, tests 16 and 17) a totally different fault pattern was obtained (Fig. 14).

The above mentioned observations led us to the conclusion that the arrangement of the initial flaws and the interaction process between these flaws have a much greater influence upon the fault pattern than the confinement ratio (R) and the strain rate ($\dot{\varepsilon}$). This means that the final fault pattern will be much more sensitive to modifications in the arrangement of the initial flaws than to R and $\dot{\varepsilon}$.

The following mechanism was proposed in order to give a qualitative description of the dynamics of the fault pattern:

a) Under a load characterized by a certain combination of strain rate and initial amplitude, a group of 2, 3, or 4 adjacent teflon inserts, due to their specific relative position will exhibit a stronger influence upon the local stress state than any other group of adjacent initial flaws.

b) The favorable orientation of these initial flaws, with respect to the loading characteristics, will alter the local stress state, triggering early flaws along approximately the same direction . These early flaws will grow later into a stronger local flaw.

c) This flaw will grow bigger than the actual "nucleation" zone which generated it and will enter the adjacent zones of influence. Along with the increase of stress more nucleation zones will appear, causing a

greater interaction between the extended cracks and other inserted or local flaws. This interaction will give the final shape of the failure pattern in accordance to the applied stresses.

An important observations is that the "early" cracks are not triggered by the wing cracks developed at the tips of the inserted flaws, but they appear independently in a certain zone of the region delimited by the group of initial flaws. Later, these "early" cracks will grow and interact with the ones generated by the wing cracks linking together two or more inserts. The proposed mechanism assumes that the "early" cracks will nucleate on the grain boundaries, in a zone where the superposed stress fields generated by all adjacent inserted flaws yield a path of high shear stress. A sketch of this mechanism is shown in figure 4.

A mode II, shear stress driven crack model is assumed in the nucleation of the "early" cracks, since all the normal stresses are acting to close the crack.

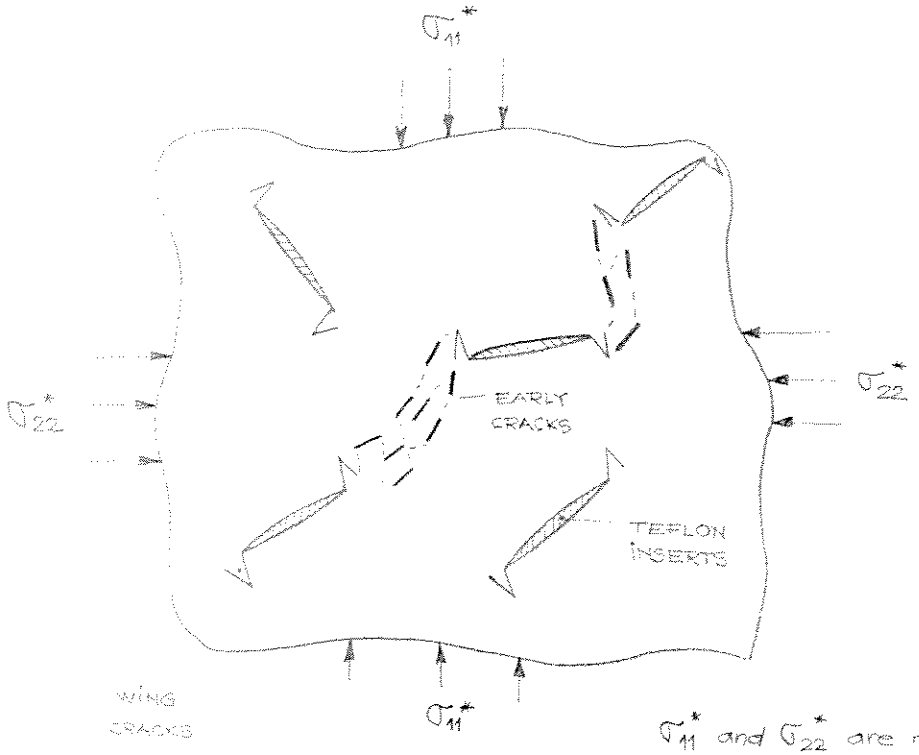

Fig. 4

σ_{11}^* and σ_{22}^* are normal far field stresses

$\sigma_{11}^* \approx \sigma_{11}$

$\sigma_{22}^* \approx \sigma_{22}$

References:

1. E.M. Schulson and O.Y. Nickolayev, Failure of Columnar Saline Ice Under Biaxial Compression: Failure Envelopes and Brittle-to-Ductile Transition, Journal of Geophysical Research, Vol. 100, No. B11, pp. 22,383-22,400, November 1995.

2. E.M. Schulson and S.E. Buck, The Ductile-to-Brittle Transition and Ductile Failure Envelopes of Orthotropic Ice Under Biaxial Compression, Acta metall. mater. Vol. 43, No.10, pp. 3661-3668, 1995.

3. David Broek, Elementary Engineering Fracture Mechanics, Noordhoff International Publishing, Leyden, 1974

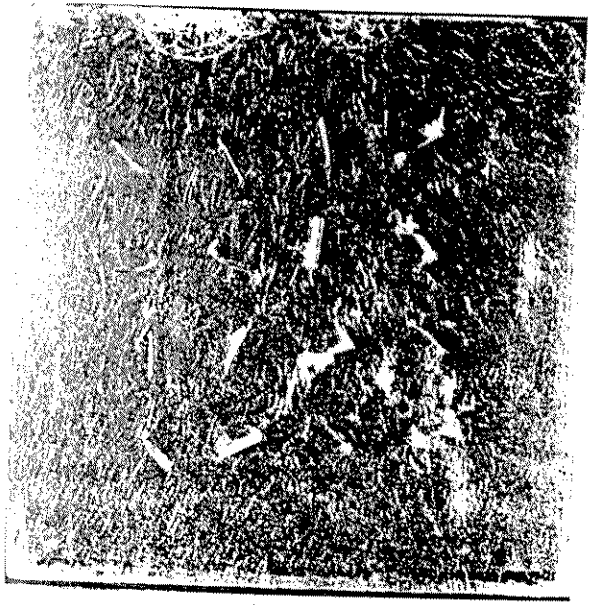

1.

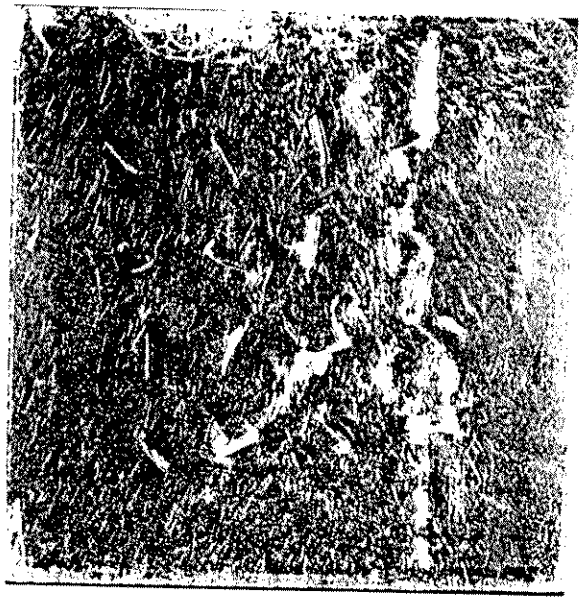

2.

3.

TEST 1 , UNIAXIAL
(BRITTLE)

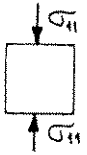

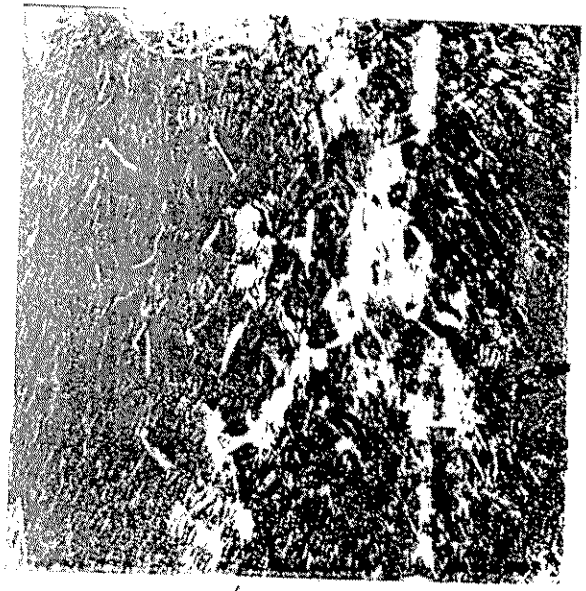

4.

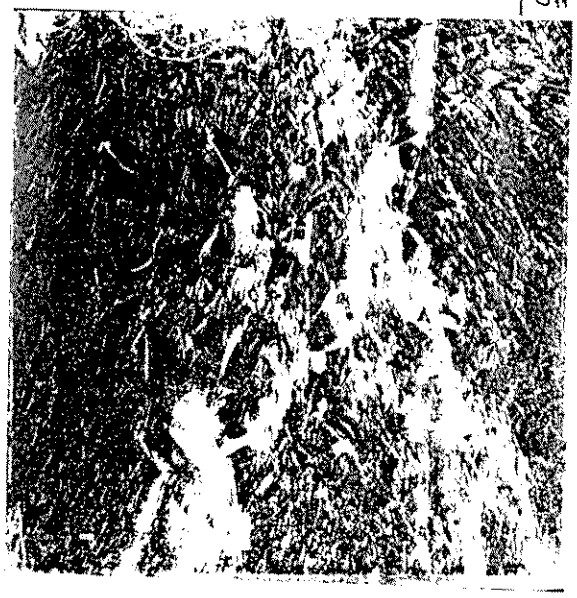

5.

6.

Fig. 5

1.

2.

3.

TEST 2, BIAXIAL
(DUCTILE)

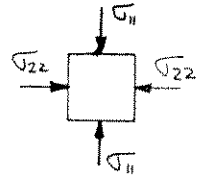

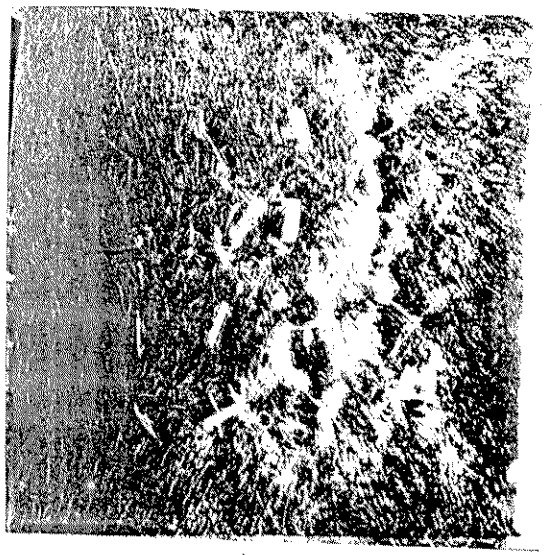

4.

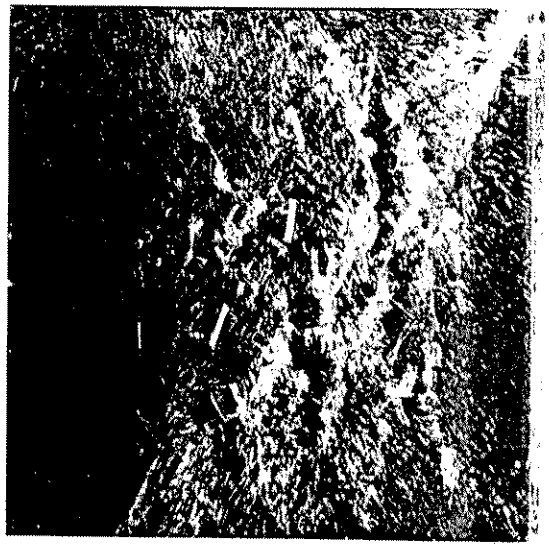

5.

6.

Fig. 6

1.

2.

3.

TEST 3, BIAXIAL
(DUCTILE)

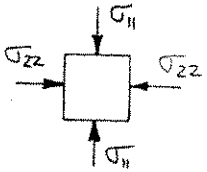

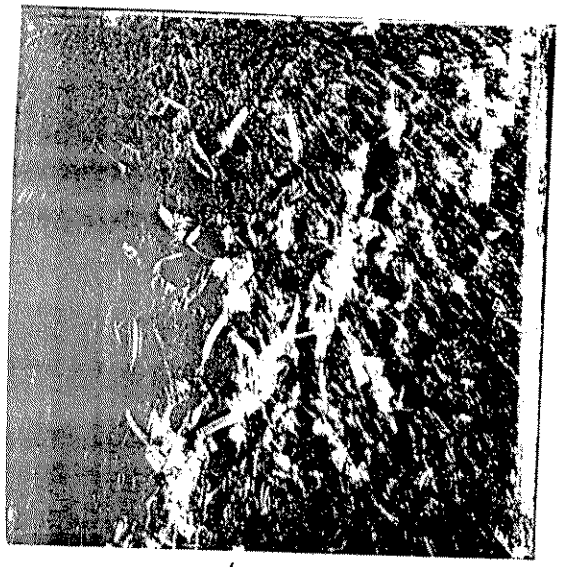

4.

5.

6.

Fig. 7

1.

2.

3.

TEST 4, BIAXIAL
(BRITTLE)

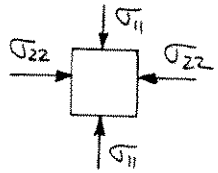

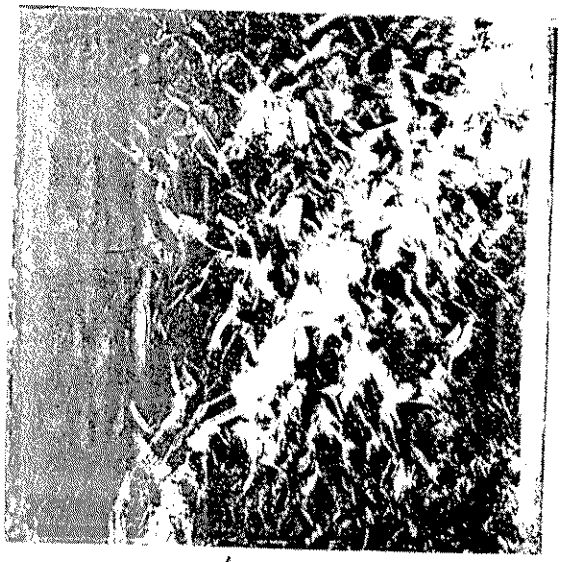

4.

5.

6.

Fig. 8

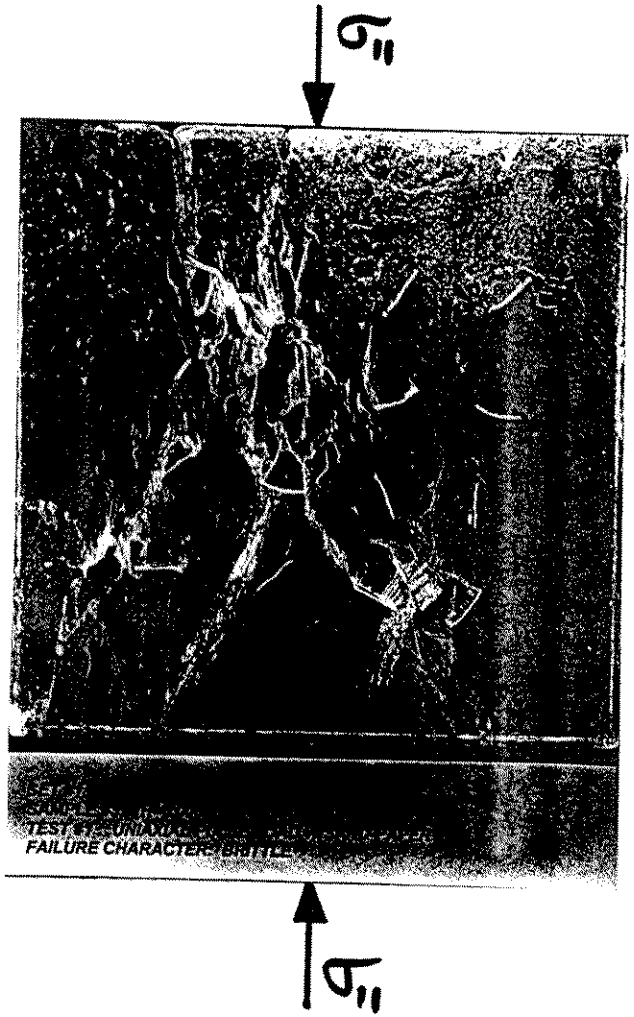

$\dot{\varepsilon} = 4 \cdot 10^{-3}$

$R = 0$

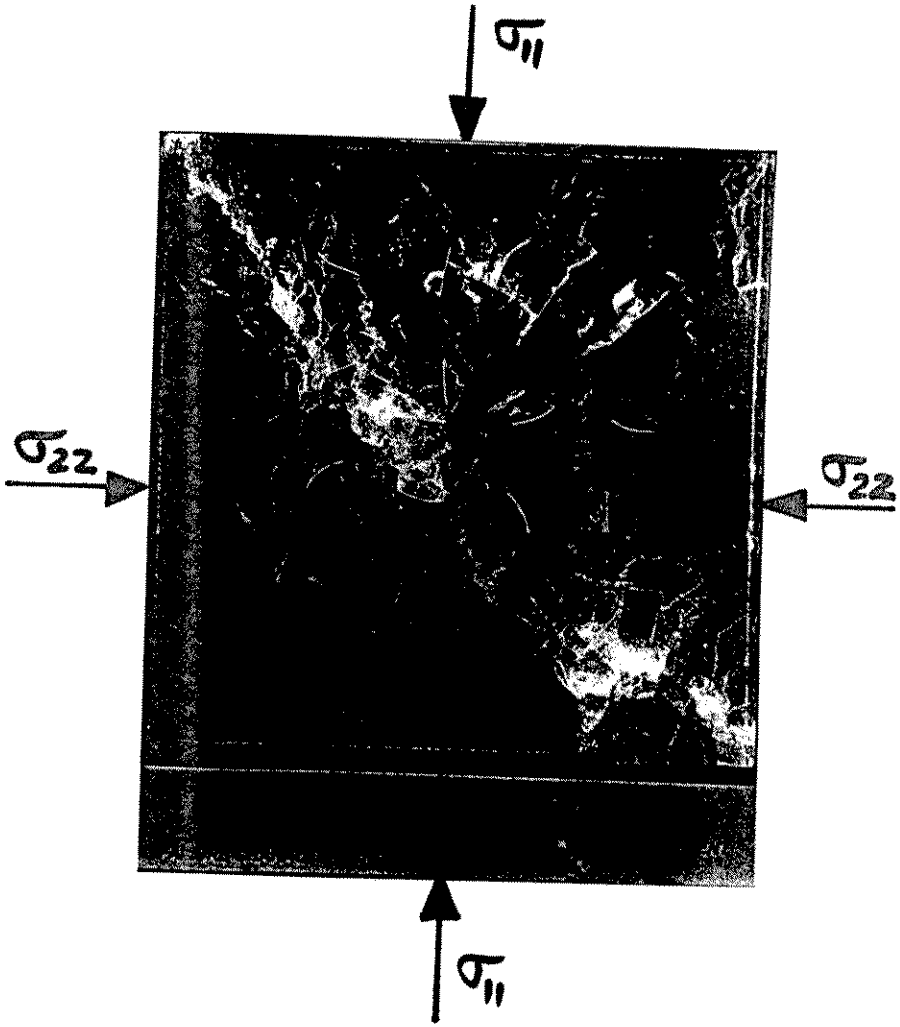

$\dot{\varepsilon} = 4 \cdot 10^{-2}$

$R = 14.5\,\%$

Fig. 9

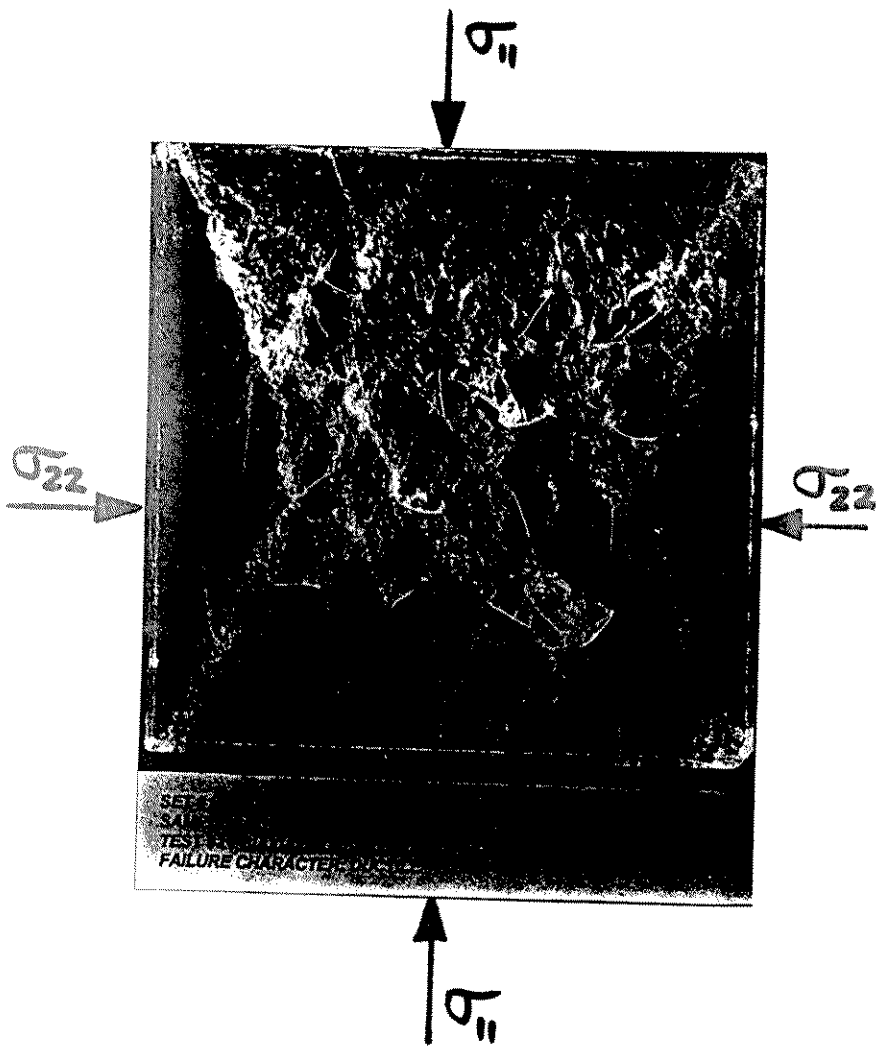

$\dot{\varepsilon} = 4 \cdot 10^{-3}$

R = 5.6%

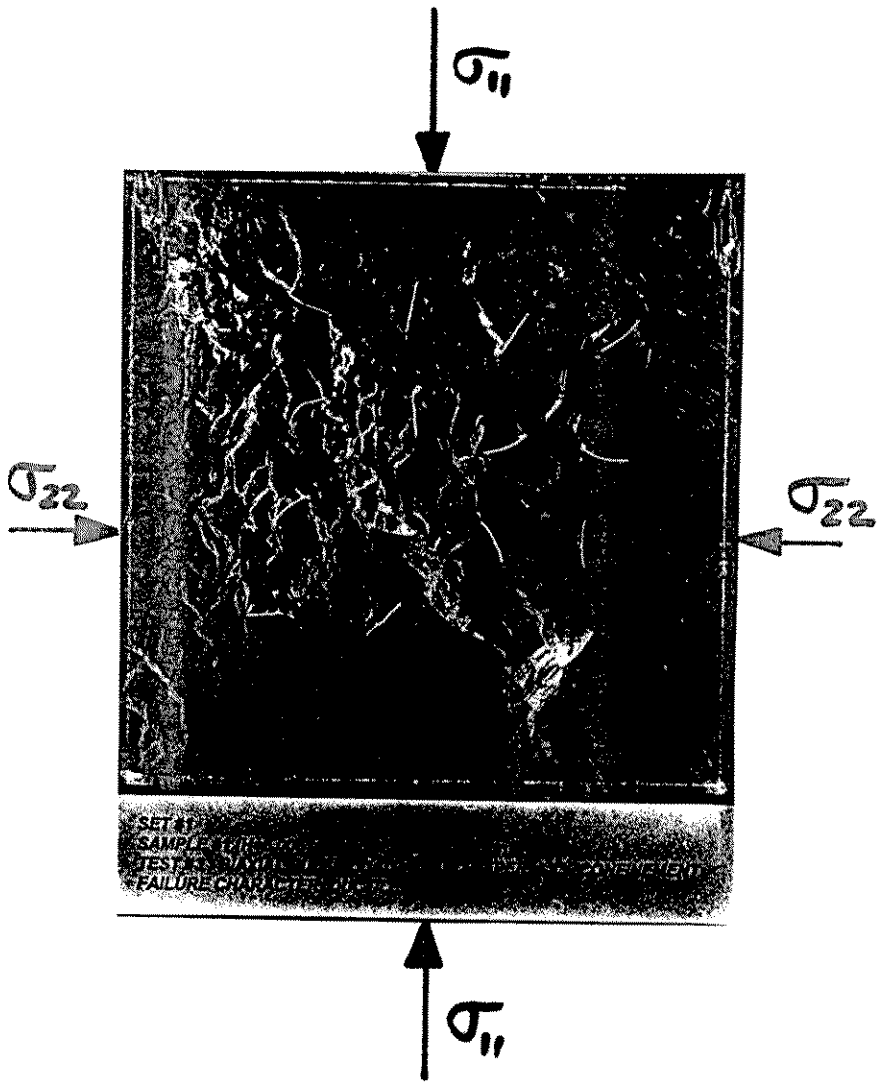

$\dot{\varepsilon} = 8 \cdot 10^{-3}$

R = 6.7%

Fig. 10

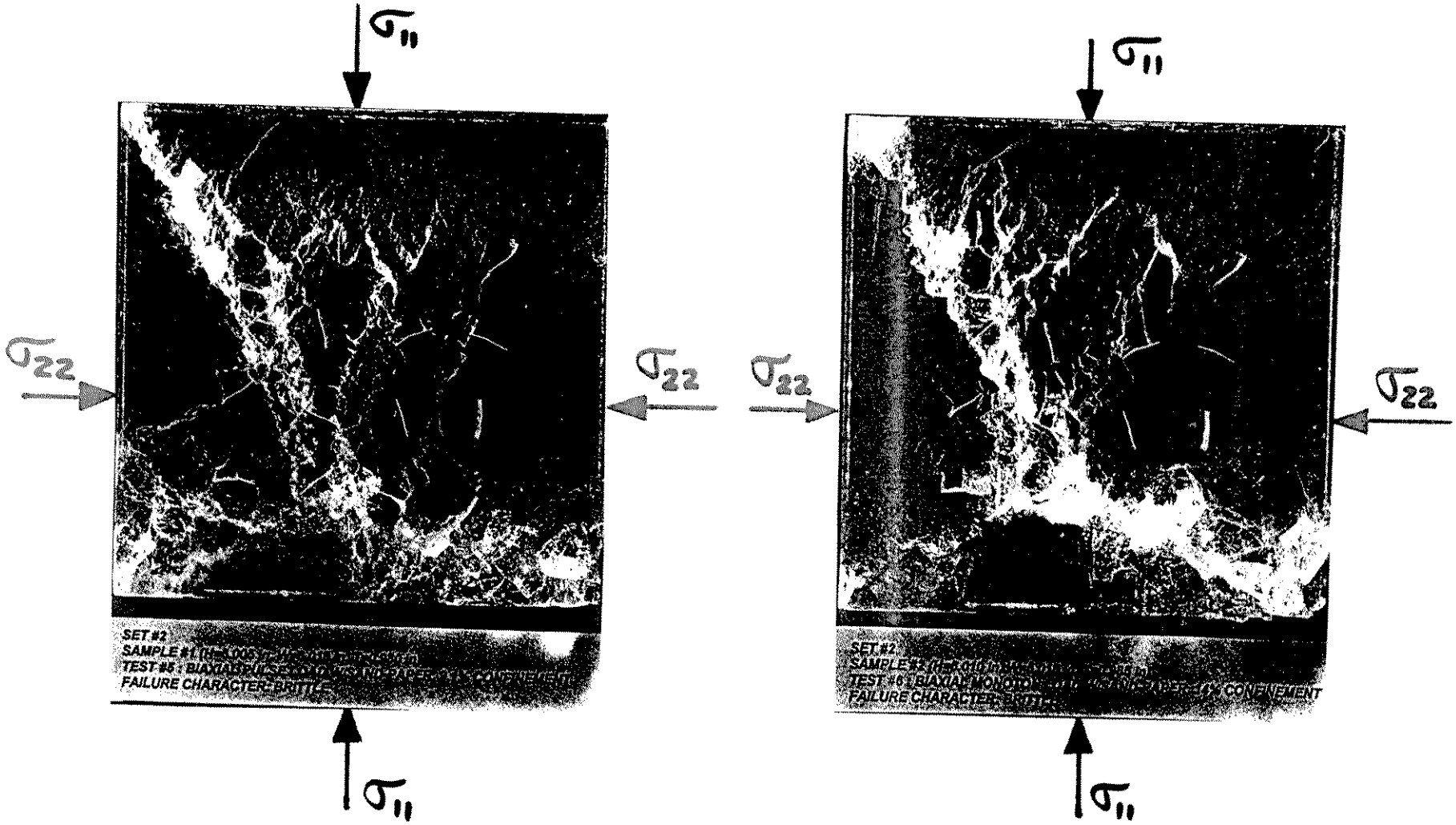

$\dot{\varepsilon} = 3.6 \cdot 10^{-2}$

$R = 9.1\,\%$

$\dot{\varepsilon} = 4.1 \cdot 10^{-2}$

$R = 14\,\%$

Fig. 11

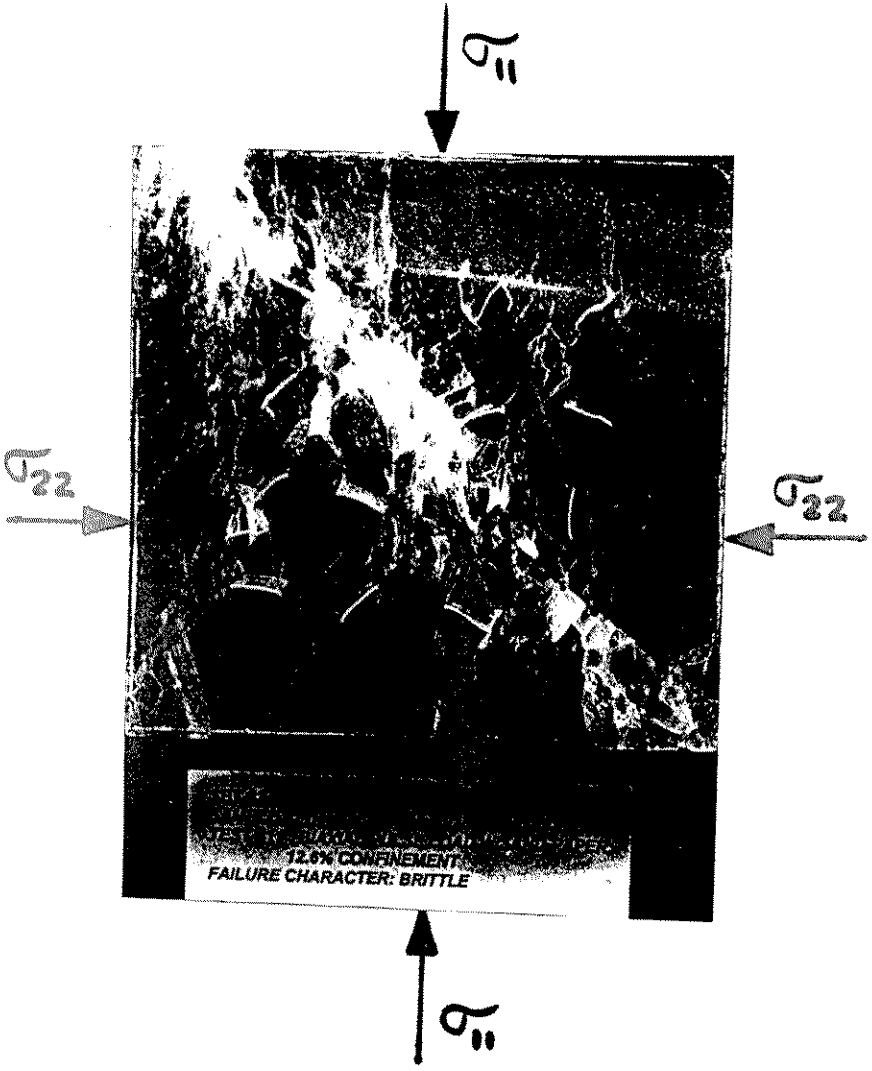
σ11
σ22
σ22
σ11
12.6% CONFINEMENT
FAILURE CHARACTER: BRITTLE
$\dot{\varepsilon} = 1.6 \cdot 10^{-2}$
R = 12.6 %

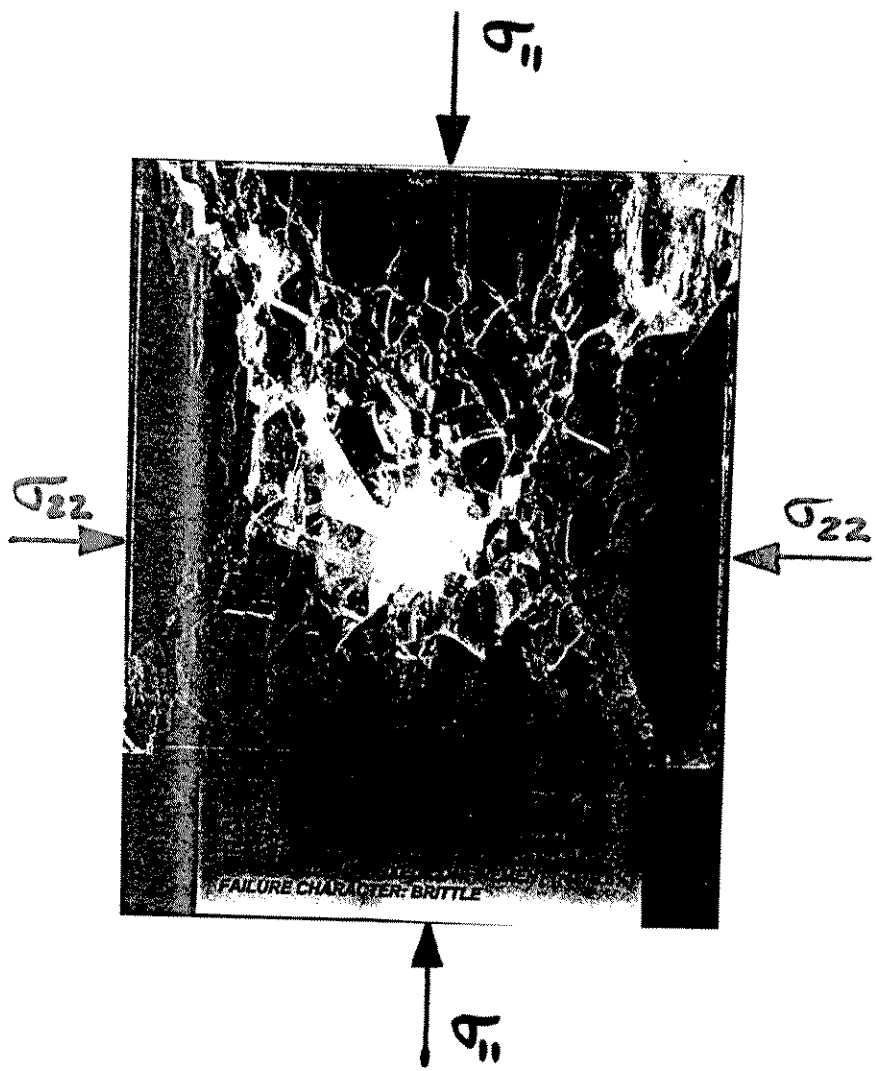
σ11
σ22
σ22
σ11
FAILURE CHARACTER: BRITTLE
$\dot{\varepsilon} = 1.6 \cdot 10^{-2}$
R = 9.6 %

Fig. 12

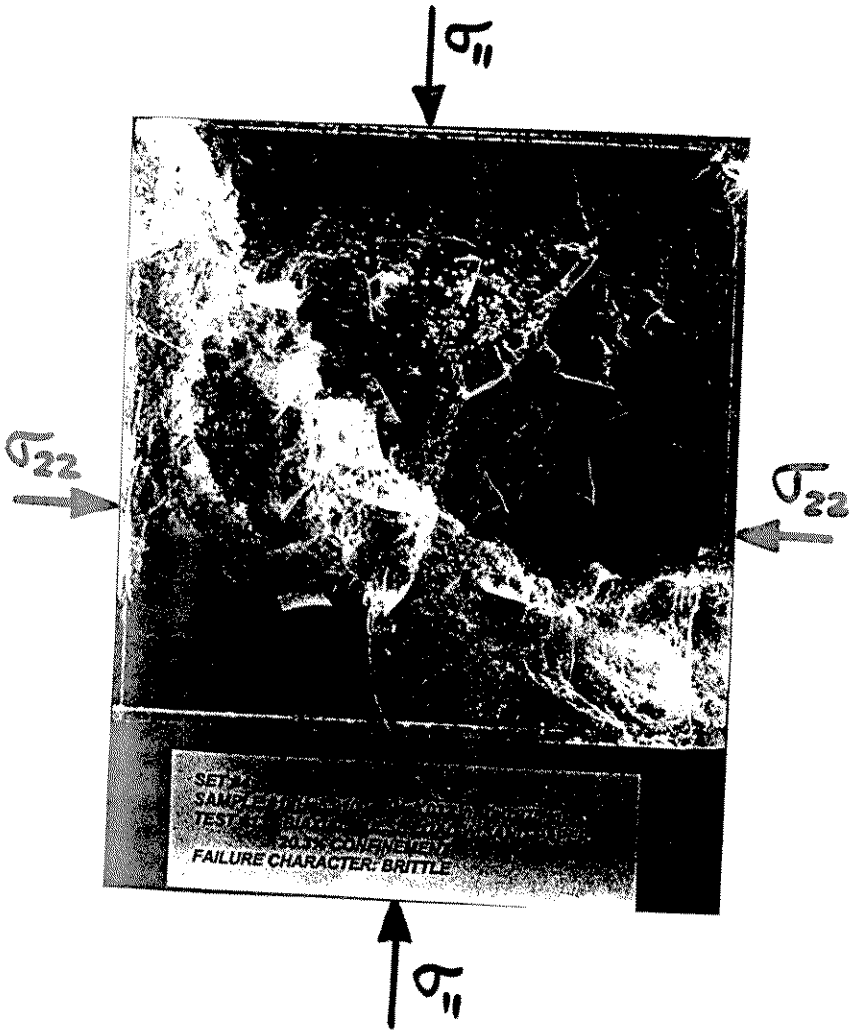

$\dot{\varepsilon} = 1.2 \cdot 10^{-2}$

$R = 20.3\%$

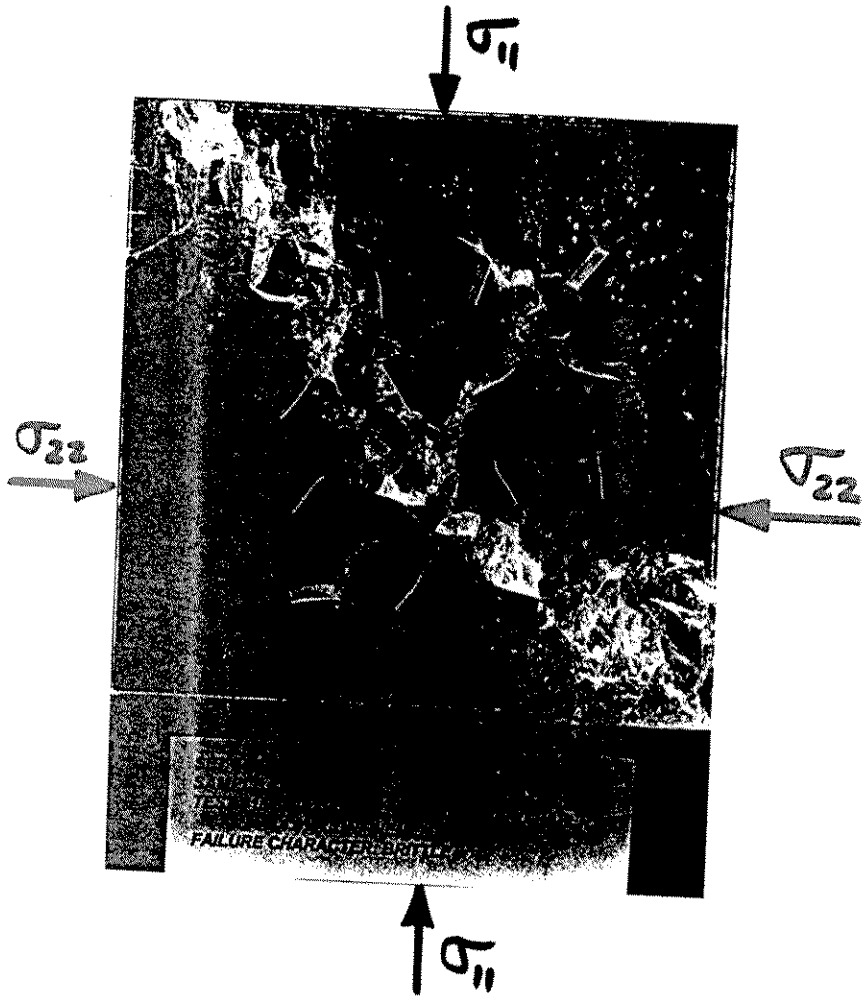

$\dot{\varepsilon} = 4 \cdot 10^{-3}$

$R = 4.8\%$

Fig. 13

ROTATED 90° CCW

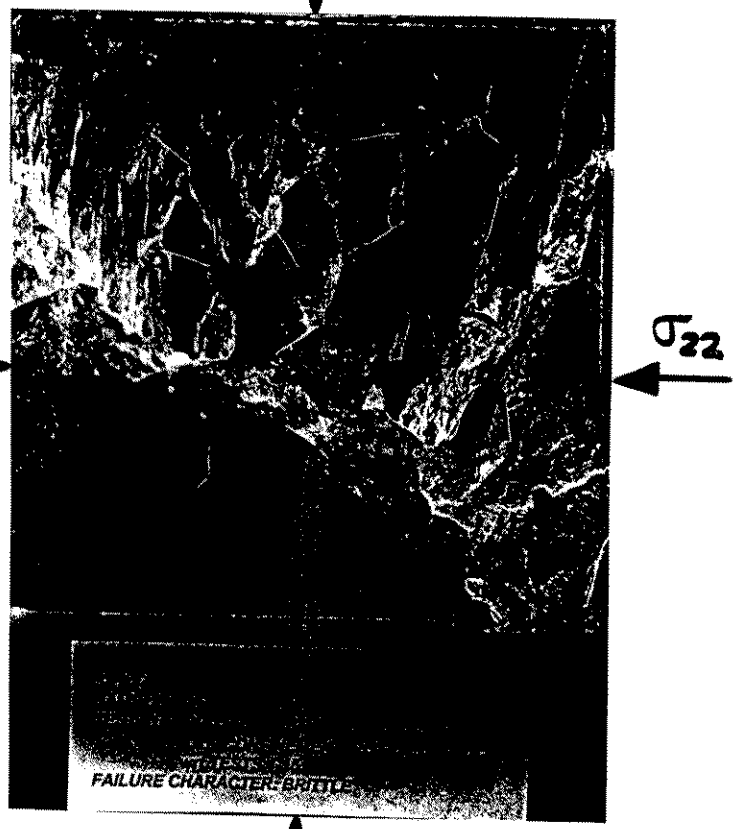

$\dot{\varepsilon} = 3.6 \cdot 10^{-3}$

R = 4.6 %

ROTATED 90° CCW

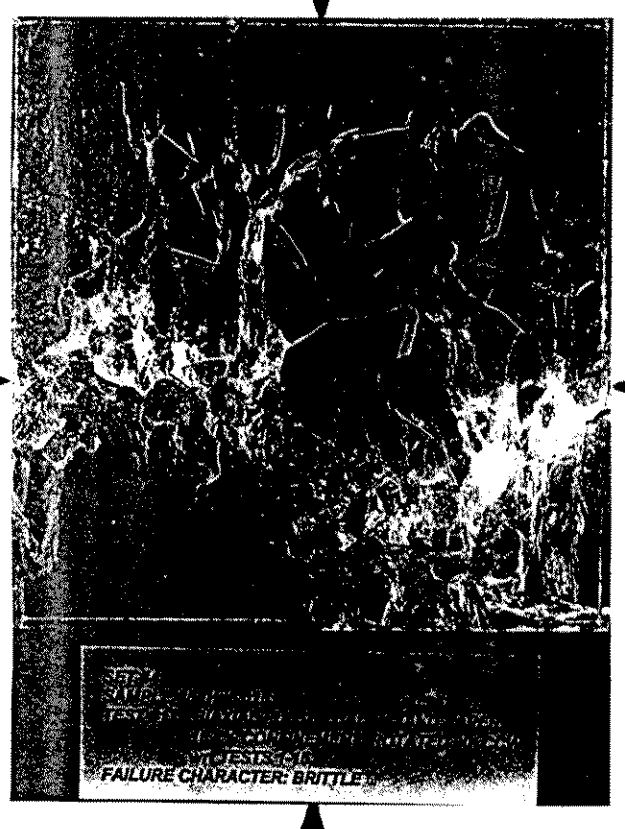

$\dot{\varepsilon} = 3.6 \cdot 10^{-3}$

R = 15.7 %

Fig. 14

The Brittle Compressive Failure of Columnar S2 Ice: A Comparison of Fresh-Water and Salt-Water Ice

by

E.T. Gratz and E.M. Schulson
Thayer School of Engineering
Dartmouth College
Hanover, N.H., 03755

The brittle compressive failure of salt-water columnar S2 ice has been described in Gratz and Schulson [1997]. Cubes of salt-water columnar ice were loaded using a true triaxial testing system where the stresses were applied perpendicular to the columnar-shaped grains (σ_{11} and σ_{22}) and parallel to the columnar-shaped grains (σ_{33}). Proportional loading was applied, i.e. the ratio of stresses σ_{11}:σ_{22}:σ_{33} was maintained during each test. The strain rate along the direction of the greatest compressive stress was 6×10^{-3} s^{-1} and the temperature was -10 °C for all tests. Three regimes (1, 2 and 3) of behavior were noted, each with a distinct dependence of strength on confinement and each with distinct failure modes. Regime 1 behavior is observed when loading is mainly across the columns and the across column confinement is low. Regime 2 behavior is observed when loading is mainly across the columns and the across-column confinement is moderate to high. Regime 3 behavior is observed for loading mainly along the columns. Similar tests have now been performed using fresh-water columnar S2 ice to allow comparison between the two ice types within each of the three regimes.

Regime 1: Within Regime 1, strength increases with confinement across the columns according to

$$\sigma_f = \sigma_o + k\,\sigma_c \qquad (1)$$

where $\sigma_f = \sigma_{11,f}$, σ_o is the uniaxial, across-column compressive strength $\sigma_{11,uf}$, $\sigma_c = \sigma_{22,f}$ and k is an experimental constant which we will denote k_1. Table 1 lists the values of $\sigma_{11,u}$ and k_1 reported by Smith and Schulson [1993 and 1994] for fresh-water columnar ice and salt-water columnar ice, respectively. In both cases, the constants were calculated based on data obtained for biaxial across-column loading at -10 °C and a strain rate near 6×10^{-3} s^{-1}. Within Regime 1, strength is insensitive to confinement along the columns [Gratz and Schulson, 1997] so Equation (1), originally used to describe the stresses at failure for biaxial loading, can also be used to describe the across-column stresses at failure for triaxial

loading, i.e. when confinement is applied along the columns as well as across the columns. Figure 1 shows the across-column stresses at failure $\sigma_{11,f}$ and $\sigma_{22,f}$ under triaxial loading for fresh-water columnar ice from Smith [1991] which overlap the results for salt-water columnar ice from Gratz and Schulson [1997]. Both sets of data fall near the dashed line which was drawn using equation (1) and the experimental values of $\sigma_{11,uf}$ and k_1 for fresh-water columnar ice.

Regime 2: Within Regime 2, strength increases with confinement along the columns. Figure 2 shows the results for tests conducted under balanced across-column loading, i.e. $\sigma_{11}=\sigma_{22}$. Both fresh-water and salt-water columnar ice show a large increase in strength for confining stresses up to about 2 MPa. At higher confining stresses, strength still increases with confinement but the sensitivity is much lower. The effect of the along-column confining stress on the strength is modeled as piece-wise linear using two expressions based on equation (1) where, in this case, $\sigma_f = \sigma_{11,f}$, σ_o is a constant which depends on the across-column confinement ratio $R_{21}=\sigma_{22}/\sigma_{11}$, k is another experimental constant, and $\sigma_c = \sigma_{33,f}$. Over low confining stresses, which we will denoted as Regime 2a, $\sigma_o = \sigma_{11,o}/(1+R_{21})$ [Smith and Schulson, 1993 and 1994] and $k = k_{2a}$. At moderate confining stresses, which we will denote as Regime 2b, $\sigma_o = \sigma_{11,2b}$ and $k = k_{2b}$. Table 1 lists values for $\sigma_{11,o}$ from Smith and Schulson [1993, 1994] and values for k_{2a}, $\sigma_{11,2b}$ and k_{2b} derived from linear regression analysis of the data plotted in Figure 2.

Regime 3: Within Regime 3, strength increases with the smaller across-column confining stress according to equation (1) where $\sigma_f = \sigma_{33,f}$, σ_o equals the uniaxial compressive strength along the columns $\sigma_{33,uf}$, k is another experimental constant, and $\sigma_c = \sigma_{22,f}$. Figure 3 shows the results for tests conducted under balanced across-column confinement, i.e. $\sigma_{11}=\sigma_{22}$. Fresh-water columnar ice is stronger that salt-water columnar ice under uniaxial compression along the columns, however they share similar strengths when

across-column confinement is applied. Table 1 lists values of $\sigma_{33,uf}$ and $k=k_3$ for fresh-water and salt-water columnar ice.

The results shown in Figures 1-3 indicate that fresh-water columnar ice and salt-water columnar ice have similar brittle failure strengths when loaded under triaxial compression. These results and additional data were used to establish the brittle compressive failure surfaces for fresh-water and salt-water columnar ice. Figure 4a shows the surface for fresh-water columnar ice, and Figure 4b shows the surface for salt-water columnar ice. For both materials, the surfaces expand as the hydrostatic component of the stress tensor increases, in accord with Mohr-Coulomb behavior and with the frictional crack sliding mechanism of brittle failure. Both materials fail through macroscopic faulting which results from the linking up of cracks nucleated during the deformation. The principal difference is that the deformation damage to the salt-water ice is restricted more to the vicinity of the faults, owing to the crack-stopping influence of the brine pockets. Otherwise, the brittle compressive strength and the failure modes of the two materials are essentially the same.

	Fresh-Water S2 Ice	Salt-Water S2 Ice
$\sigma_{11,uf}$	3.8 MPa	3.5 MPa
k_1	3.1	3.1
$\sigma_{11,o}$	15 MPa	16 MPa
k_{2a}	10	4.5
$\sigma_{11,2b}$	17 MPa	insufficient data
k_{2b}	1.6	insufficient data
$\sigma_{33,uf}$	8.2 MPa	5.6 MPa
k_3	4.4	7.2

Table 1: Experimental parameters describing the strength of fresh-water columnar ice and salt-water columnar ice.

References

Gratz, E.T. and Schulson, E.M. (1997). Brittle failure of columnar saline ice under triaxial compression. Journal of Geophysical Research, 102(B3), 5091-5107.

Smith, T.R. and Schulson, E.M. (1993). The brittle compressive failure of fresh-water columnar ice under biaxial loading. Acta metall. mater., 41(1), 153-163.

Smith, T.R. and Schulson, E.M. (1994). Brittle compressive failure of salt-water ice under biaxial loading, Journal of Glaciology, 40(135), 265-276.

Smith, T.R. (1991). The effect of stress state on the brittle compressive failure of columnar ice. Ph.D. Thesis, Thayer School of Engineering, Dartmouth College.

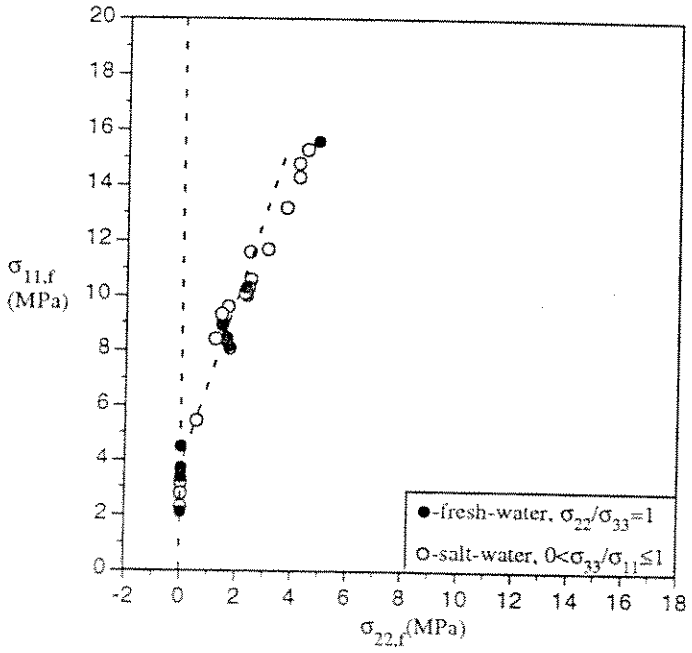

Figure 1: Across-column stresses at failure within Regime 1 for fresh-water and salt-water columnar ice loaded under triaxial compression.

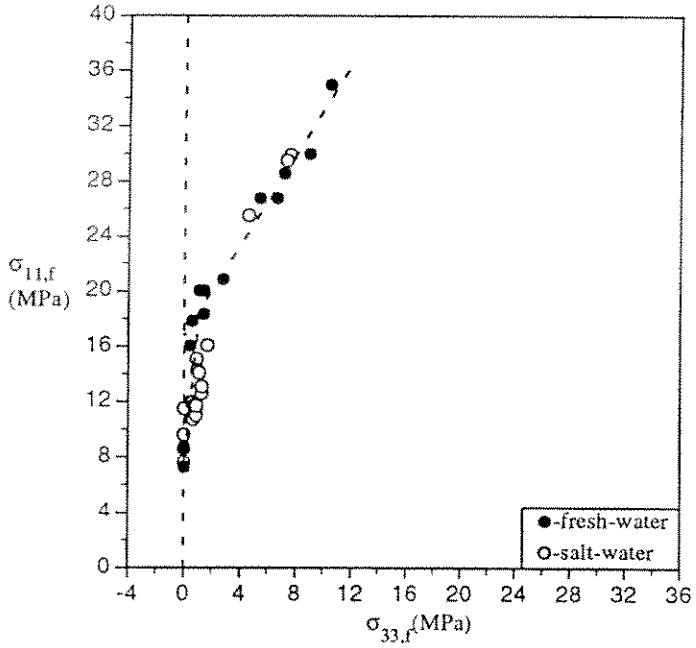

Figure 2: Strength versus along-column confining stress within Regime 2 for fresh-water and salt-water columnar ice loaded under balanced across-column confinement.

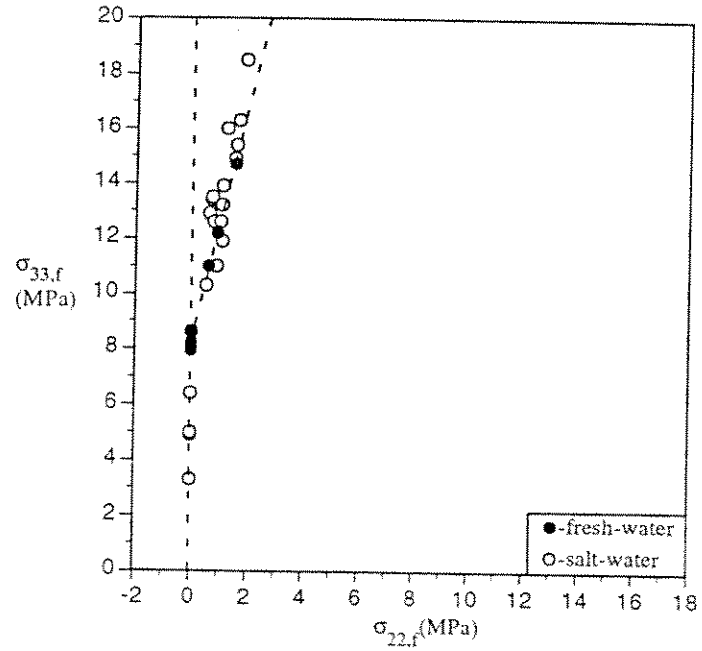

Figure 3: Along-column stress at failure versus across-column confining stress within Regime 3 for fresh-water and salt-water columnar ice loaded under balanced across-column confinement.

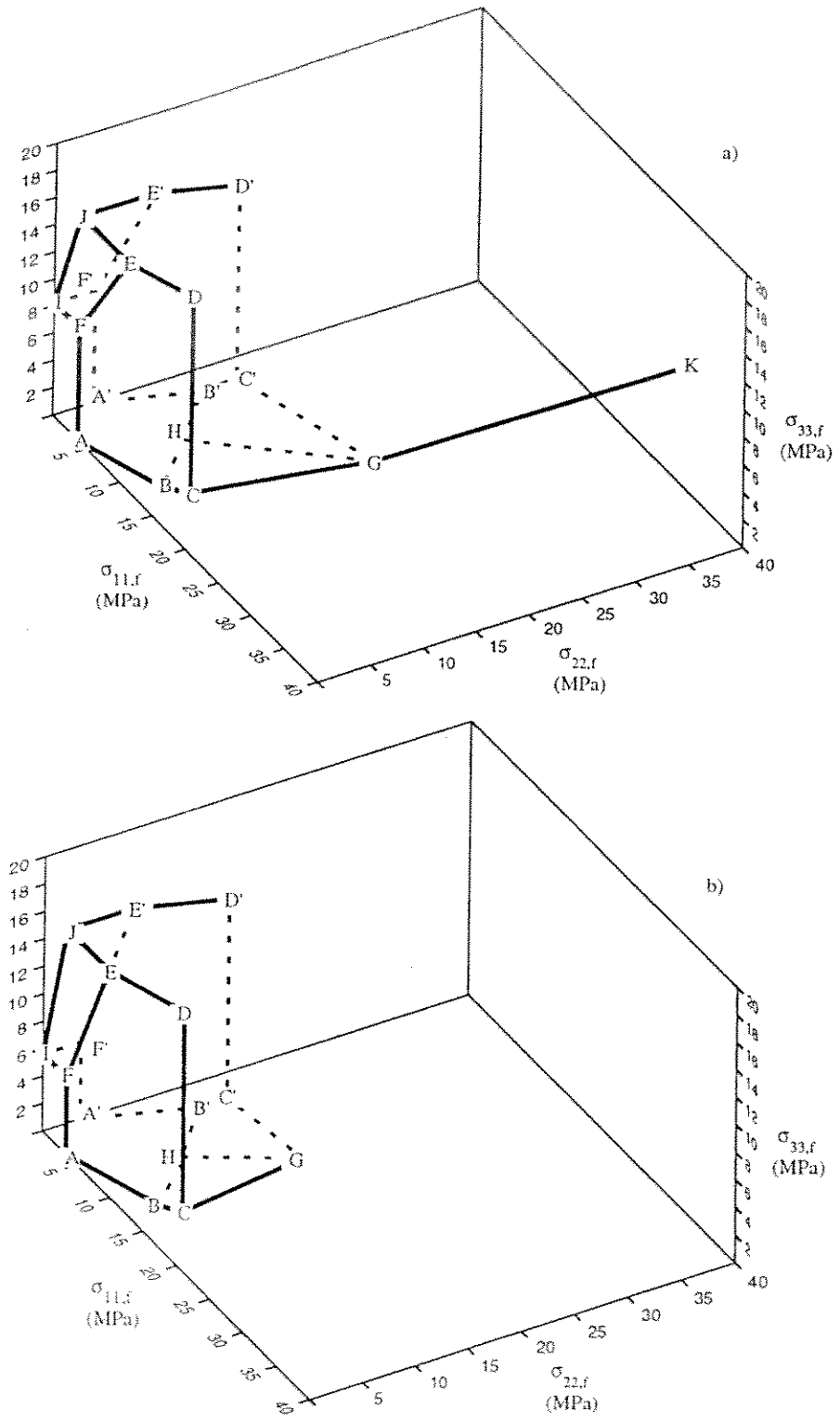

Figure 4: Brittle compressive failure surface for a) fresh-water columnar ice and b) salt-water columnar ice loaded under triaxial compression at -10 °C and a strain rate of 6×10^{-3} s^{-1}.

The Ductile Compressive Strength of Columnar S2 Ice: A Comparison of Behavior Under Proportional and Conventional Triaxial Loading

by
Jeffrey S. Melton and Erland M. Schulson
Ice Research Laboratory
Thayer School of Engineering
Dartmouth College, Hanover, NH, 03755

The deformation of laboratory-grown S2 columnar saline ice (LGSI) under triaxial compressive loading was investigated at a temperature of -10°C with a constant strain rate of 3.9×10^{-5} s^{-1}, using an MTS multiaxial servo-hydraulic testing system. All of the tests were carried out on 160mm cubic samples prepared from ice grown in this laboratory. In one set of tests the samples were proportionally loaded with confinement ratios of $R_{21}=\sigma_{22}/\sigma_{11}=0.25$, 0.5, and $R_{31}=\sigma_{33}/\sigma_{11}$ variable; σ_{11} and σ_{22} are normal stresses applied in two orthogonal directions across the columns and σ_{33} is applied along the columns. A second set of tests was performed to simulate conventional triaxial loading. In this case the samples were loaded hydrostatically ($\sigma_{11}=\sigma_{22}=\sigma_{33}$) to an initial pressure and then loaded along x_1 at a constant strain rate of 3.9×10^{-5} s^{-1} while σ_{22} and σ_{33} were held constant. In this scheme x_1 and x_2 are perpendicular to the long axis of the columns; x_3 is parallel to the column axis.

At $R_{21}=0.25$ and 0.5 the behavior of the ice was macroscopically ductile, with the yield stress $\sigma_{11,y}$ independent of R_{31} as shown in Figure 1. The results suggest that $\sigma_{11,y}$ can be predicted by Hill's (1950) criterion for the yielding of plastically orthotropic materials. The upper and lower limits of Hill's (1950) criterion are plotted as solid lines in Figure 2. Additional analysis suggests that the flow stress for up to 2% inelastic deformation is also reasonably predicted by Hill's criterion (1950), using appropriate coefficients.

The results also suggest that the flow behavior of the ice is a function of both R_{21} and R_{31}. At $R_{21}=0.25$ the stress-strain curve (σ_{11} vs. ε_{11}) generally exhibits a well defined peak that gradually tapers off with increasing strain, as seen in

Figure 3a. The shape of the curve did not change with increasing along-column confinement. For R_{21}=0.5 the shape of the curve depended on the along-column confinement. For R_{31}<0.5 the stress-strain curve shows a broad peak and then remains fairly flat with increasing strain, Figure 3b. Figure 3c shows that at higher values of R_{31} the post-yield behavior is characterized by a flow stress that slowly increases with increasing strain, without a peak. Attempts are being made to characterize the stress-strain curve and determine which deformation mechanisms contribute to the shape of the curve.

All tests were terminated after testing to ε_{11}=0.03. Thin sections (≈1.5 mm thick) were made within minutes of unloading to ensure that the observed microstructure was free from post-test features. Across-column cracks were found in all post-test examinations of the microstructure. The crack density was on the order of 400 cracks/m^2, and the distribution of cracks appeared to be independent of across-column and along-column confinement. The crack lengths were typically 5 mm, usually with one tip originating at the grain boundary and the other tip terminating in the grain interior. The crack widths were generally less than 1 mm, and many cracks did not appear to have opened. Additionally, there did not appear to be any dynamic recrystallization, which was observed in tests performed at R_{21}=1.0 (Melton and Schulson, 1995)

In the "conventional" triaxial tests the yield stress $\sigma_{11,y}$ increases as the initial confining pressure increases, Figure 4. This behavior makes sense since the increasing confining pressure inhibits basal slip, raising the stress needed to initiate yielding. In all tests the stress-strain curve (σ_{11} vs. ε_{11}) had a well defined peak

followed by strain-softening.

Comparison of the yield stresses from the proportional loading tests and "conventional" loading tests are shown in Figure 5. There does not appear to be any significant difference in the yield strengths from the two loading paths, within experimental scatter. Further analysis has shown that there is no difference in the flow stresses taken at other points on the stress-strain curve (σ_{11} vs. ε_{11}), up to 2% inelastic deformation.

References

Hill, R (1950). "The Mathematical Theory of Plasticity," Oxford University Press, New York, pp 317-323.

Melton, JS and Schulson, EM (1995). "Preliminary Results on the Ductile Deformation of Columnar Saline Ice Under Triaxial Compressive Loading," *Proc OMAE 95*, Vol 4, pp 139-143.

Figure 1. The yield strength $\sigma_{11,y}$ is given for across-column confinement of R_{21}=0.25 and R_{21}=0.5 as a function of the along-column confinement R_{31}. Statistical analysis shows that the yield strength does not significantly depend on R_{31}.

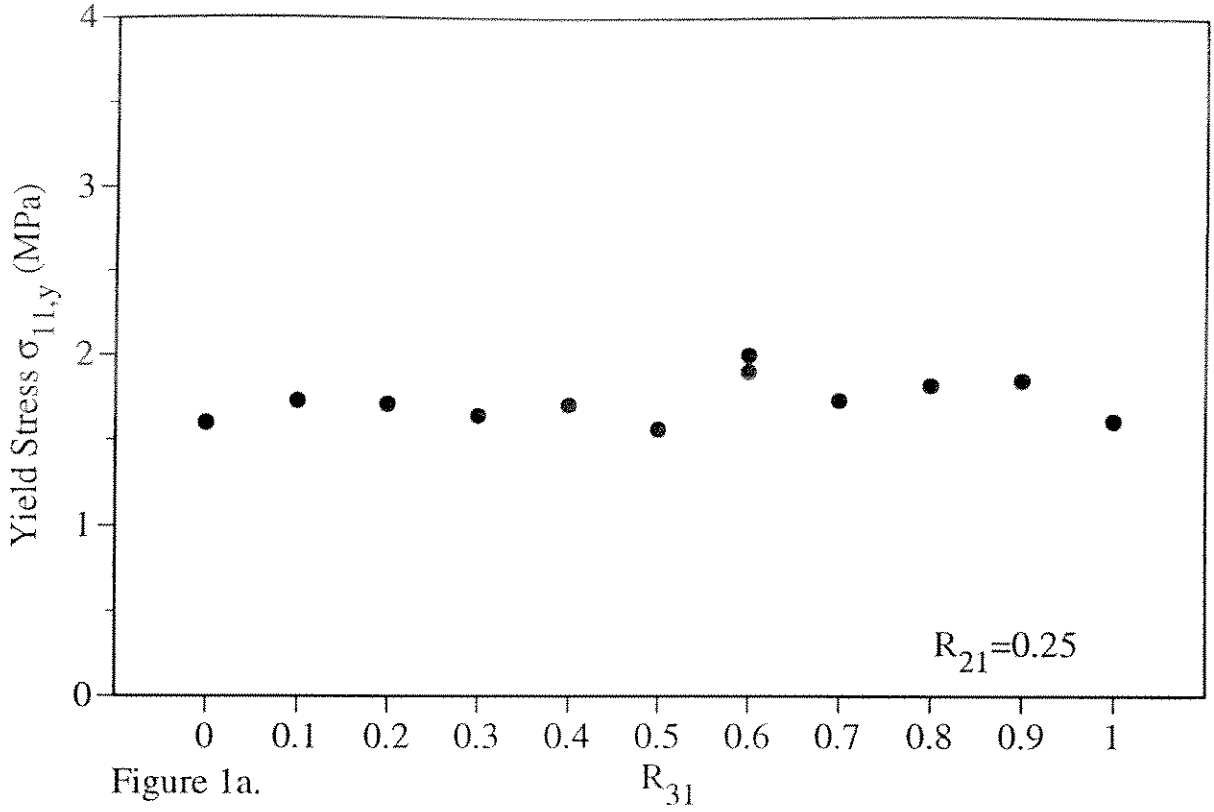

Figure 1a.

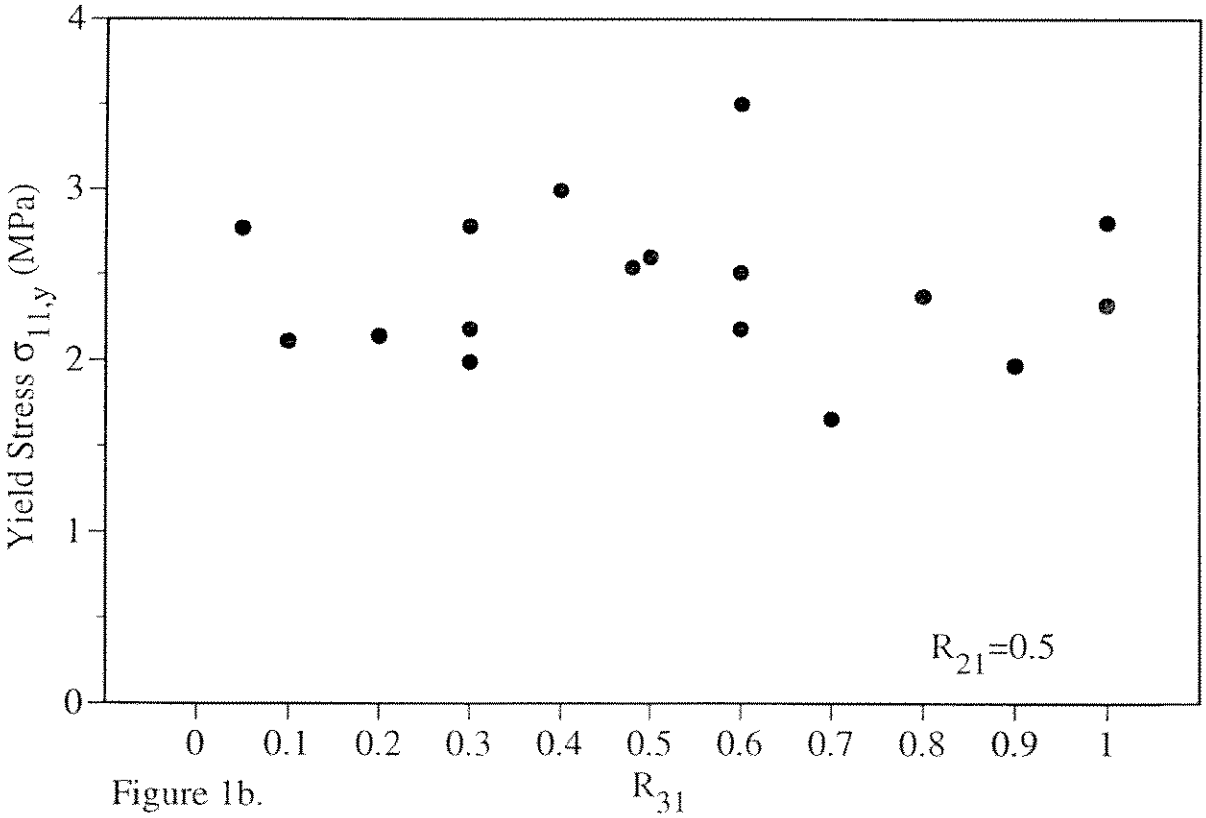

Figure 1b.

Figure 2. The yield strength data given in Figure 1 is shown with the upper and lower bounds of Hill's (1950) criterion. The bounds were calculated using uniaxial yield strength values of 1.4 MPa across the columns and 7.4 MPa in the along-column direction.

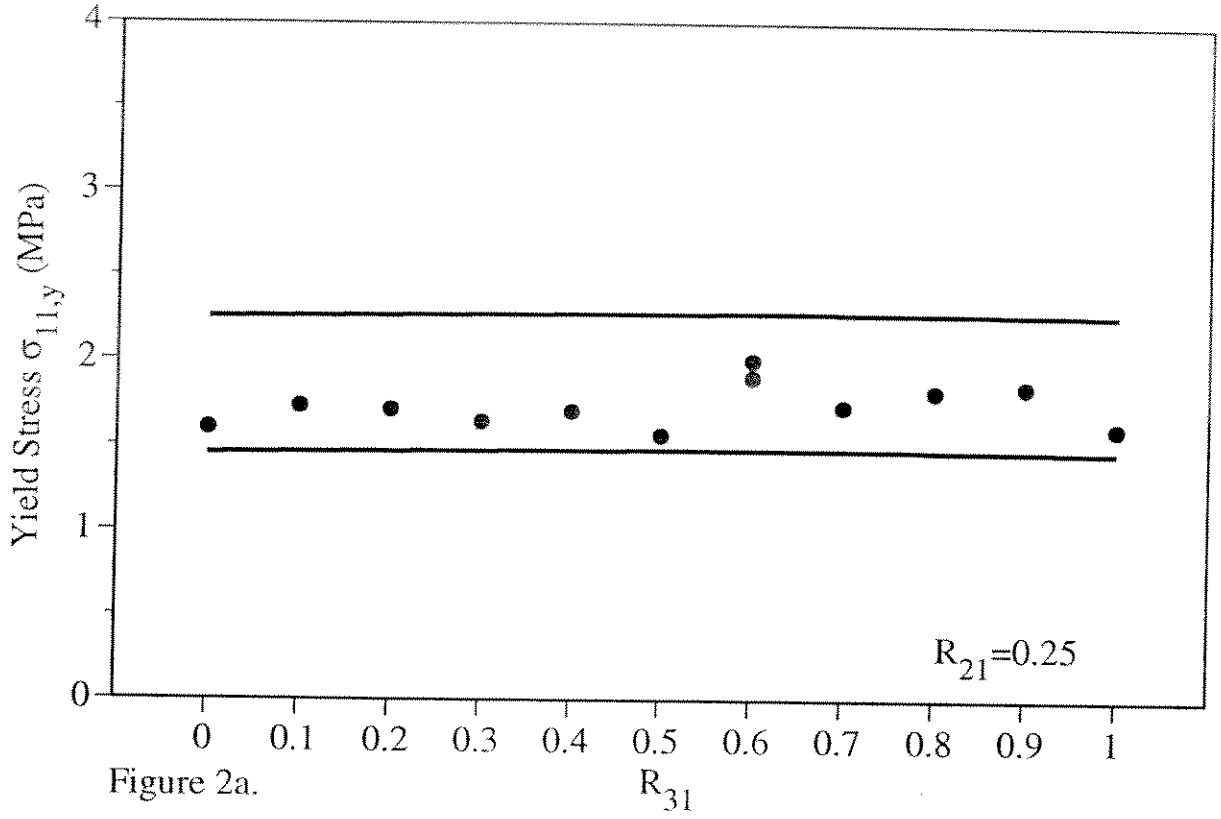

Figure 2a.

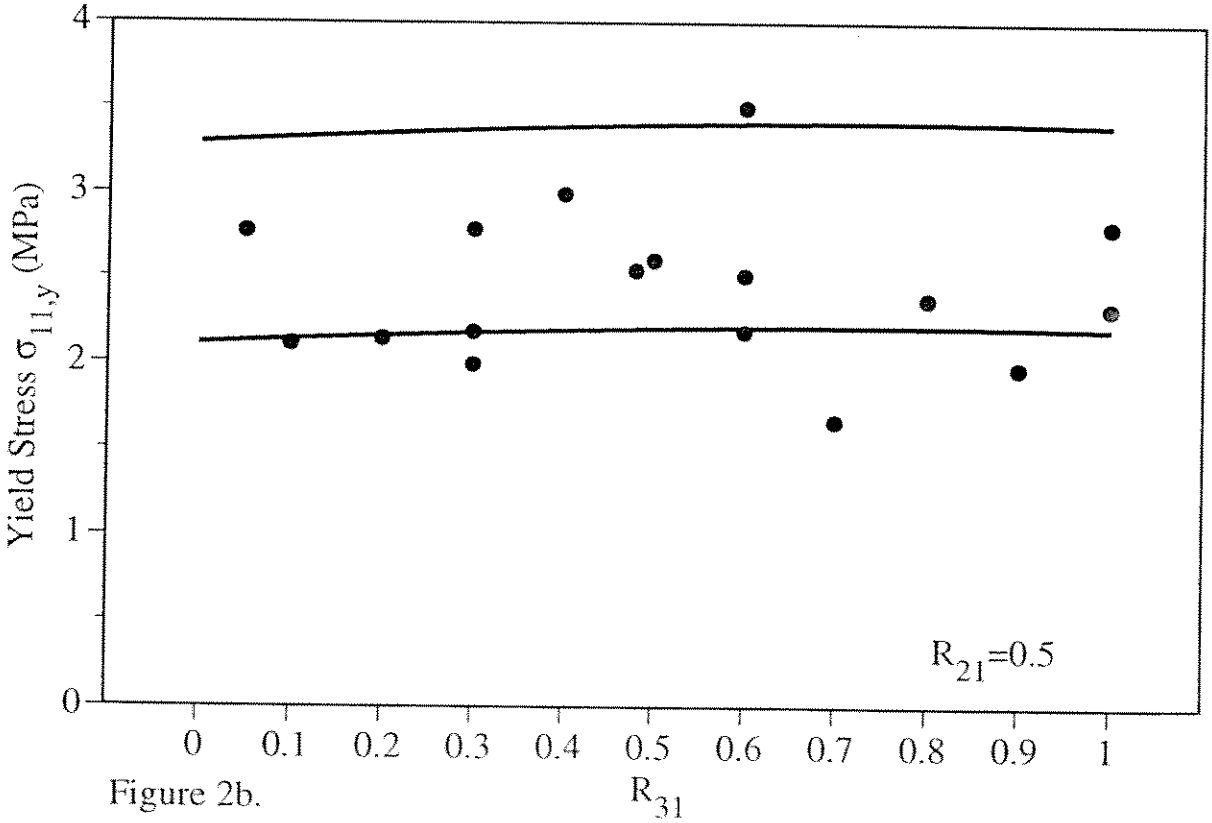

Figure 2b.

Figure 3. The flow curve (σ_{11} vs. ε_{11}) changes shape with increasing confinement. Figure 3a shows a flow curve for low confinement (R_{21}=0.25, R_{31}=0.1) which generally has a distinct peak followed by strain softening. At higher confinement (R_{21}=0.5, R_{31}=0.1) the strain softening is suppressed, so that the post-yield branch of the flow curve is flat as seen in Figure 3b. As R_{31} increases the post-yield branch of the flow curve develops pronounced strain hardening (Figure 3c, R_{21}=0.5, R_{31}=0.8).

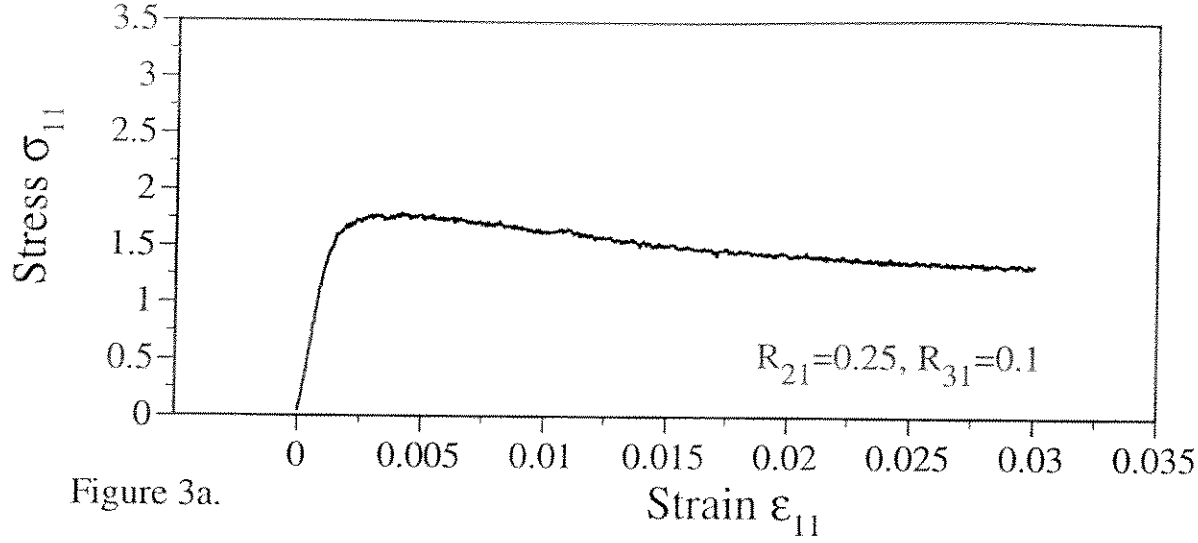

Figure 3a.

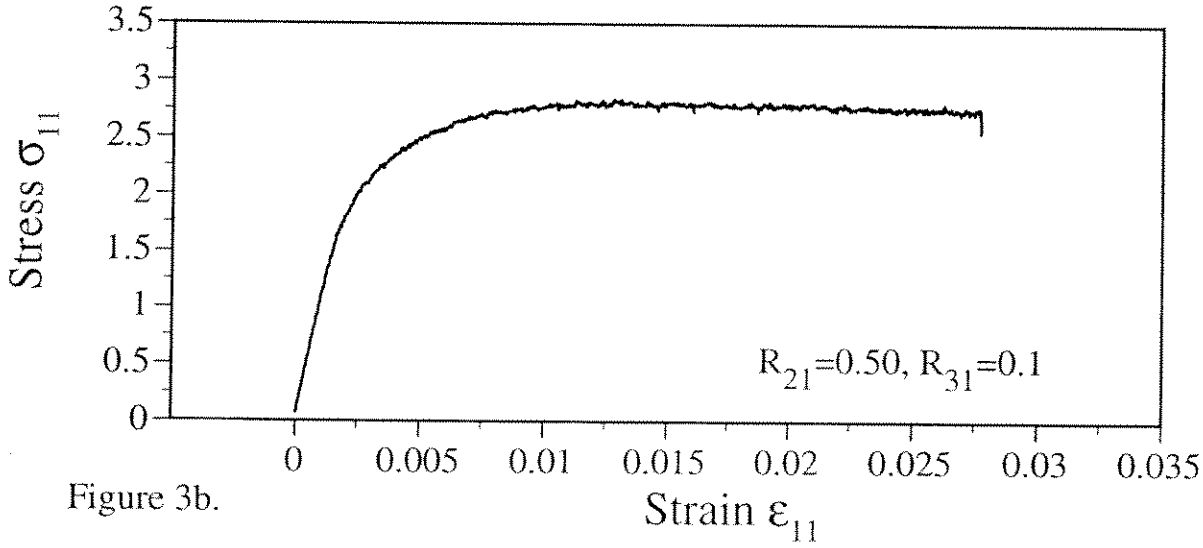

Figure 3b.

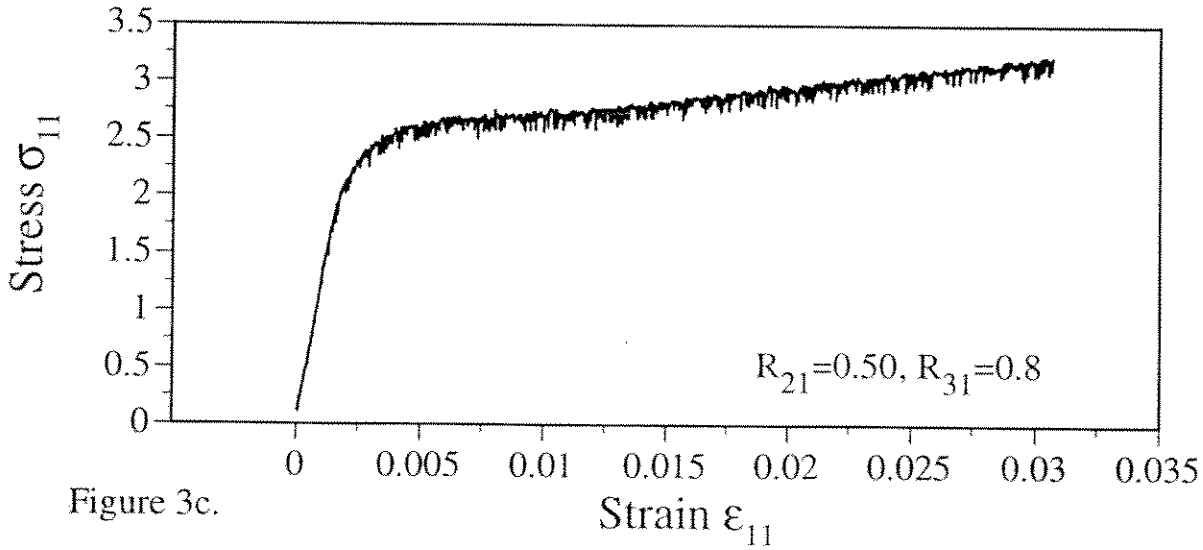

Figure 3c.

Figure 4. The yield strength $\sigma_{11,y}$ for the "conventional" triaxial tests are plotted as a function of the initial confining pressure. Notice that the yield strength increases with increasing confinement, which is consistent with deformation due to basal slip.

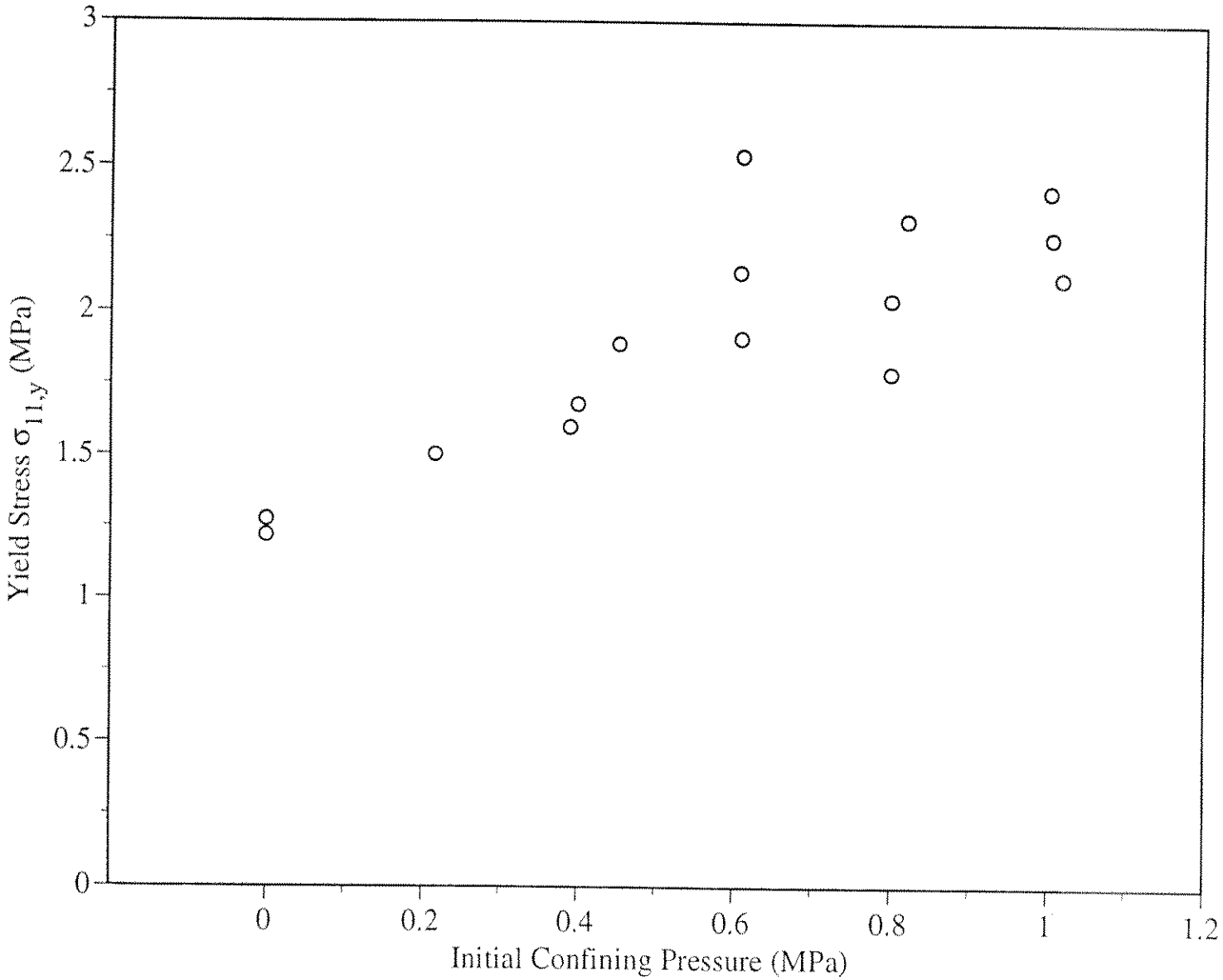
Yield Stress $\sigma_{11,y}$ (MPa)
3
2.5
2
1.5
1
0.5
0
0
0.2
0.4
0.6
0.8
1
1.2
Initial Confining Pressure (MPa)

Figure 4.

Figure 5. The yield strength $\sigma_{11,y}$ is re-plotted as a function of the along-column confinement ratio R_{31}, measured at the yield stress. The two solid lines are expected values for R_{21}=0.25 and R_{21}=0.5, respectively. Other expected yield strengths for different values of R_{21} were found by interpolation and are shown as dashed lines. For "conventional" tests R_{21}=R_{31}, so the R_{21} value of a test point can be found from the R_{31} value and compared to the expected yield strength for a proportional loading test of the same R_{21} value.

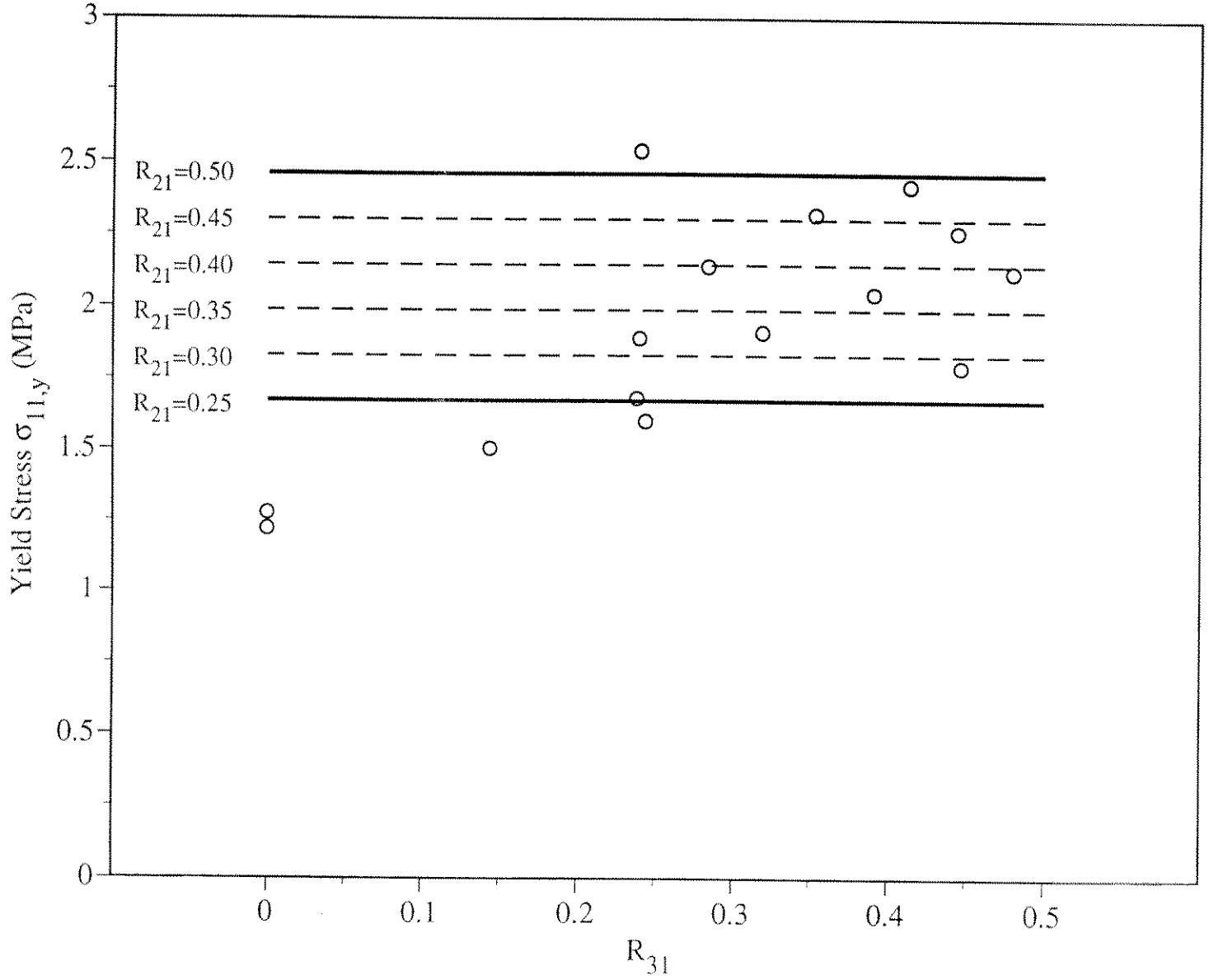
3
2.5
2
1.5
1
0.5
0
0
0.1
0.2
0.3
0.4
0.5
R31
Yield Stress σ11,y (MPa)
R21=0.50
R21=0.45
R21=0.40
R21=0.35
R21=0.30
R21=0.25

Figure 5.

The Ductile-to-Brittle Transition in Ice Unde Compression: The Effect of Temperature

by Suogen Qi and E. M. Schulson

Thayer School of Engineering
Dartmouth College
Hanover, NH 03755

Ductile-to-Brittle Transition in Ice Under Compression: Temperature Effect

Under compressive loading, ice exhibits ductile behavior at lower strain rates and brittle behavior at higher strain rates. The ductile-to-brittle transition is of interest for two reasons. First, it marks the highest strength of ice and thus the highest load during ice structure interaction. Second, it implies different deformation mechanisms on both sides of the transition.

Schulson [1, 2] has modelled the ductile-to-brittle transition. His first transition model is mainly phenomenological one.In recent works, the second model, termed physical transition model, is presented. It can be expressed as :

$$\dot{\varepsilon}_{11} = \frac{1.2B'K_{IC}^3}{f d^{1.5}\left\{\left(1+\mu^2\right)^{0.5} - \mu - R_{21}\left[\mu + \left(1+\mu^2\right)^{0.5}\right]\right\}}$$

where K_{IC} is the fracture toughness, d is the crack size which is set by the grain size, μ is the kinetic friction coefficient of ice on ice, f denotes the ratio of the crack tip zone size to the size of the parent, sliding crack, R is the confining stress ratio, and B' is the creep constant in the power law creep equation $\dot{\varepsilon}_c = B'\sigma^n$ (where B'=Bexp(-Q/RT) and B is experiment constant and Q is the Activation energy). This model successfully accounts for the dependence of transition rate on grain size d[3]. It also implies that the transition strain rate will be a function of temperature through K_{IC} μ , and B. The purpose of this work is to investigate the effect of temperature on the transition strain rate.

Both the fresh water and salt water columnar ice used in this study were grown in the IRL following standard procedures by Kuehn and Schulson [4]. The plate samples were machined so

that the columns of ice were perpedicular to the largest face of the samples. The tests were performed using a MTS uniaxial testing system at -3, -20,-30,and -40 °C ±0.2 °C. The long dimention of the specimens were strained at rates between 10^{-6} to $10^{-1}\,s^{-1}$.

The results indicate that both fresh water and salt water columnar ice exhibit ductile behavior at lower stran rates and brittle behavior at higher strain rates. The peak stress and failure stress for both fresh water and salt water ice increased with decreasing temperatures. The strength of fresh water ice is higher than that of salt water ice.The ductile-to-brittle transition strain rate decreased with decreasing temperature for both types of ice. The transition rate of salt water ice is one order of magnititude higher than that of fresh water ice at the same temperature. At lower strain rates, cracks formed along grain (column) boundaries, increasing in number with increasing load. In this case , the new crack formation dominated over the crack propagation.This leads to macroscopic ductile behavior. At higher strain rates , cracks still formed along boundaries, but with increasing load, the cracks propagated and split the samples. This resulted in macroscopic brittle behavior.

In Schulson's model, the transition was explained in terms of the competition between the buildup and the relaxation of tensile stresses around the tips of the inclined cracks. The transition strain rate was modelled in terms of frictional crack sliding, wing cracking and creep. The observaions of crack nucleation and propagation confirmed this point in the model. At lower strain rates, the stress relaxation dominates and the samples showed ductile behavior, while at higher strain rates, the stress buildup dorminates and the samples exhibited brittle behavior. Calculating the activation energy Q in Schulson's model gives out interesting results. It is found that Q values increased with increasing temperature from 73.5 kJ /mol for fresh water ice and 60.97 kJ /mol for salt water ice at -40 °C to 78.5 kJ /mol for fresh water ice and 63.36 kJ / mol for salt water ice at - 3 °C. Although not sufficent activation energy data are available, this result is approximately in agreement with what is found in the literatures[5,6].

References:

1.E.M.Schulson, Acta metall.mater.38,1963,1990

2.E.M.Schulson and S.E. Buck, Acta metall.mater. 43, 3661, 1995

3.R.A.Batto and E.M.Schulson, Acta metall.mater.41,2219,1993

4.Kuehn, G. A., and E.M.Schulson,Ann.Glaciol.,39,1994

5.Weertman Johannes, Ann.Res.Earth planet Sci.,11,215,1983

6.P.Barnes,Proc.R.Soc.London A,324,127,1971

7.W.A.Nixon and E.M. Schulson, Journal de physi. 48,313,1987

8.D.E.Jones, Annals of Glaciology,15,242,1991

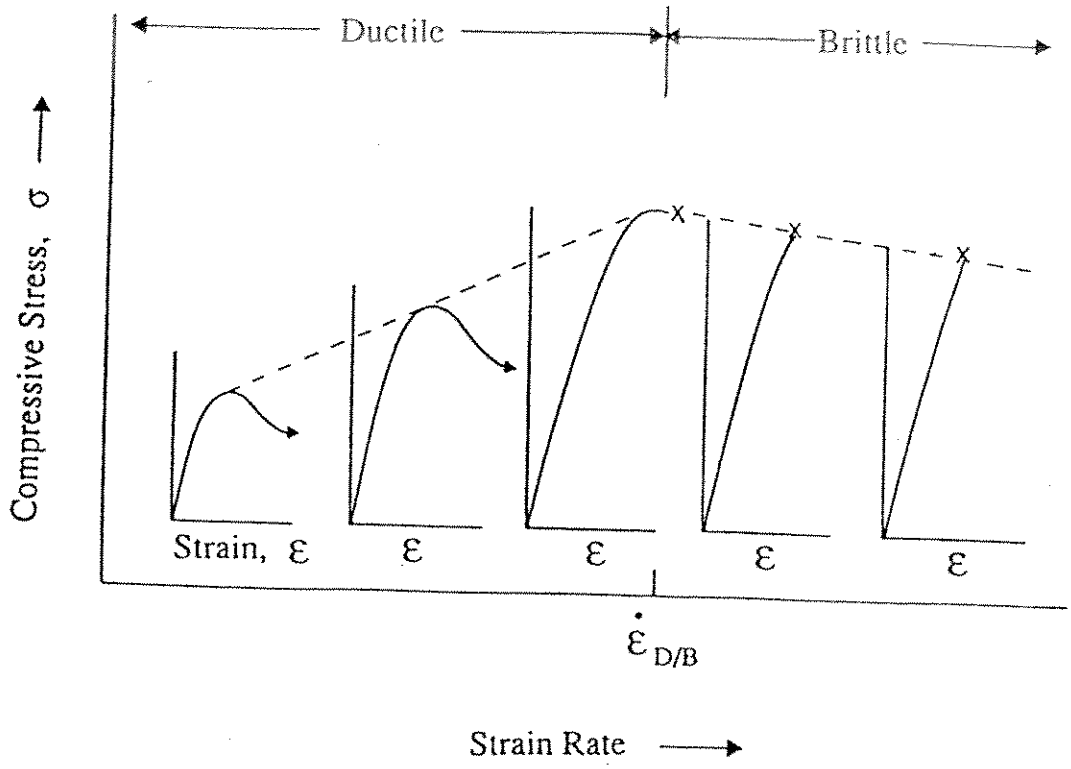

Schematic stress–strain curves for polycrystalline ice compressed under uniaxial loading. The arrow denotes deformation without collapse to higher strains; the x, macroscopic failure. A transition occurs from ductile to brittle behavior upon raising the strain rate above $\dot{\epsilon}_{D/B}$. The compressive strength as indicated by the envelope, responds differently to strain rate within the two regimes, indicating different deformation mechanisms.

Schulson's Transition Model

$$\dot{\varepsilon}_{11} = \frac{1.2B'K_{IC}^3}{f d^{1.5}\left\{\left(1+\mu^2\right)^{0.5} - \mu - R_{21}\left[\mu + \left(1+\mu^2\right)^{0.5}\right]\right\}}$$

where K_{IC} is the fracture toughness, B' is the creep constant in the power law creep equation $\dot{\varepsilon}_c = B'\sigma^n$ (where $B' = Be^{-Q/RT}$ and B is experiment constant and Q is the Activation energy), μ is the kinetic coefficient of friction of ice on ice; f denotes the ratio of the crack tip creep zone size to the size of the parent, sliding crack . R_{21} is confining stress ratio.

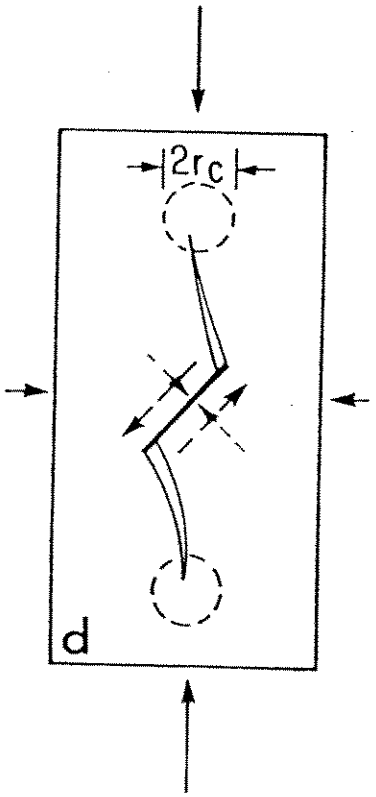

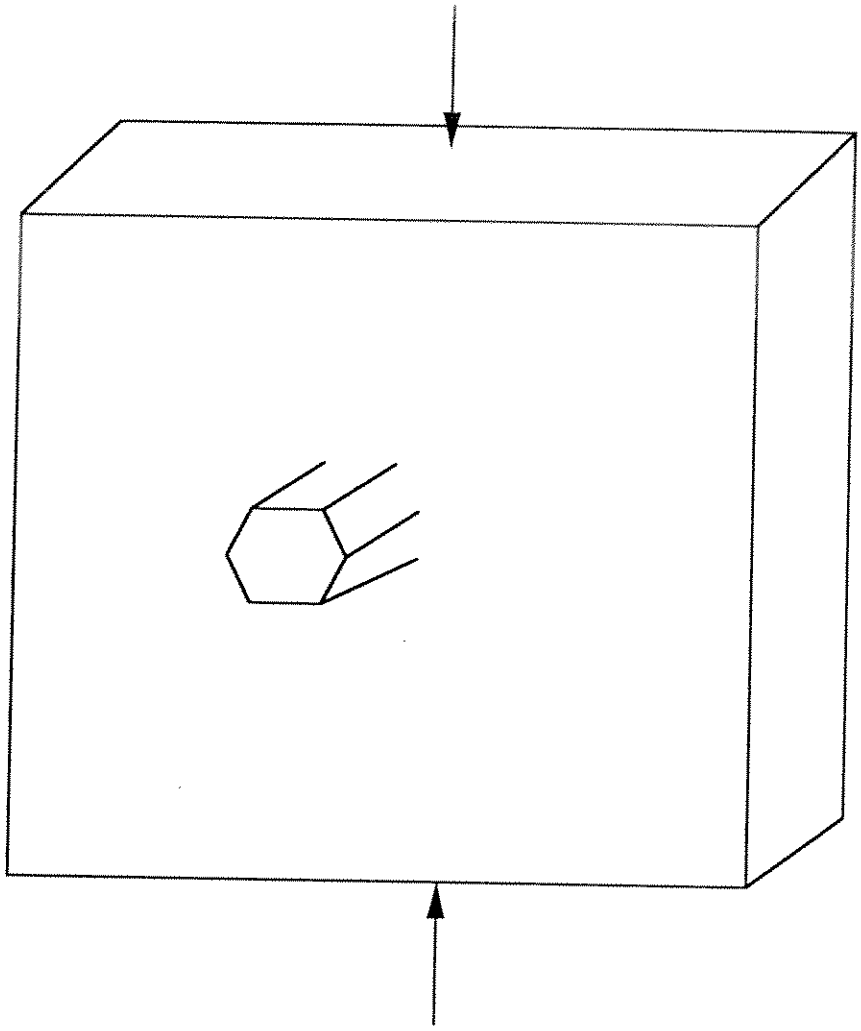

Materials: Fresh Water Ice and Salt Water Ice
Sample Size: 6x6x1" and 6x4x1"
Temperature: -40 to -3 $^{\circ}C$
Strain Rate: $10^{-6}s^{-1} to 10^{-1}s^{-1}$

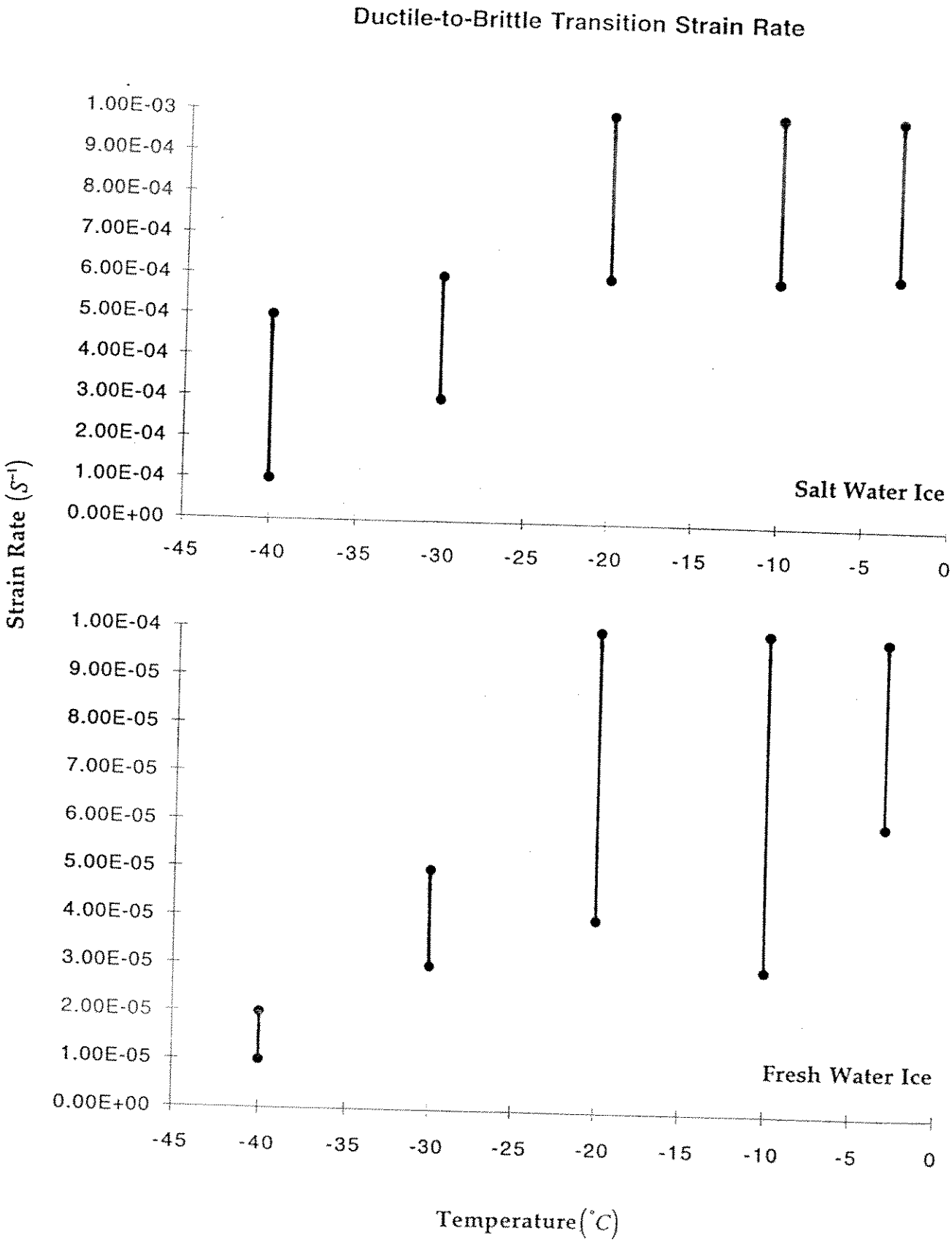
Ductile-to-Brittle Transition Strain Rate
Strain Rate (S^{-1})
1.00E-03
9.00E-04
8.00E-04
7.00E-04
6.00E-04
5.00E-04
4.00E-04
3.00E-04
2.00E-04
1.00E-04
0.00E+00
Salt Water Ice
-45
-40
-35
-30
-25
-20
-15
-10
-5
0
1.00E-04
9.00E-05
8.00E-05
7.00E-05
6.00E-05
5.00E-05
4.00E-05
3.00E-05
2.00E-05
1.00E-05
0.00E+00
Fresh Water Ice
-45
-40
-35
-30
-25
-20
-15
-10
-5
0
Temperature ($^{\circ}C$)

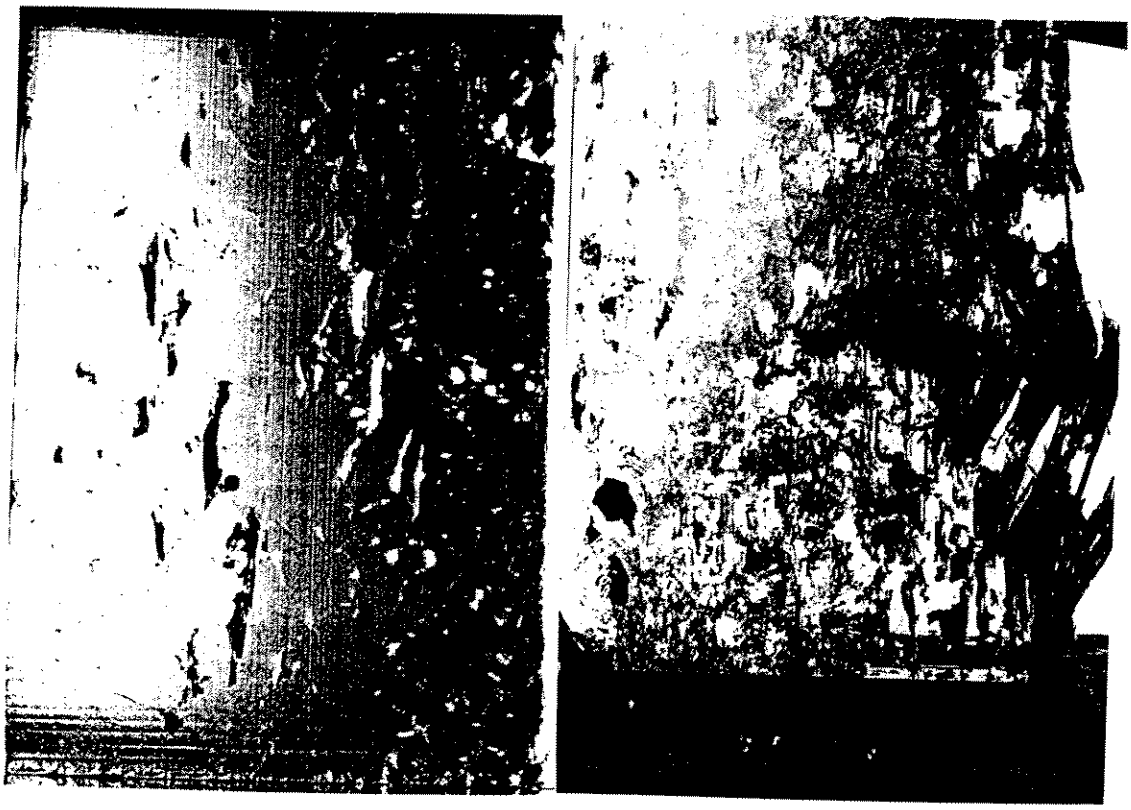

Fresh Water Ice $\dot{\varepsilon} = 4 \times 10^{-5} s^{-1} at -20^{\circ}C$

Fresh Water Ice $\dot{\varepsilon} = 6 \times 10^{-5} s^{-1} at -20^{\circ} C$

Calculated Activation Energy Q

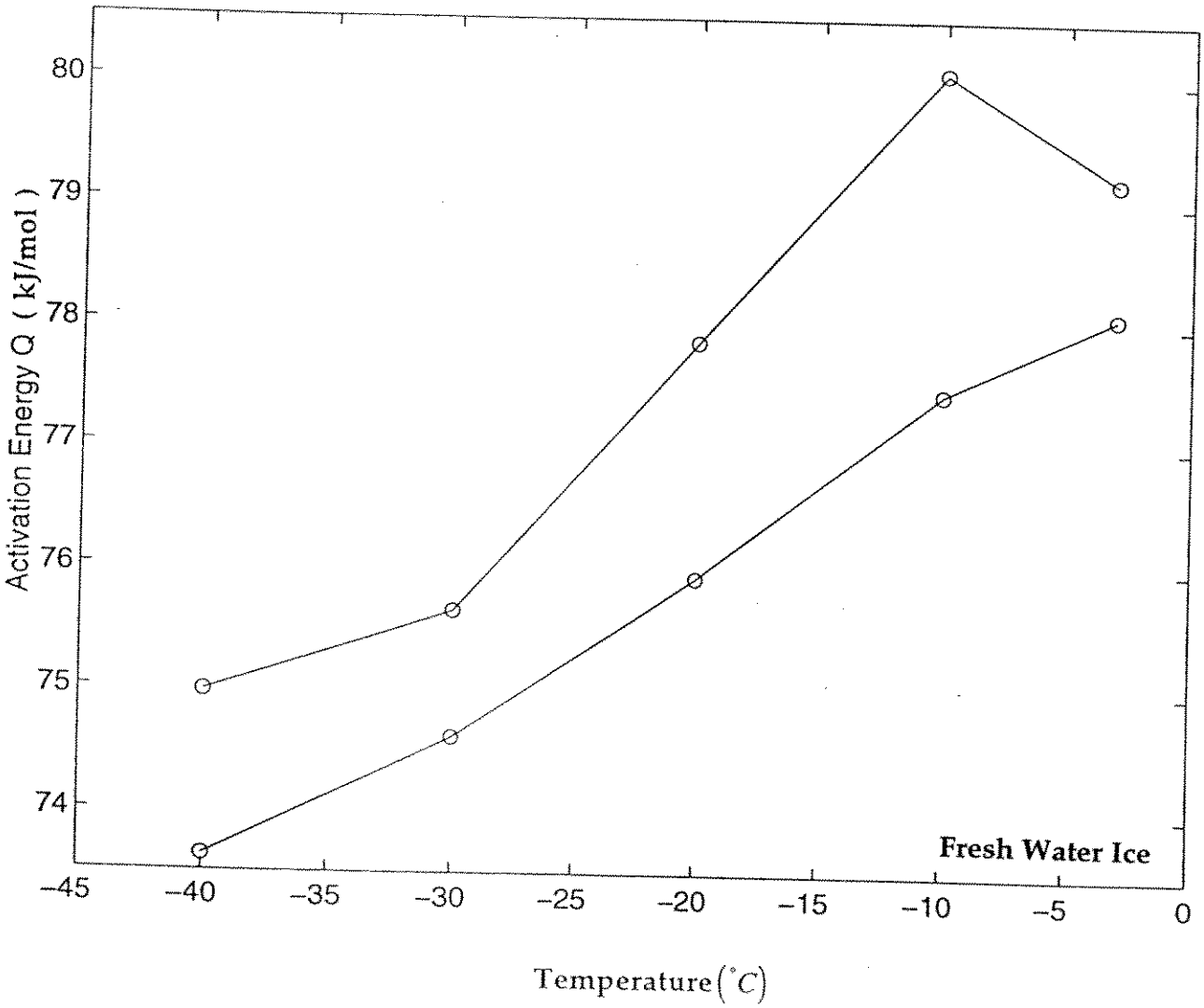

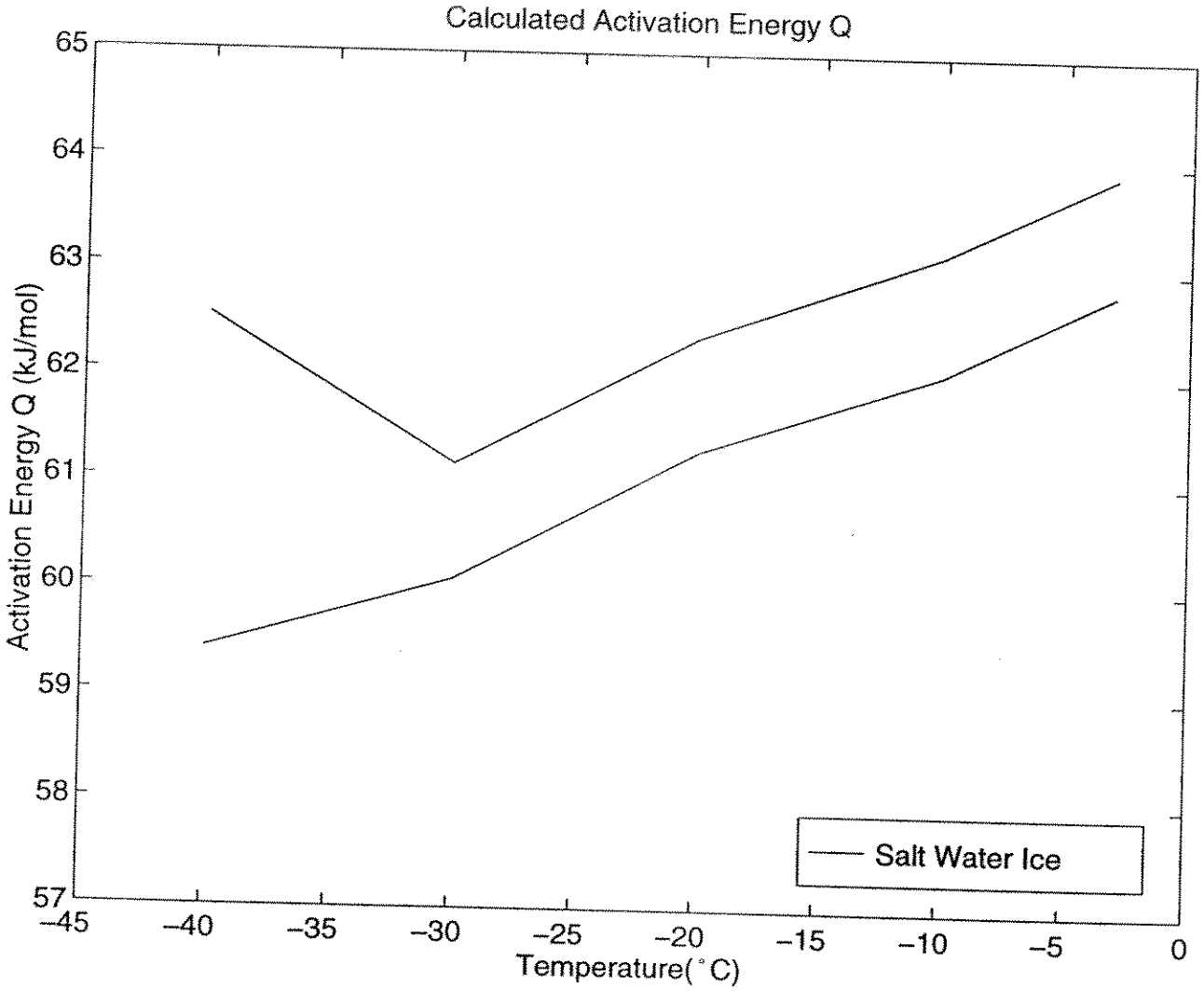
Calculated Activation Energy Q
Activation Energy Q (kJ/mol)
65
64
63
62
61
60
59
58
57
−45
−40
−35
−30
−25
−20
−15
−10
−5
0
Temperature(°C)
Salt Water Ice

The Effect of Confinement on the Brittle Indentation Failure of Ice

Johan A. Grape and Erland M. Schulson

1 Introduction

It is now well established that confinement across the columns causes an increase in the failure strength of S_2 ice, by inhibiting the propagation of splitting cracks from wing-cracks, and finally suppressing damage formation from inclined cracks to such a degree that out-of-plane failure, with splitting perpendicular to the column direction becomes the principal failure mode [1]. The present study considers the relationship between confinement and indentation failure loads when a plate of virgin ice is loaded across the columns by a flat indenter. These results are of some significance because they provide insight into the effect that the natural constraint of geometry has on failure mode and hence indenter load. In larger-scale ice-structure interaction problems, the relationship between structure width and floe-size will dictate the mode of failure, and in the process zone near the structure the fracture loads will be dependent on the uniformity of the interface and the constraint provided by the geometry of the ice. Previous studies of this problem have focused on fully constrained plates [2, 3], or free-floating ice-sheets at 0°C [4, 5], but not one of them has considered the effect of variable constraint on the modes of failure.

2 Experimental results

The experiments performed here are illustrated in figure 1. The plates were of in-plane dimensions approximately 200mm (x) by 150mm (z) and a thickness of 38mm. Experiments were also performed on 102mm thick specimens to establish whether ice thickness affected failure strength. The indenter was made from solid aluminum and was 38.1 mm wide ($2b$). The indenter edges had been rounded to reduce stress-concentrations that could lead to premature failure. The grain size of the ice ranged from 2.1 mm to 6.1 mm, such that the indenter was minimum of 6 grain-diameters wide. The experiments were performed in the

(50)

MATS by applying a confining stress along the x direction and applying the indentation load along the long (200 mm) side of the plate, such that the indentation motion was along the (z) direction. The confinement was applied in three ways: preset constant stress, proportional to load on the indenter and rigid (ie. plane strain). The proportional loading was performed to emulate an infinite sheet, by allowing the constraining stress to increase as the plate deformed, while the rigid conditions were used to classify whether the response was elastic, and for comparison with previous studies of this nature. Experiments were performed at temperatures of -3°C, -10°C and -40°C at a strain rate of 10^{-3}, determined by the equation $\dot{\epsilon} = v/2b$, where v is the rate of indenter propagation and $2b$ the width of the indenter. This strain rate was chosen because it leads to brittle behavior under uniaxial loading, while remaining slow enough to allow easy observation of damage development. However, in order to compare with true brittle behavior, experiments were also performed at an indentation strain rate of 10^{-2}at -10°C.

Each "puck" of ice grown for use in these experiments was characterized by performing uniaxial compression experiments at the testing conditions at which indentation tests on the ice were to be performed. It was found that at all conditions, the failure mode was characteristically brittle, driven by the formation of wing-cracks and failure through splitting along the loading direction.

Figure 2 and 3 show indenter pressure versus displacement curves for selected experiments performed at various confining stresses at -10°C at the low (10^{-3}) and high (10^{-2}) strain rates. The results show that increasing confining stress causes higher indenter pressure at failure, and also results in more characteristically ductile behavior in the low-rate experiments. Overall, it was found that the experiments at -3°C and -10°C at the lower strain rate resulted in ductile response, while the other conditions showed brittle failure. In addition, it was found that the thick plates (102mm) showed the exact same response as the thinner plates.

The confining stress affects failure strength in a manner analogous to that observed for biaxial compression. That is, failure separates into two regimes. At confining stresses less than about 25% of the uniaxial compressive strength of the ice, the indenter pressure at failure was linearly dependent on the applied confinement, and failure was through the formation of shear-faults under the indenter and the propagation of cracks along planes oriented parallel to the column direction. At the lowest confining stresses, these

cracks would lead to splitting of the ice plates, and progressively higher compressive confinement would reduce the propagation of these cracks and lead to more damage in the ice near the indenter. At confining stresses above the threshold value, this failure mode was suppressed, and failure was through the propagation of in-plane cracks, leading to spallation failure of the ice near the indenter.

Figure 4 shows the maximum indenter pressure recorded in the experiments for all conditions and rate studied. It is clear that the strength of the ice increases with decreasing temperature, and it can be seen that the indenter pressure at failure is at first approximately linearly dependent on confining stress, but that this dependence vanishes when the confinement reaches a certain value. More general conclusions are possible when considering this data normalized with respect to the uniaxial compressive failure strength (σ_{ult}), shown in figure 5. The normalization has been done for each point relative to uniaxial compression data for the same puck of ice and testing conditions. At confining stresses below 20% of the uniaxial strength, the maximum indenter pressures for all conditions show a nearly identical linear dependence on the confining stress. However, the transition to the out-of-plane failure mode, characterized by a constant maximum indenter pressure with increasing confining stress, occurs at a lower confining stress relative to the uniaxial failure stress for the tests in which the response was brittle (-10°C, $\dot{\epsilon} = 10^{-1}$ and -40°C, $\dot{\epsilon} = 10^{-3}$). It can be seen that the transition in the experiments where the response was ductile occurs at a confining stress approximately equal to 25% of the uniaxial strength.

The results show that the magnitudes of indentation loads to crush virgin ice are inherently dependent on the deformation mechanism that is active in the ice. If conditions lead to brittle failure, the loads can be expected to be significantly lower than under ductile deformation rates at the same temperature. It is also clear that the transition in failure mode and the absolute magnitudes are dependent on the confinement of the ice in the indentation process zone.

3 Projection of results onto variable geometries

We have pursued analysis to determine how the experiments described above compare with loading of larger ice-plates, in order to suggest where these results fit in larger-scale problems. We studied the relationship between the geometry of the plates studied here, and the deformation of an infinite plate under the

action of an indenter. As mentioned above, cracking initiated away from the indenter, indicating no significant stress concentrations at the indenter edges. It was therefore deemed that the most accurate depiction of this particular indentation problem was one of a constant pressure on the face of the indenter. The stress-field in the plate due to this loading is readily available[6], and is shown in figure 6. Also shown in the figure is the plate superimposed on the stress-field. Averaging the stresses along the lateral boundaries of the specimen provided a ratio of 5.5% of the indenter pressure. A number of experiments were performed using this proportional loading scheme at the conditions $T = -10°C$, $\dot{\epsilon} = 10^{-3}$. The results are shown in figure 7 and show that from these results, the loading of an infinite plate appears to fall in the regime where indenter failure pressure is linearly dependent on the confining stress. This means that a slight increase in constraint of the ice could lead to substantial increases in indenter pressures.

Loading was also performed with rigid boundaries to determine how large the stresses on the boundary would become under indentation of a fully constrained plate. In this case the plate was preloaded with a slight confining stress of about 0.1 MPa, and the platens then locked in place. This loading path is essentially equivalent to a plane- strain condition in the in-plane direction transverse to the indenter motion (x). These tests resulted in failure through the out-of-plane failure mode, and confining stresses above the threshold value to initiate this failure mode. They also showed that in the experiments where the deformation was ductile, an inelastic response was clearly evident, as the ratio of boundary stresses to indenter pressure increased throughout the test, rather than maintaining a single value, which would indicate elastic deformation. Figure 8 shows the load-history of a typical set-boundary experiment in which brittle behavior was observed. It can be seen that the ratio of confining stress to indenter pressure stabilized, and hence it is clear that the deformation is elastic. The ratio of confining stresses on the boundary to indenter pressure is about 5% and in remarkable agreement with the analytical solution given above.

The plate was also simulated using a finite element model, which was compared to the analytical solution for an infinite plate to determine which confining stress best approximated the stress-state in an infinite plate. Through comparison of the stress-fields in the finite element model and the analytical model, it was determined that the best fit was achieved with a confining stress in the numerical model that was 8% of the indenter pressure. Figure 9 shows a comparison of the in-plane stresses along the centerline $x = 0$

between the two models, and it gives reasonable agreement. A comparison of the predicted load-paths of the two models is shown in figure 10, and it shows that both solutions indicate that the indenter failure pressure for an infinite plate falls in the region where increasing confinement has the effect of increasing the failure load. This is a significant result, as it indicates that in the process-zone during larger-scale interaction problems, additional confinement can lead to increased loads, while similarly, relieving local confinement can lead to significant reduction in the failure loads.

4 Conclusion

We have studied the effect of lateral constraint on the indentation of damage-free columnar freshwater ice by a flat indenter. We found that constraint has an effect similar to that observed by Smith and Schulson [1] for biaxial compression, in that the constraint increases the maximum load measured on the indenter by suppressing the mechanism of failure through radial cracking away from the indenter leading to plate splitting. Through experimentation and comparison with analytical and numerical models, it was found that the indentation of an infinite plate would lead to failure in the regime where maximum indenter pressure is dependent on confining stress.

References

[1] T. Smith, E. M. Schulson, *Acta Metall. mater.*, Vol. 41, No. 1, pp 153-163, 1993

[2] R. Frederking, L. W. Gold, *Canadian Geotechnical Journal*, Vol. 12, p. 456, 1975

[3] B. Michel, N. Toussaint, *Journal of Glaciology*, Vol. 19, No. 81, pp. 285-300, 1977

[4] B. Michel, D. Blanchet, *Annals of Glaciology*, Vol 4, pp. 180-187, 1983

[5] G. W. Timco, *Proceedings, OMAE 1986*, Vol. 4, pp. 444-452, 1986

[6] S. P. Timoshenko, S. N. Goodier, *Theory of Elasticity*, McGraw-Hill, 1970

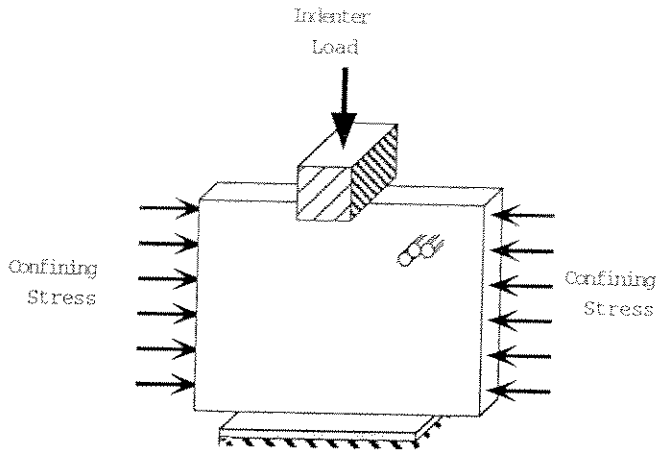

Figure 1: Schematic of the indentation loading in the MATS

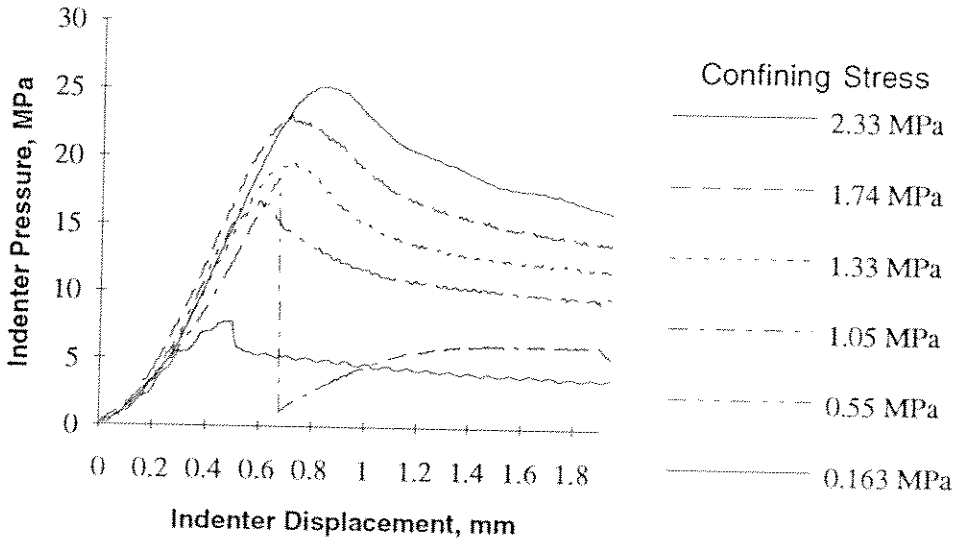

Figure 2: Indenter pressure vs. displacement typical for experiments performed under conditions that resulted in ductile behavior.

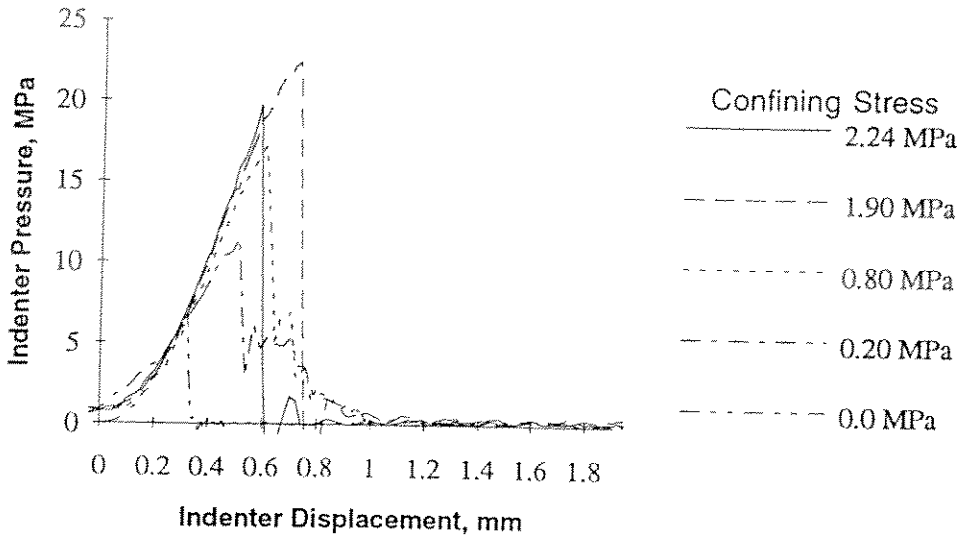

Figure 3: Indenter pressure vs. displacement typical for experiments performed under conditions that resulted in brittle behavior.

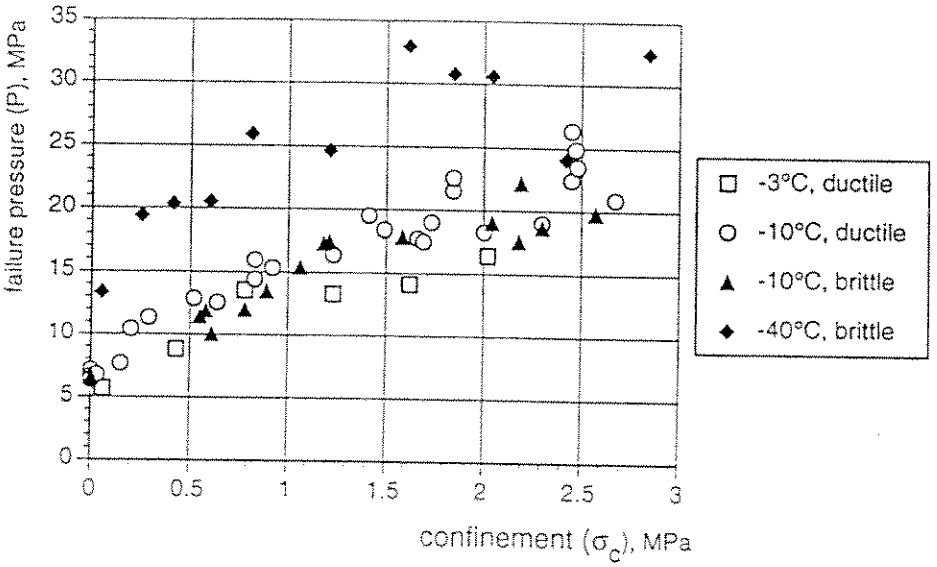

Figure 4: Comparison of maximum indenter pressure for all conditions tested

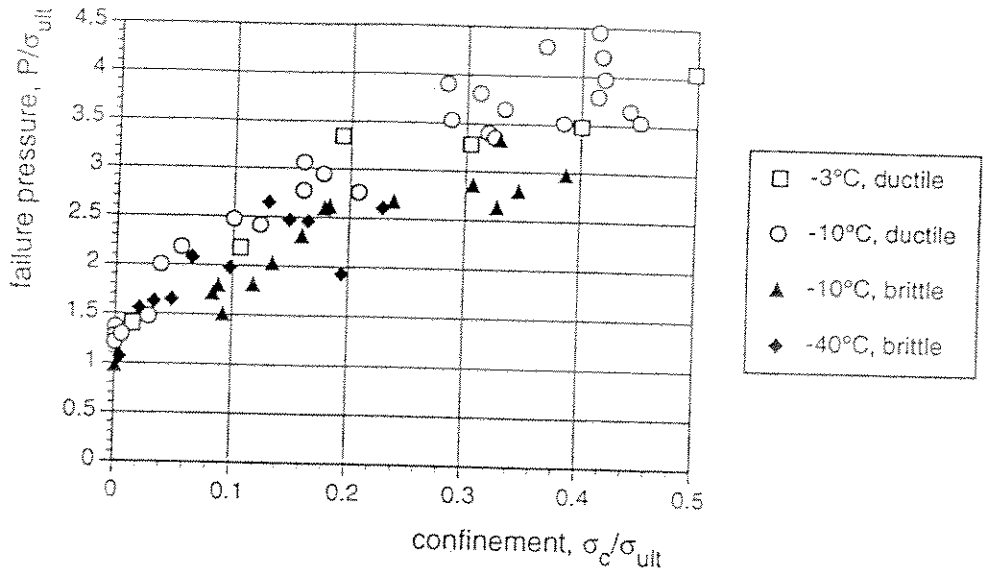

Figure 5: Comparison of indenter pressures and confining stress normalized with respect to the uniaxial compressive failure strength of the ice at the conditions tested.

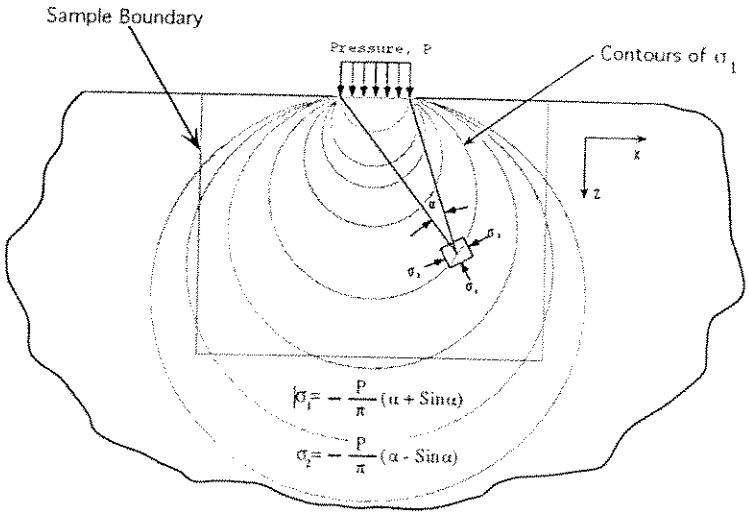

Figure 6: Experiments simulating the stress-field in an infinite sheet were performed by applying a confining stress proportional to the indenter pressure determined by superimposing the specimen on the stress field in an infinite plate and averaging the stresses along the lateral boundaries of the specimen.

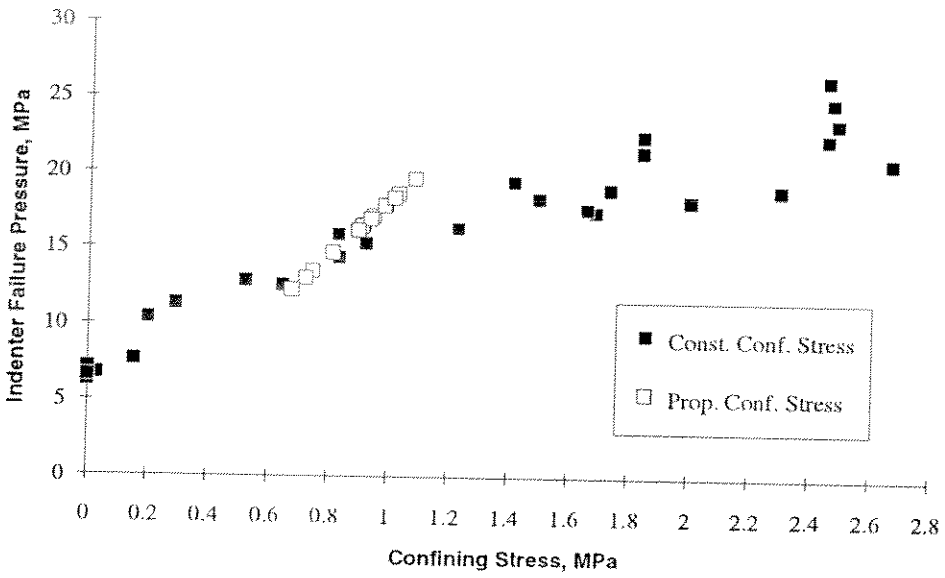

Figure 7: Indenter failure pressure for proportional loading shown with const. conf. stress data, indicating that the loading of an infinite plate falls within the region where failure stress is linearly dependent on confining pressure

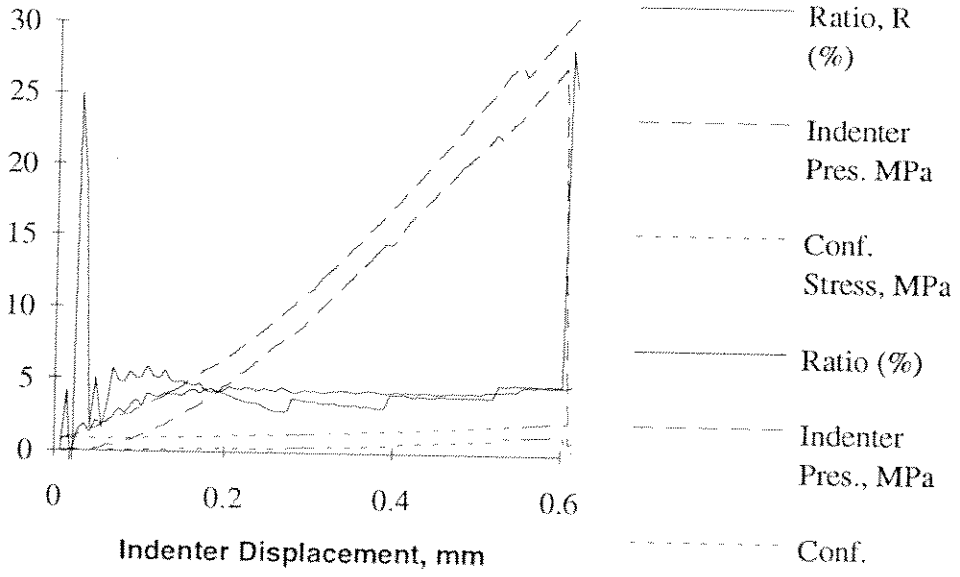

Figure 8: Stress versus displacement curve for an experiment with rigid boundaries. The ratio of confining stress to indenter pressure (R) is constant after the speed of the indenter becomes constant, indicating elastic behavior. The ratio is approximately 5%, in good agreement with analytical models.

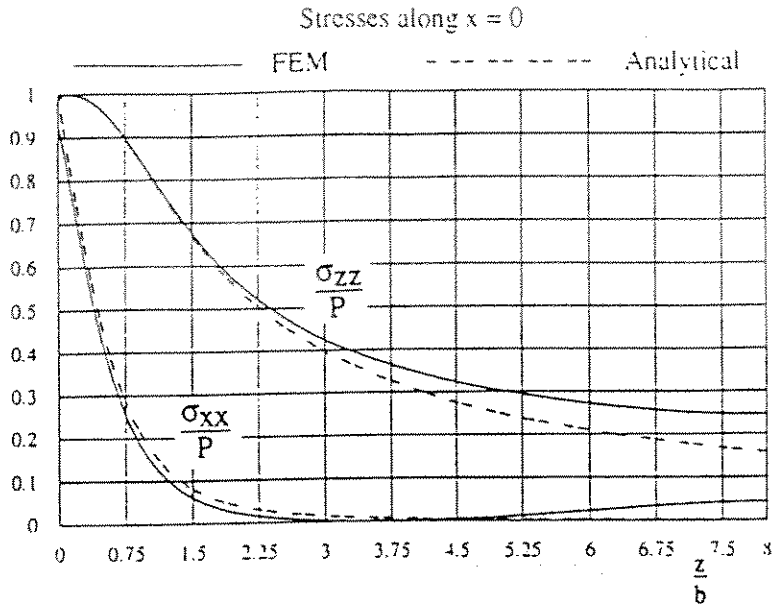

Figure 9: Best fit of stresses directly in front of the indenter was determined by finite element analysis of a specimen and comparison with the analytical model. The confining stress is 8% of the indenter load.

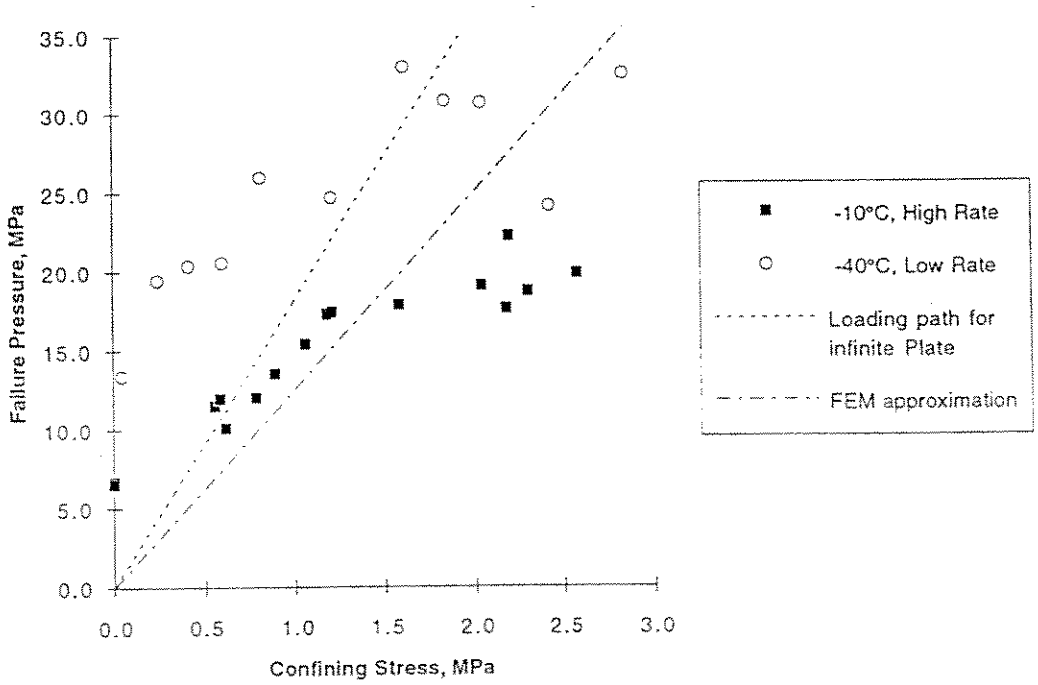

Figure 10: Predicted loading paths of the infinite plate superimposed on the results from the brittle indentation tests. The lines indicate the bounds of the analytical and numerical models.

Brittle Indentation Failure of Ice

by

Sang-Ryong Ko and Eric Gratz

ABSTRACT

Preliminary tests have been conducted at the Ice Research Laboratory concerning the brittle indentation failure of fresh-water columnar ice loaded under a spherical indentor. The ice was grown according to standard laboratory procedures which results in columnar ice with an average grain size of about 6 mm. Cube-shaped samples with nominal dimensions 152 mm on edge were prepared from the ice. A uniaxial MTS servo-hydraulic testing system was used to press a stainless steel sphere, 25.4 mm in diameter, into the ice in a direction perpendicular to the long axis of the columnar shaped grains. Figure 1 shows a schematic sketch of the loading geometry used and Figure 2 shows the experimental setup. The indentor speed was 0.038 m/s and the resulting load was measured using a computerized data acquisition system. Figure 3 shows the indentor load-displacement curve for one of the tests. Load increased as the indentor was displaced into the ice until brittle failure, i.e. a sudden decrease in load, was observed. Typically, samples exhibited repeated failure events with continued indentor displacement. Deformation damage included cracking into the bulk of the sample, crushing under the indentor, and spallation from the sample surface. Table 1 lists the peak loads and corresponding displacements for two tests conducted under identical conditions.

Table 1. Indentor load and displacement at peaks in the load-displacement curves.

	Test 1		Test 2	
	1st Peak	2nd Peak	1st Peak	2nd Peak
P (kN)	5.5	7.05	2.74	5.2
δ (mm)	0.38	0.87	0.41	1.57

The stress-state under the indentor was modeled using the Hertzian formulation.

The original Hertz analysis gave explicit quantitative consideration to only the surface stress condition [1]. The radius of the circular elastic contact, a is given by

$$a = \left(3PR/4E^*\right)^{1/3} \qquad (1)$$

where P is the applied normal load, R is the radius of indentor and E^* is given by

$$1/E^* = \left(1-\upsilon_1^2\right)/E_1 + \left(1-\upsilon_2^2\right)/E_2$$

the Young's modulus of E_1, E_2 and Poisson's ratio υ_1, υ_2 of sample and ball, respectively.

Displacement, δ is given by

$$\delta = a^2/R = \left(9P^2/16RE^{*2}\right)^{1/3} \qquad (2)$$

The total load compressing the indentor and sample is related to the pressure by

$$P = (2/3)\,P_o/\pi a^2 = \left(6PE^{*2}/\pi^3 R^2\right)^{1/3} \qquad (3)$$

where P_o is the pressure in the center of the loaded circle.

Equations 2 and 3 were used to calculate values of P_o from the data listed in Table 1. The values of the pressure in the center of the loaded circle, P_o, ranged from 125 MPa to 545 MPa, pressures which are much greater than the approximately 100 MPa pressure required to melt ice at -10°C. The possibility exists that pressure melting plays some role in brittle indentation failure of columnar ice. However, the magnitude of the pressures under the indentor prompted us to conduct additional testing to judge the validity of applying Hertzian analysis to predict the pressures under the indentor.

Two tests were conducted using pulse loading. The rate of loading and unloading was 0.5 kN/s, approximately equal to the loading rate in the displacement controlled tests. Triangular pulses up to 1 kN, 2 kN, 3kN, etc. were applied until failure, and sufficient time was allowed between pulses to observe the crack patterns under the indentor. Figure 4 shows one of the load-displacement curves obtained. The hysteresis in the load-displacement curve clearly indicates that the behavior of the ice is not purely elastic while Hertzian contact analysis assumes elastic behavior. Cracking prior to failure was observed under the indentor which could account for some of the

permanent deformation. Cone cracks, typically associated with spherical indentation of elastically isotropic brittle solids (like glass), were not observed. Instead radial fan cracks, as shown in Figure 5, were observed which cut the columns. In some tests, these fan cracks split the sample as shown in Figure 6. As mentioned before, spallation and crushing were also observed. Creep is also likely to play a role in the deformation at the temperature and rate used in this study.

Clearly, the brittle indentation failure in columnar ice we observed is not strictly Hertzian in nature. Cracking prior to failure is observed and permanent deformation, due to cracking and possibly plasticity, may also be an important part of the failure process.

References

1. K.L. Johnson, 1985, *Contact Mechanics*, pp. 84-106.

Figures

Fig. 1	A schematic sketch of the loading geometry.
Fig. 2	A picture of experimental set up.
Fig. 3	Load-displacement curve (monotonic loading).
Fig. 4	Load-displacement curve (pulse loading).
Fig. 5a, b, c	Pictures and sketch of crack phenomena.
Fig. 6	Picture showing fan cracks split.

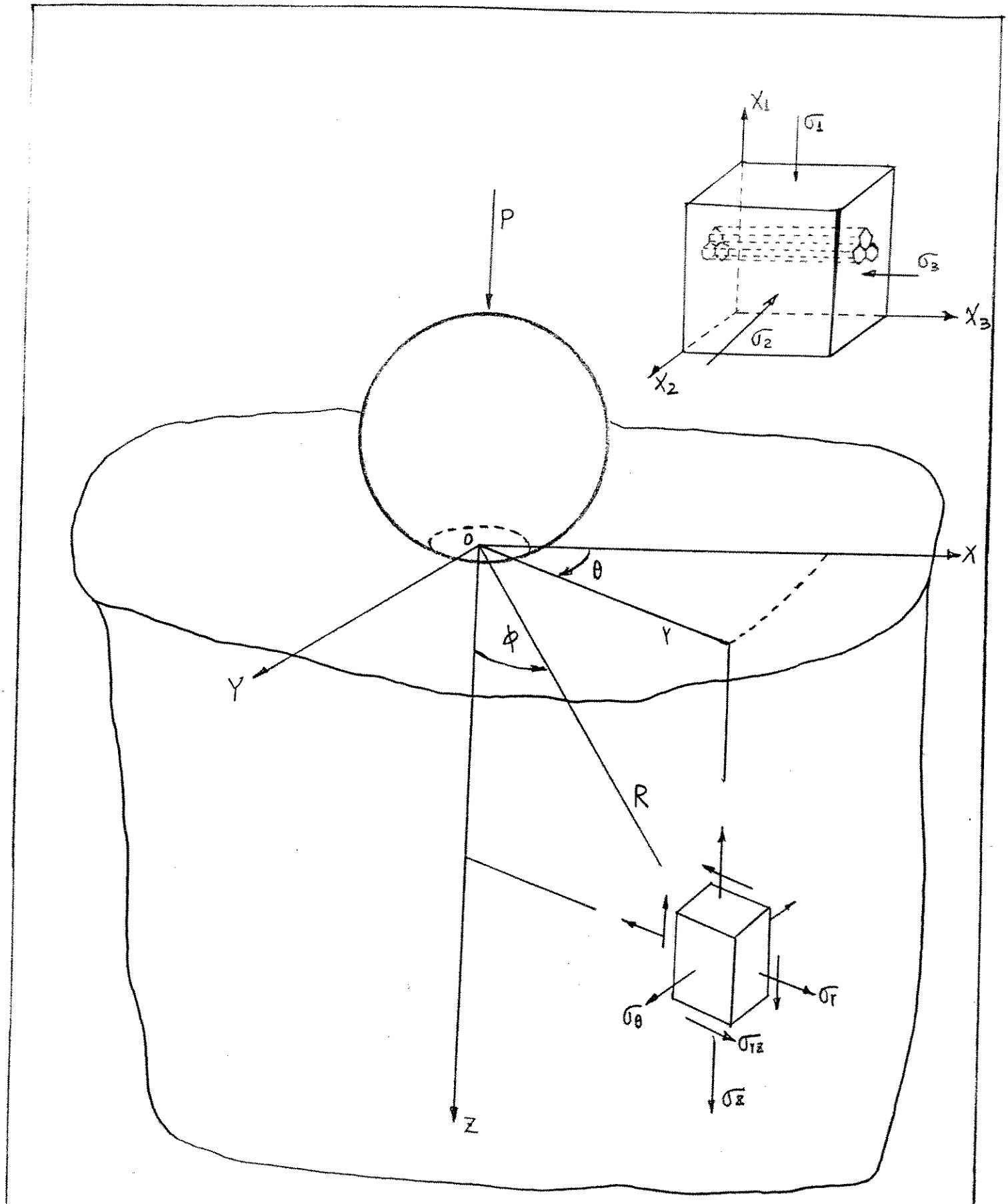

Figure 1

Figure 2

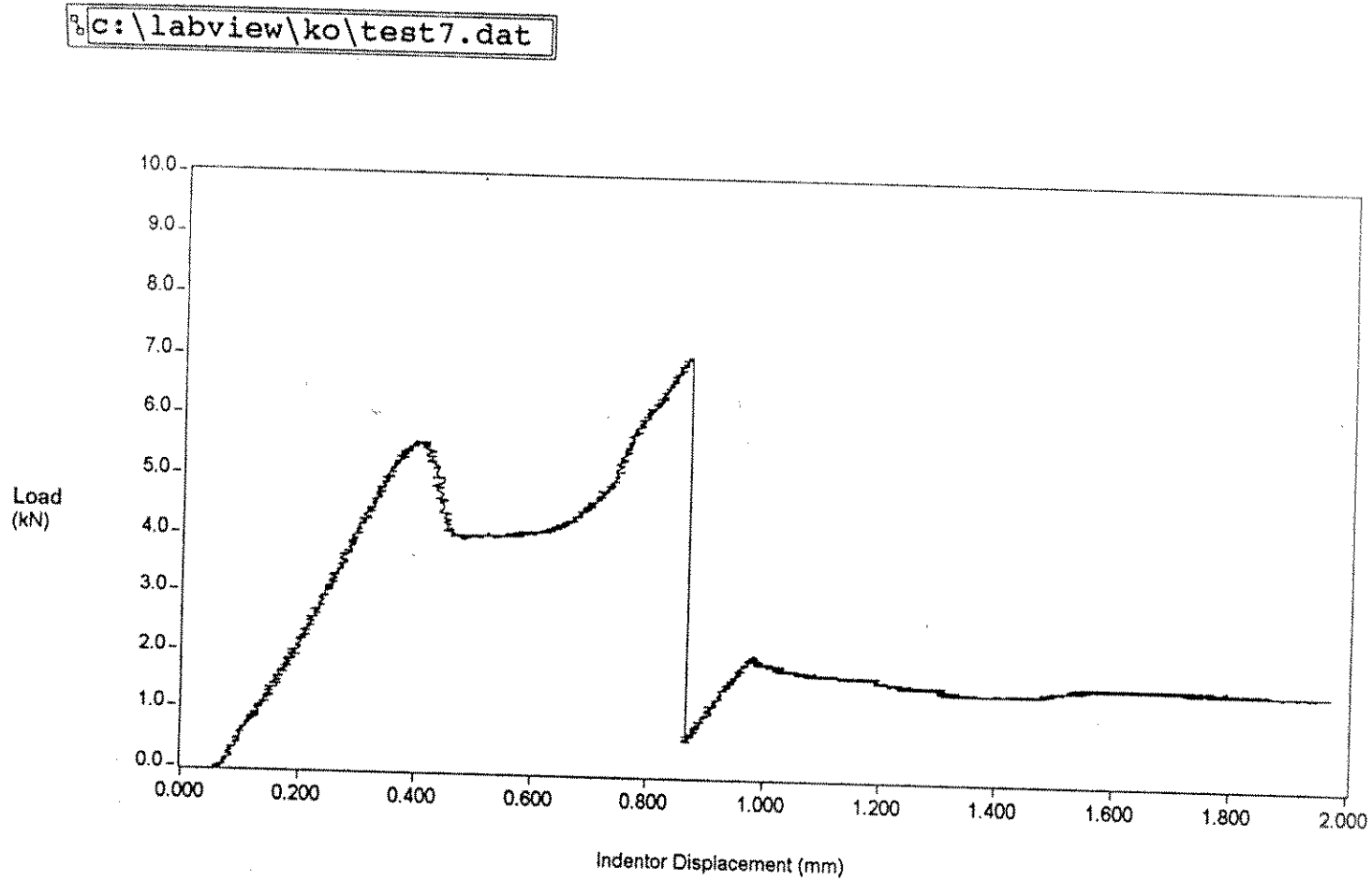
c:\labview\ko\test7.dat
Load
(kN)
10.0
9.0
8.0
7.0
6.0
5.0
4.0
3.0
2.0
1.0
0.0
0.000
0.200
0.400
0.600
0.800
1.000
1.200
1.400
1.600
1.800
2.000
Indentor Displacement (mm)

Figure 3

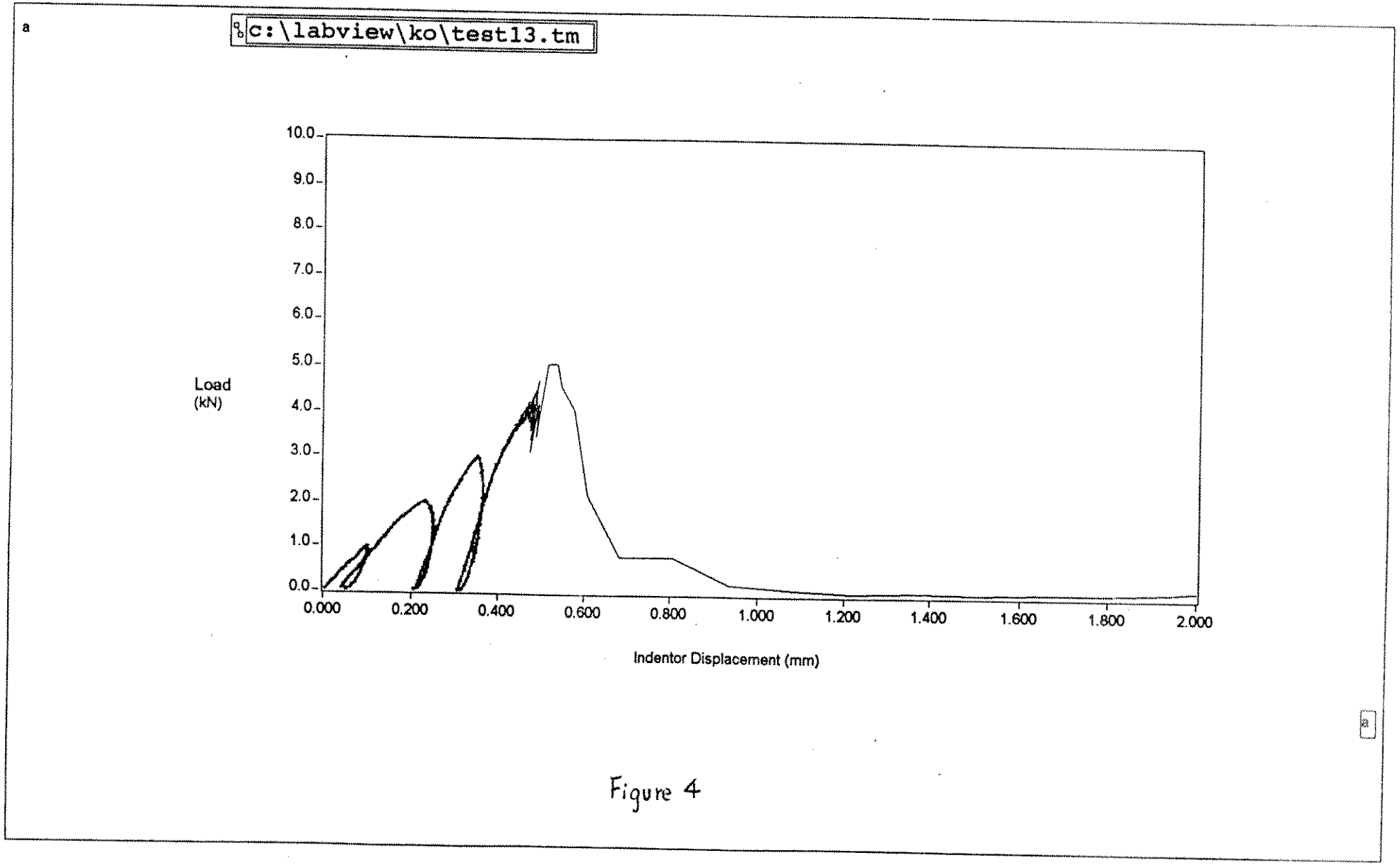
a
c:\labview\ko\test13.tm
Load
(kN)
10.0
9.0
8.0
7.0
6.0
5.0
4.0
3.0
2.0
1.0
0.0
0.000
0.200
0.400
0.600
0.800
1.000
1.200
1.400
1.600
1.800
2.000
Indentor Displacement (mm)

Figure 4

Figure 5a

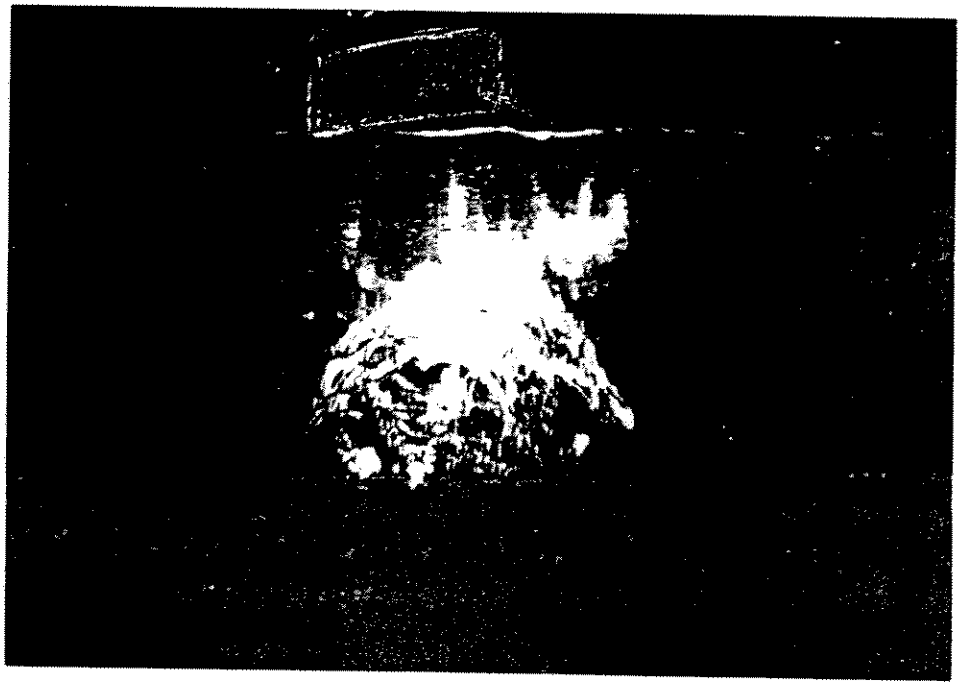

Figure 5b

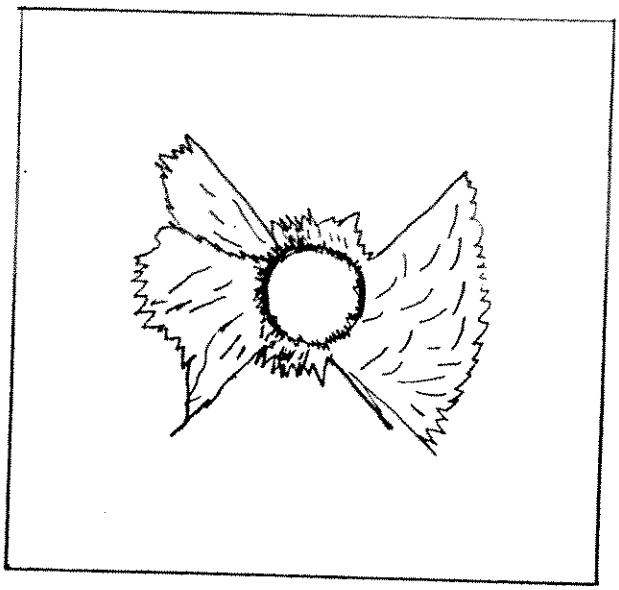

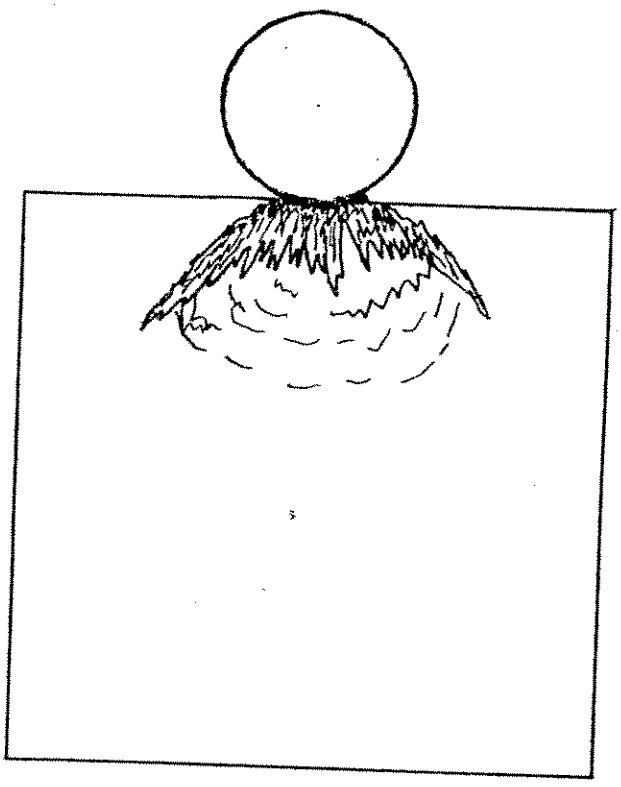

Figure 5c

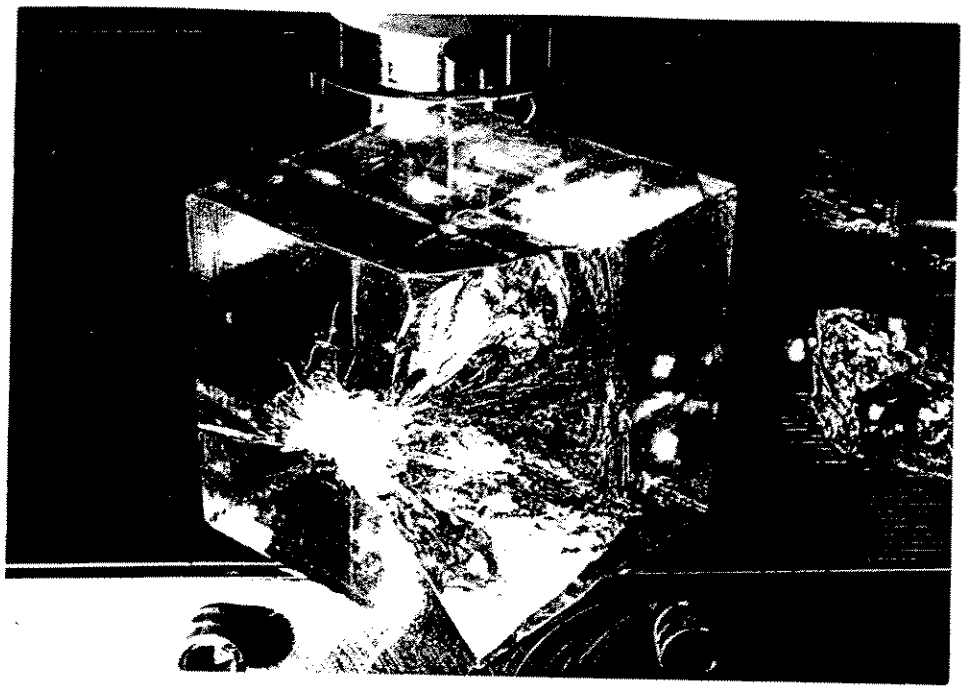

Figure 6

A New Method to Achieve Increased Hydrostatic Loading Using the Multiaxial Testing System

Jeffrey S. Melton, Eric T. Gratz and Erland M. Schulson
Ice Research Laboratory
Thayer School of Engineering
Dartmouth College, Hanover, NH 03755

One active area of research at the Ice Research Laboratory is focused on outlining the triaxial compressive failure surface of columnar S2 ice for both brittle and ductile behavior (Melton and Schulson 1995, 1997, Gratz and Schulson 1997). The samples are loaded in triaxial compression using an MTS true triaxial testing system. The multi-axial testing system (MATS) has three sets of servo-hydraulic actuators to load cube shaped specimens. Each pair of actuators can be controlled independently or programmed to apply proportional loading. For the tests reported here, the compressive failure strength was investigated at -10 °C at constant strain rates that ranged from 4×10^{-5} s^{-1} to 1×10^{-2} s^{-1}. All of the tests were carried out on 159mm or 160mm cubic samples prepared from freshwater ice or saline ice grown in the laboratory. The samples were proportionately loaded with confinement ratios $R_{21}=\sigma_{22}/\sigma_{11}$ and $R_{31}=\sigma_{33}/\sigma_{11}$ variable; σ_{11} and σ_{22} are normal stresses applied in two orthogonal directions across the columns and σ_{33} is applied along the columns. The loads were applied through brass brush-type platens similar to the platens used by Häusler (1981).

One consequence of using our true triaxial testing system is that the edges of the sample must remain unloaded to prevent the platens from coming into contact with each other as the sample deforms. This loading condition leads to large stress concentrations near the edges, which appears to cause premature failure of samples under high confinement. This failure mode, which occurs in both the brittle and ductile regimes, is called end crushing and it is usually observed to occur under near hydrostatic loading. It is characterized by crushing or severe cracking just below the surface of one or more faces of the sample. The damage is localized to 1-2 cm below

the surface and does not represent the overall response of the ice. This localized failure is the limiting factor in trying to map out the complete triaxial failure surface. Figure 2a shows the across-column failure stress $\sigma_{11,f}$ versus the across-column confining stress $\sigma_{33,f}$ for tests conducted at a strain rate of $1x10^{-2}$ s^{-1}. The across-column stresses were equal (R_{21}=1) and the failure stress was observed to rise rapidly for very small along-column confining stresses, but then reached a plateau of about 15 MPa at higher along-column stresses. End crushing was noted for tests along the plateau. Figure 2b shows results in the ductile regime for the same loading paths, except at a strain rate of $4x10^{-5}$ s^{-1}. Again, the failure stress increases with increasing along-column confinement until at R_{31}>0.2 end crushing sets in and this causes large distortions of the brush platens, leading to questionable results.

Gratz, working with frozen soil, encountered similar problems resulting from the presence of non-loaded edges. In these tests, frozen soil was extruded into the gaps between the loading platens. To reduce the extrusion 0.008 inch thick brass strips were used to reinforce the edges of the samples thereby reducing the area available for extrusion. The edge reinforcements were made from strips of brass bent lengthwise forming 90° angles which were adhered to the edges. Reinforcing the edges was successful in reducing the extrusion area with delayed the onset of extrusion to higher hydrostatic pressures.

Edge reinforcement was subsequently used in the study of ice. Figure 3a shows the effects of the edge confinement on the behavior of ice in the brittle regime. The failure stress of the edge reinforced samples continuously rises with increasing along column confinement. The highest failure stress reached was 35

MPa, an increase of 20 MPa compared to the non-reinforced results. One test, shown with an arrow in Figure 3a, was hydrostatically loaded. The strength of the sample exceeded the limits of the machine, with a strength of 37.5 MPa recorded before the testing machine shut down. The hydrostatic pressure of 37.5 MPa is roughly 30 MPa higher than the hydrostatic pressure achieved in non-reinforced tests.

Figure 3b shows the preliminary results for the reinforced samples in the ductile regime. Note again the increase in failure stress with increase in along column confinement. These are not peak stresses since the tests had to be terminated before a peak occurred due to platen interaction. What happens is the pressure from ice causes the brass edge pieces to pull-out or burst, allowing the ice to flow into the brush platens causing the fingers to bend and interact. Currently we are working on that problem.

What these results show is that reinforced edges provide a method to achieve much higher hydrostatic pressures than can normally be achieved using the MATS. Additionally, tests with the reinforced edges performed at lower confinements give comparable results to tests performed without reinforced edges. This suggests that the observed behavior is an accurate reflection of the true response of the sample to triaxial loading. This gives credence to results obtained at higher confinements using the reinforced edge method. Continuing refinement of this method will allow testing at hydrostatic or near hydrostatic loading without premature failure due to end crushing.

References

Gratz, ET and Schulson, EM (1997). "Brittle Failure Of Columnar Saline Ice Under Triaxial Compression," *J Geophysical Research, Solid Earth,*, Vol 102, No B3, pp 5091-5017.

Häusler, FU (1981). "Multiaxial Compressive Strength Tests On Saline Ice With Brush-type Loading Platens," *IAHR Symposium Proceedings*, Quebec, pp 526-536.

Melton, JS and Schulson, EM (1997). "The Ductile Deformation of Columnar (S2) Saline Ice Under Triaxial Compressive Loading," *Proc ISOPE 97*, In Press.

Melton, JS and Schulson, EM (1995). "Preliminary Results On The Ductile Deformation Of Columnar Saline Ice Under Triaxial Compressive Loading," *Proc OMAE 95*, Vol 4, pp 139-143.

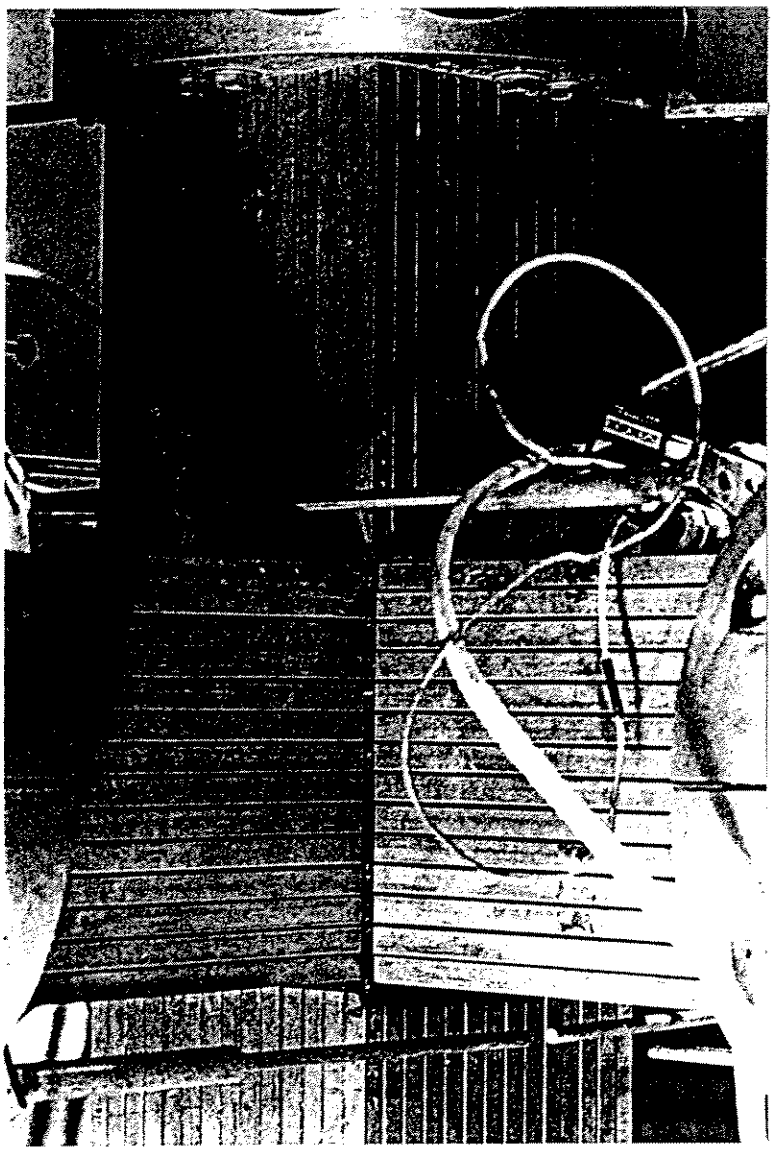

Figure 1. Photograph of a saline ice sample loaded in the MATS. The non-loaded edges can be seen between the brush platen edges.

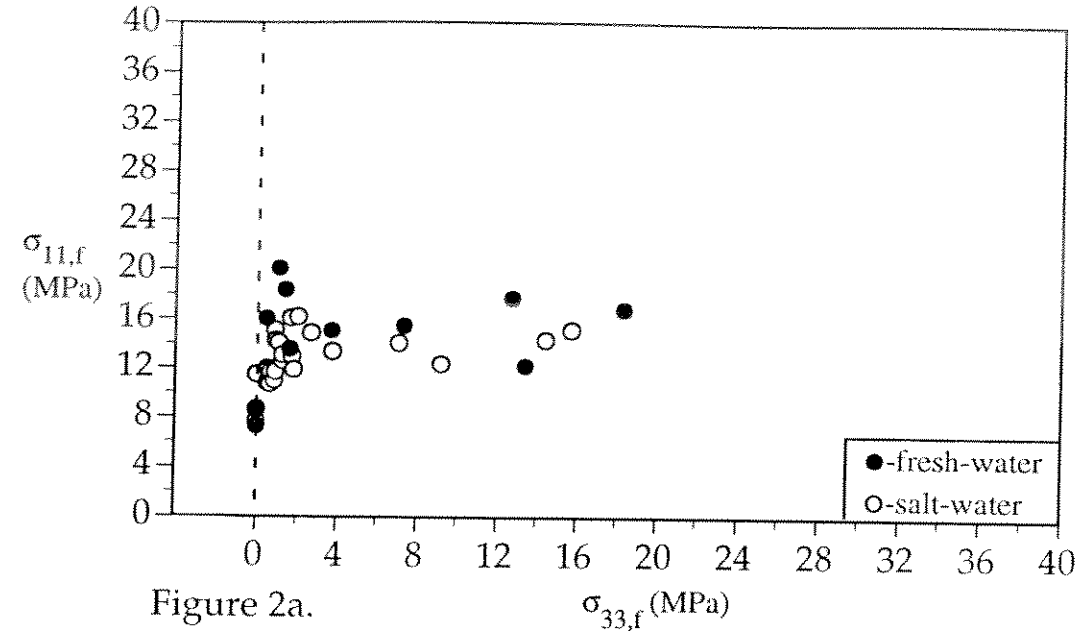

Figure 2a.

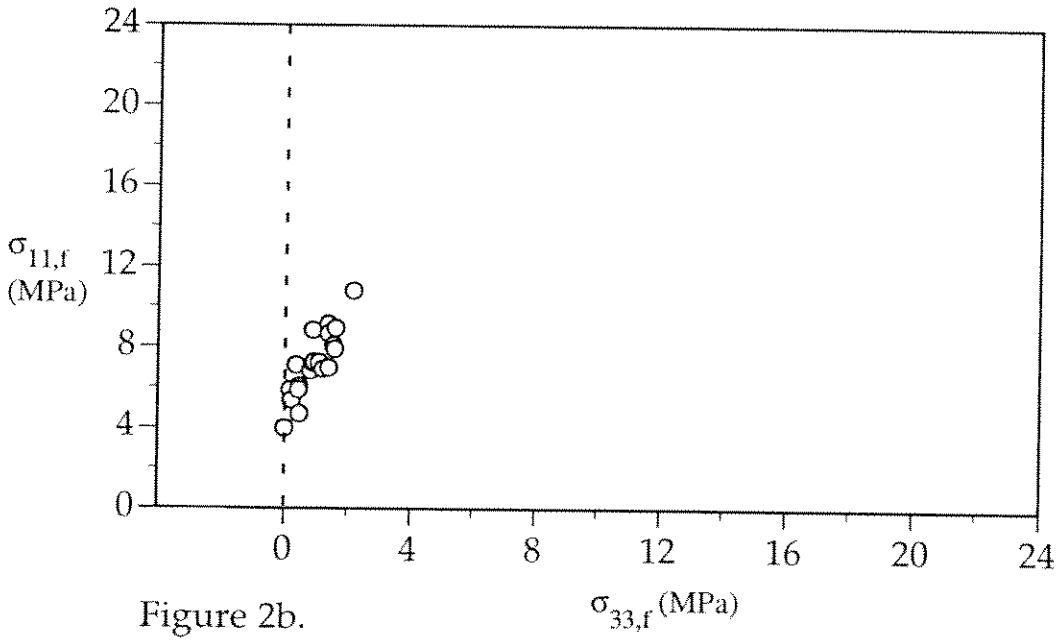

Figure 2b.

Figure 2. Shows the effect of along-column confinement (σ_{33}) on the across-column failure stress ($\sigma_{11,f}$) for full confinement across the columns. Brittle failure for both fresh and saline ice is given in 2a, while the ductile failure of saline ice is given in 2b. End failure prevents testing at an along-column confining stress greater than ≈3 MPa for both brittle and ductile regimes.

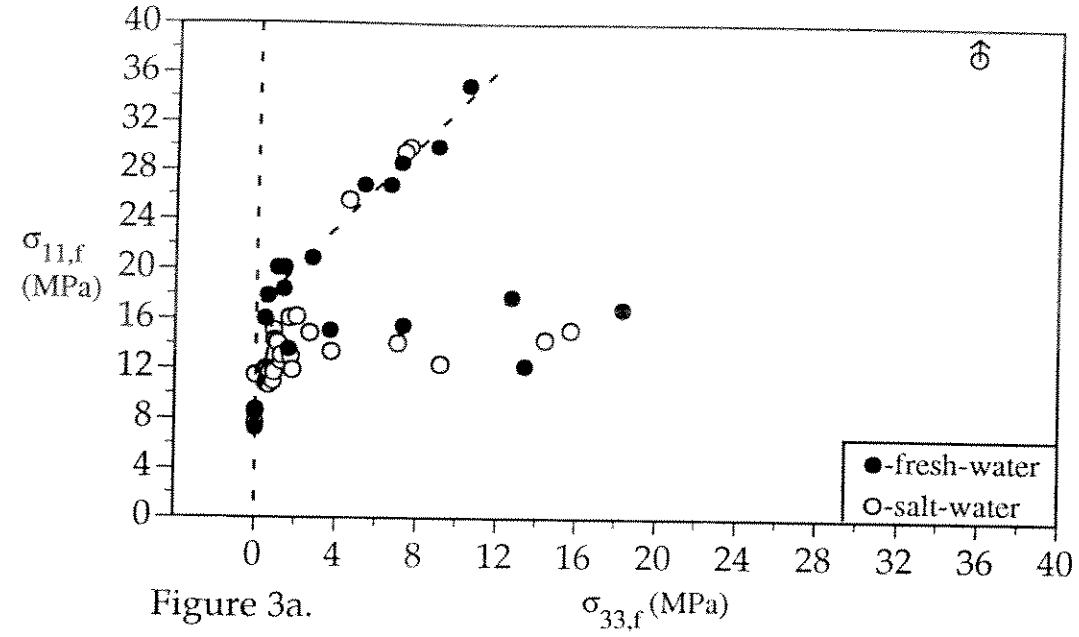

Figure 3a.

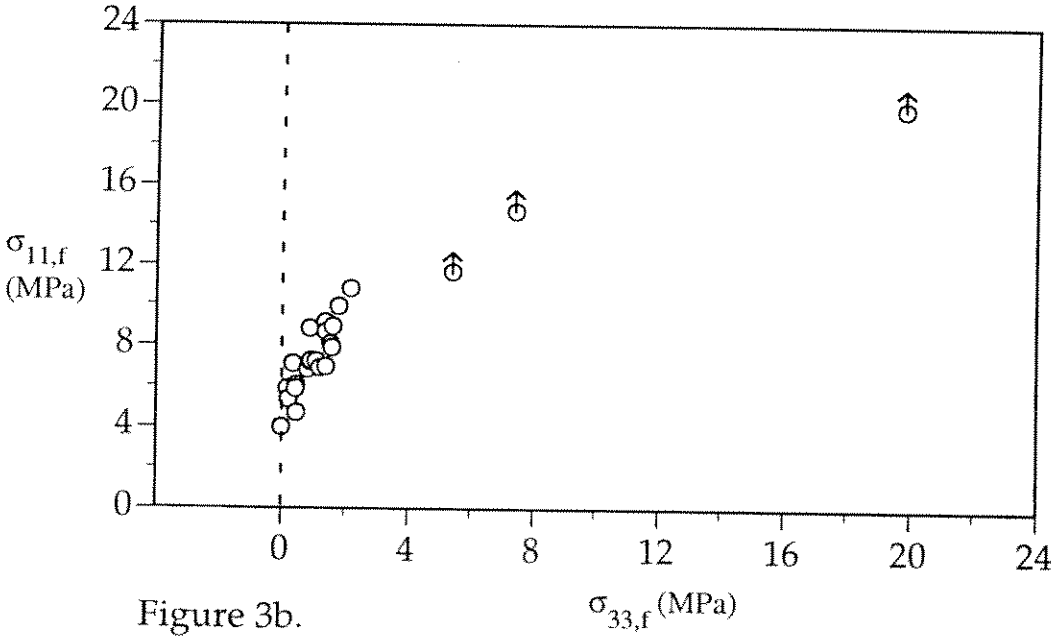

Figure 3b.

Figure 3. The effect of edge confinement in the brittle regime is shown in 3a for both freshwater and saline ice. The failure stress rises with increasing along-column stresses. Figure 3b shows similar (preliminary) results for saline ice in the ductile regime. The arrows indicate the test was terminated before a peak was reached.

The Deformation of Cubes of Frozen Soil Under Triaxial Compression

by

E.T. Gratz and E.M. Schulson
Thayer School of Engineering
Dartmouth College
Hanover, N.H., 03755

Thirty-six triaxial compression tests were performed at the Ice Research Laboratory, Thayer School of Engineering on cubes of frozen soil. The material was cut from cores taken from the Yukon Range at Fort Wainwright, Alaska. The tests were conducted using a true triaxial testing system which applied confining loads proportional to a master load: the master direction corresponded to a horizontal direction in the parent core. The tests were performed by straining the soil a fixed amount (usually between ε_{11}=0.03 to 0.04) and then by unloading. Variables included strain rate (0.001 s^{-1} to 0.07 s^{-1}), temperature (-10 °C, -5 °C, -1 °C), and confining ratio (zero to unity).

Figure 1 shows representative stress-time, strain-time and stress-strain curves for one of the tests. Under all test conditions, ductile behavior was observed. Figure 2 shows the stress-time curves for the samples tested at -10 °C and $\dot{\varepsilon}_{11}$ =0.001 s^{-1}. Yield points in Figure 2 are indicated with squares and the stresses at the start of unloading are indicated with circles. Strain hardening was observed for all tests except for those conducted under uniaxial and near-hydrostatic loading. Figure 3 plots the yield strength and the flow stress at 0.025 strain versus the confining stress for the tests conducted at -10 °C. The yield strength for all of the tests varied from 1.5 MPa to 45 MPa and increased with decreasing temperature, increasing strain rate and increasing confinement. Figure 4 shows the variation of yield strength with temperature. The strength of frozen soil decreased by approximately a factor of three with increase in temperature from -10 °C to -1 °C. Figure 5 plots the yield strength versus the strain rate showing that strength increased with rate and with increasing confinement ratio. The average strain-rate sensitivity was 0.26 as calculated using the slopes of the dashed lines plotted in Figure 5. Reductions in volume of up to 8% were measured just before unloading, followed by volumetric growth (in some cases back to the initial volume) upon post-test storage at -10 °C.

The strength of frozen soil appears to be affected by the presence of ice within some of the larger pores. Both frozen soil and ice share similar thermal and rate

sensitivities [Carter, 1971; Weertman, 1983]. Even the uniaxial strengths are similar at similar temperatures and strain rates [Carter, 1971; Jones, 1982; Schulson, 1990; Smith and Schulson, 1993]. Furthermore, when account is taken of pressure melting of the ice phase, the frozen soil appears to exhibit von Mises flow behavior.

References

Carter, D. (1971). Lois et mecanismes de l'apparente fracture fragile de la glace de rivere et de lac. Ph.D. Thesis, Universite Laval.

Weertman, J. (1983). Creep deformation of ice, Ann. Rev. Earth Planet. Soc., 11, 215-240.

Jones, S.J. (1982). The confined compressive strength of polycrystalline ice. Journal of Glaciology, 28 (98), 171-177.

Schulson, E.M. (1990). The brittle compressive fracture of ice. Acta metall., 43(10), 1963-1976.

Smith, T.R. and Schulson, E.M. (1993). The brittle compressive failure of fresh-water columnar ice under biaxial loading, Acta metall., 41(1), 153-163.

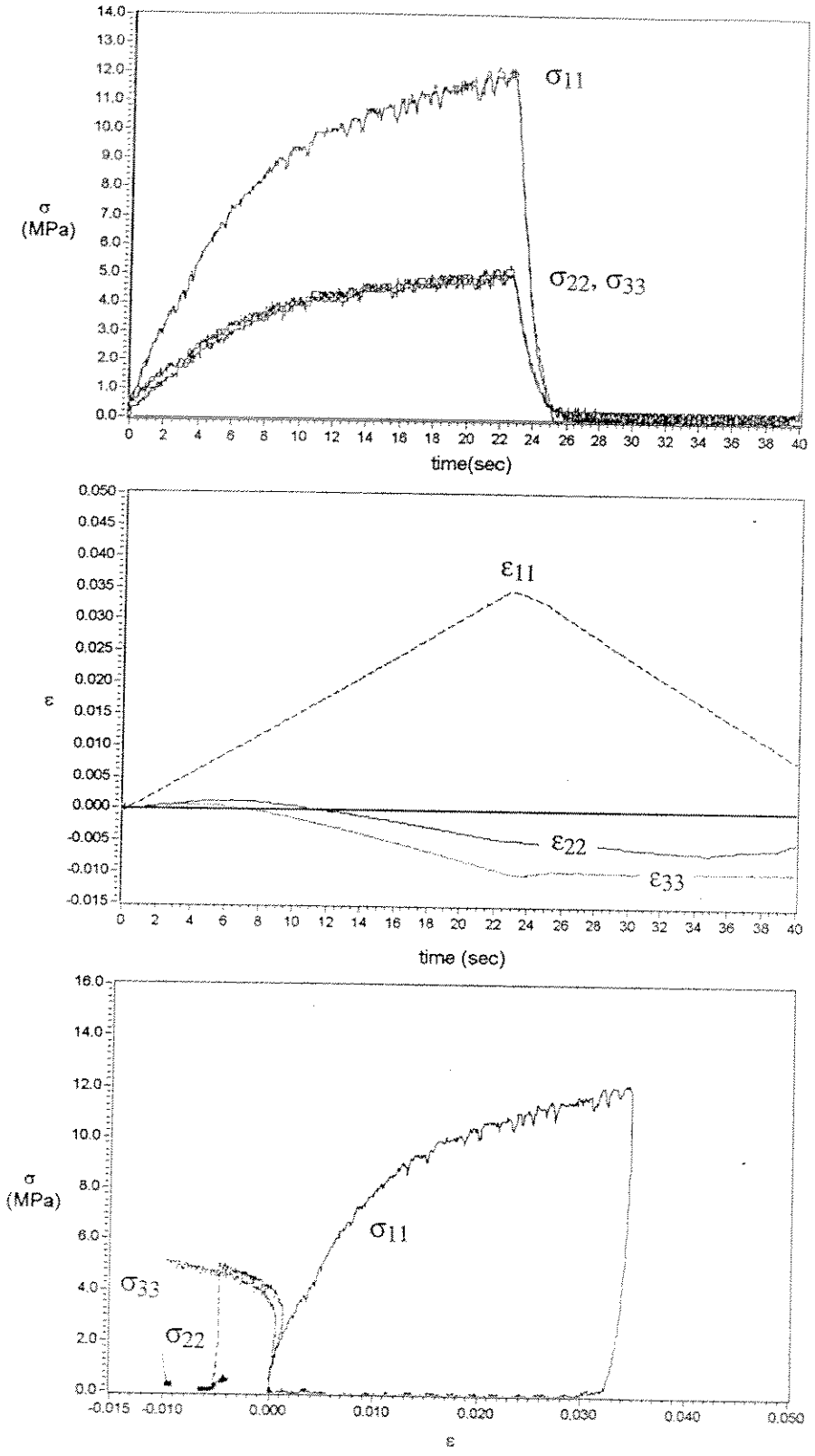

Figure 1: Results for one test where the loading path was $\sigma_{11}:\sigma_{22}:\sigma_{33}=1:0.42:0.42$ at -10 ^{o}C and $\dot{\varepsilon}_{11}= 0.001\ s^{-1}$.

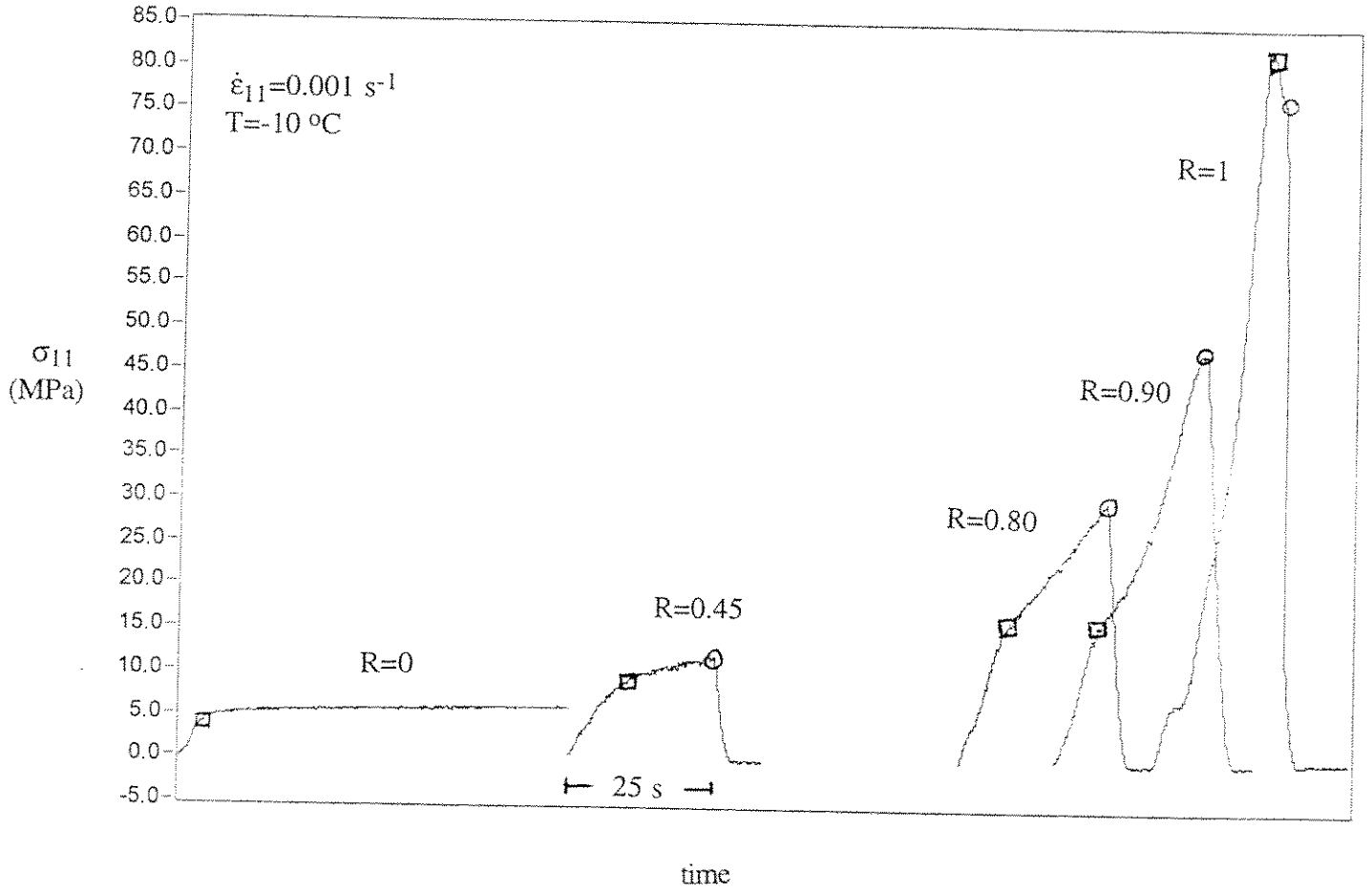

Figure 2: Stress-time curves for the samples tested at -10 °C and $\dot{\varepsilon}_{11}$= 0.001 s^{-1}.

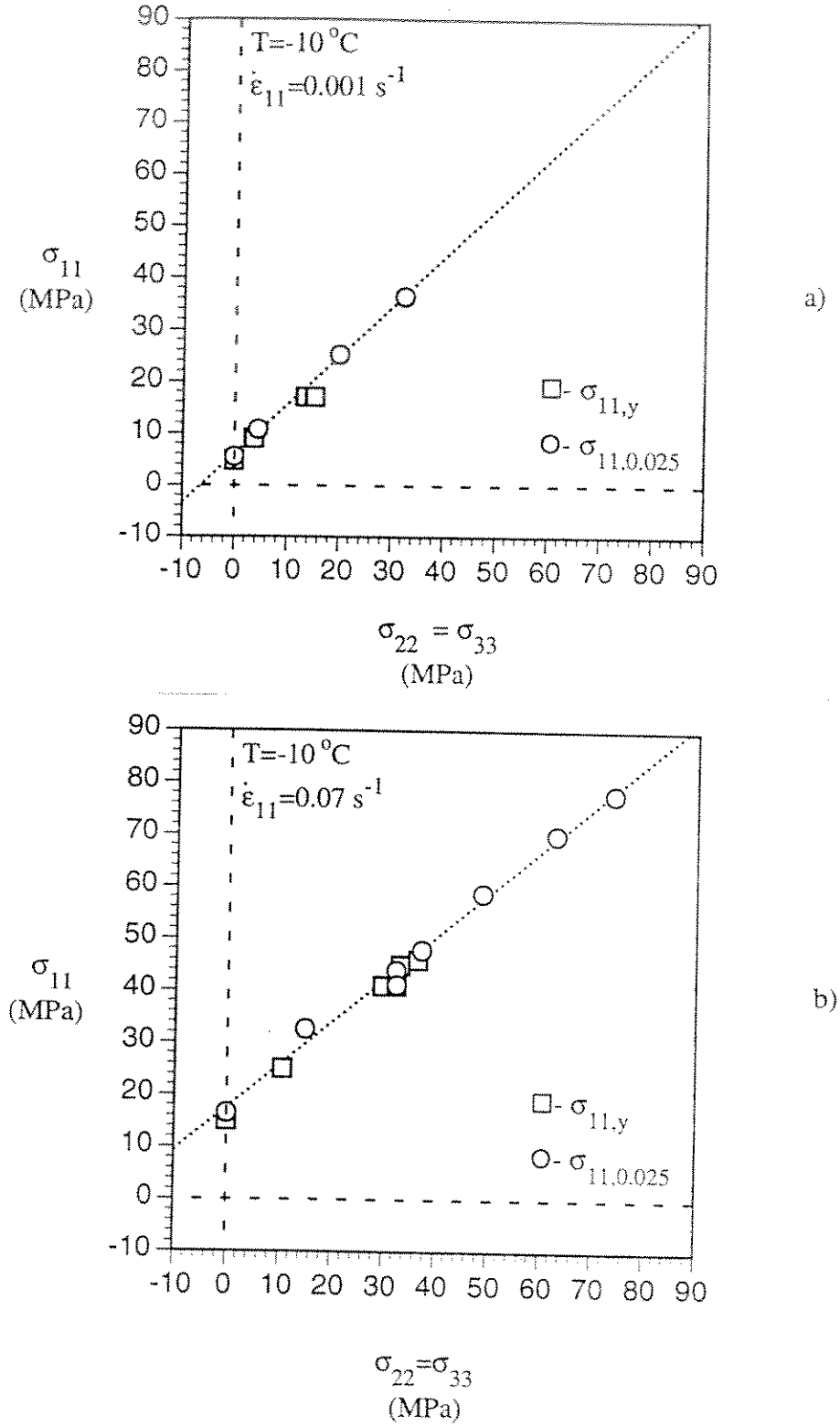

Figure 3: Yield strength and flow stress at 0.025 strain versus confining stress for tests at -10 °C and strain rates of a) 0.001 s^{-1} and b) 0.07 s^{-1}.

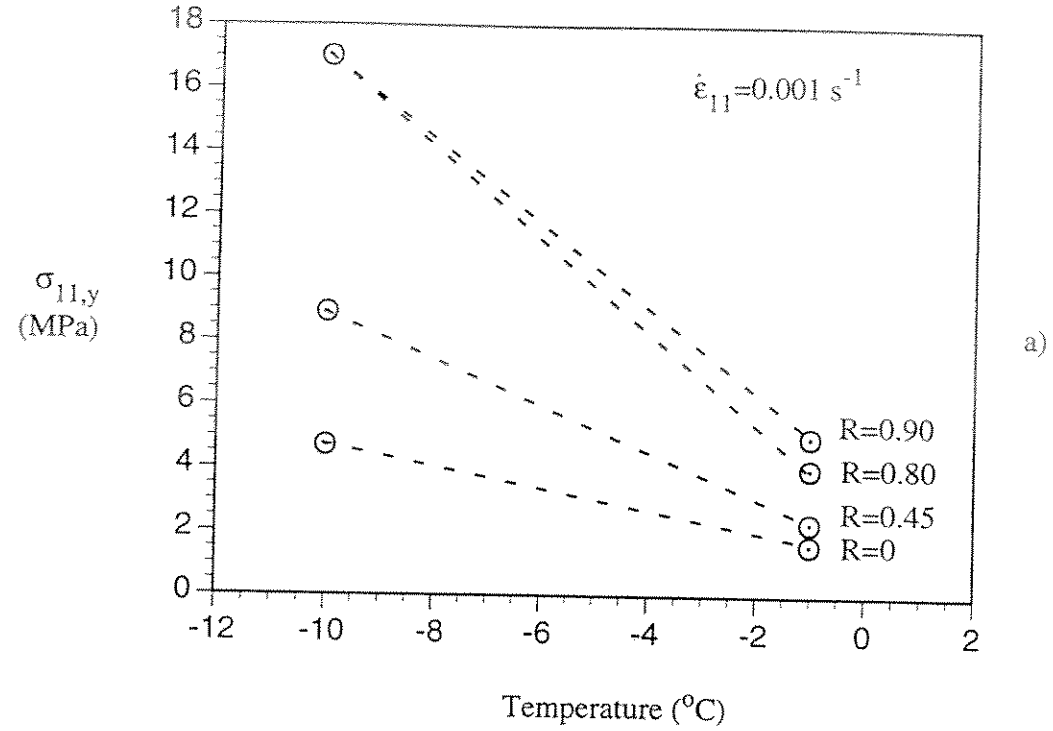

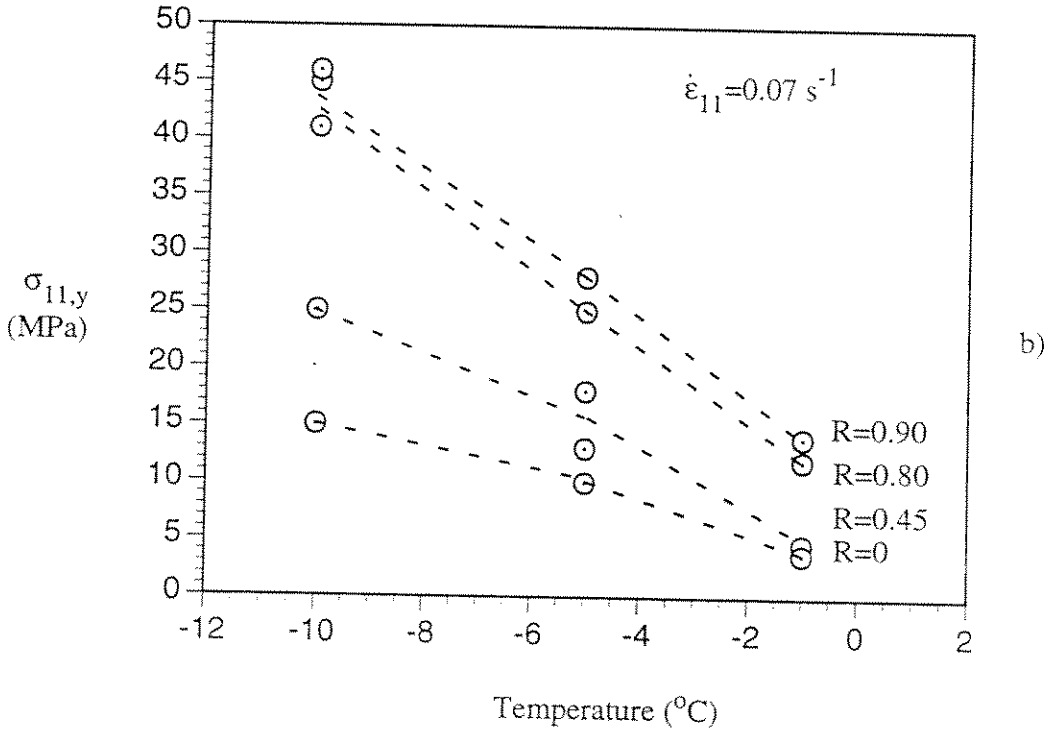

Figure 4: Yield strength versus temperature at a) $\dot{\varepsilon}_{11}$= 0.001 s^{-1} and b) $\dot{\varepsilon}_{11}$= 0.07 s^{-1}.

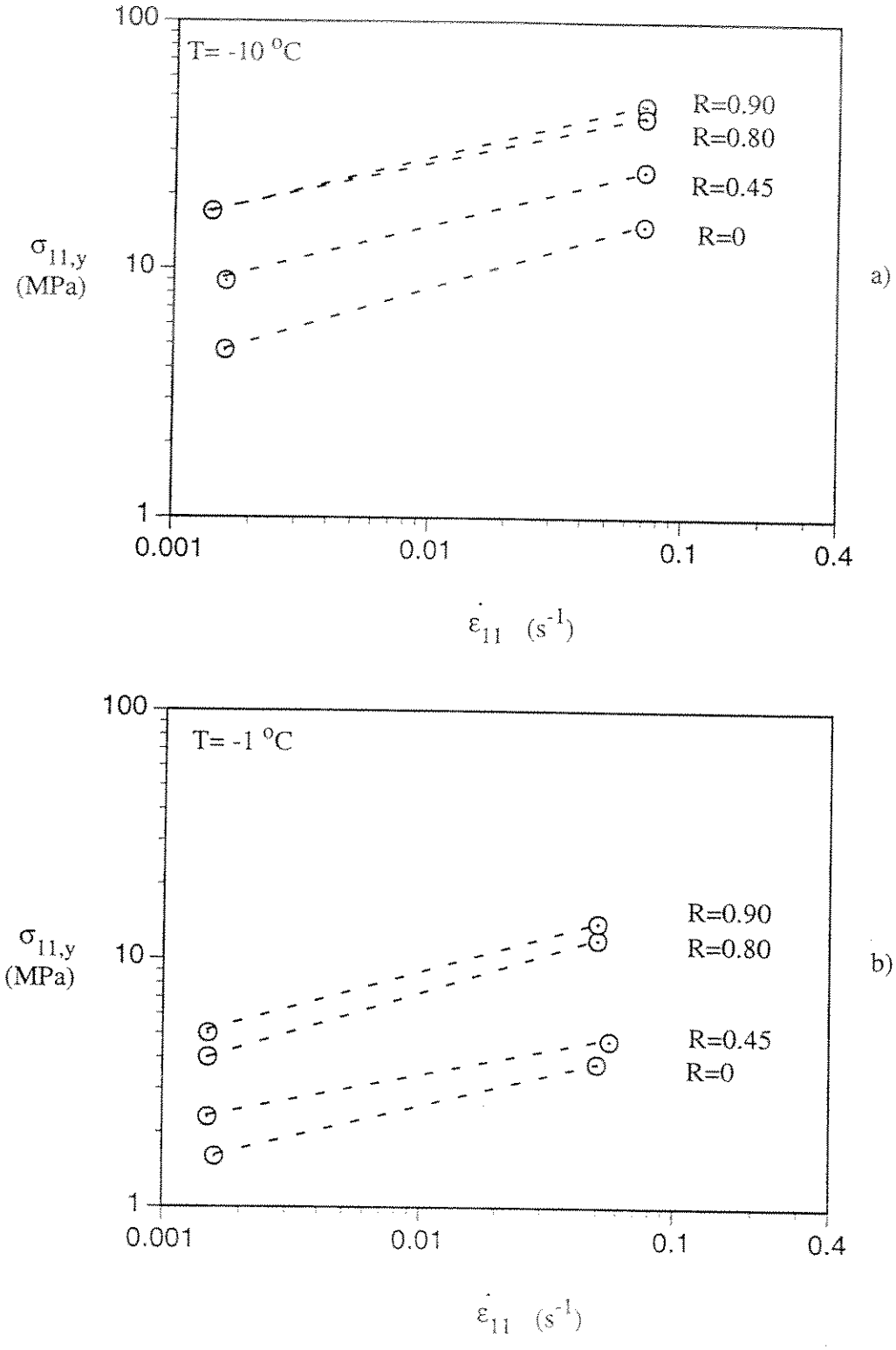

Figure 5: Yield strength versus strain rate at a) -10 °C and b) -1 °C.

INERTIAL OSCILLATIONS IN AN INTERACTING ICE FIELD

W. D. Hibler, III[+] and Petra Heil[*]

Due to frequent and intense storm systems moving across the Antarctic sea ice, ice drift and deformation fluctuate substantially. Observations of drifting buoys show inertial power to be a substantial component of ice deformation. Because the inertial period at high latitudes is close to tidal periods, tidal effects can be also be amplified by this inertial resonance. In practice, the energy dissipation by ice interaction plays a significant role in damping out this inertial energy.

In present sea ice dynamics models both with and without ice interaction, this inertial motion is overdamped due to the underestimation of coupling to the oceanic boundary layer. To develop a more consistent treatment of ice drift under fluctuating wind fields we consider here a vertically integrated formulation of the ice/ocean boundary layer system that incorporates a more realistic treatment of the upper ocean. An example of the results of this imbedding for smoothly varying wind forcing in the absence of ice interaction is shown in Figure 1. Under steady wind conditions this model reduces to the normal nonlinear water drag formulation used in most sea ice dynamics models.

Simulations using this "imbedded" model are carried out for a two week period in the sea ice region near 140 E, 65 S, during which time detailed deformation from an array of seven GPS drifting buoys was available. The results are analyzed to elucidate the role of ice interaction in the Antarctic ice pack in modifying the high frequency motion and determining the role of inertial motion on ice thickness characteristics. Because the coupling of the ice interaction with the inertial oscillations can create propagating wave effects, a high resolution Lagrangian grid model with symmetry along the ice margin was utilized in the initial analysis.

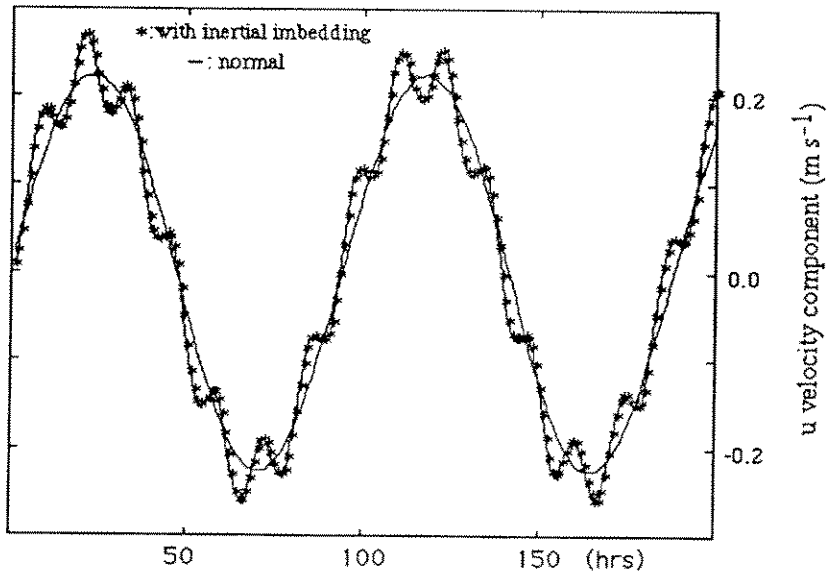

Figure 1: Velocity component of sea ice under smoothly varying wind forcing with and without inertial imbedding.

[+]Thayer School of Engineering, Dartmouth College, Hanover, NH 03755
[*]Co-operative Research Institute, University of Tasmania, Hobart, Australia

EFFECT OF ELECTRIC FIELDS ON ADHESION OF ICE TO METALS

Victor F. Petrenko

Thayer School of Engineering, Dartmouth College, Hanover, NH 03755

If electrostatic interactions contribute to ice adhesions, then the adhesion strength may be changed by an external DC bias applied across an ice/metal interface. Nevertheless, a search for this effect is not easy for two main reasons. First, the phenomenon may happen to be small and masked by data scattering when conventional mechanical tests are used to measure the adhesion strength. Second, the necessary magnitude and even polarity of the DC bias can rarely be predicted due to the complexity of screening mechanism in the subsurface layers of ice (four types of charge carriers, two types of force). So far, such screening has been calculated only in a linear approximation for a very small bias, $V_b \leq kT/e \approx 20$ mV (Petrenko and Ryzhkin, 1984). In search of the effect of DC bias on ice adhesion, we overcame the first obstacle by using a liquid/solid interface instead of a solid/solid one. Indeed, the interfacial energy which determines the adhesion can be easily and reliably measured in a contact-angle experiment when one material is a liquid and the other a solid, as in the water/metal case.

A similar technique can be employed for an ice/metal interface if the metal is in the liquid phase! Mercury, with its melting point at –38.83°C, low chemical activity, and ease in preparing a clean surface, is perfectly suited for such experiments. To measure the surface tension of an ice/mercury interface we employed a manometer made of ice, depicted schematically in Figure 1.

In equilibrium the position of mercury, h, in the capillary is:

$$h \cong 2\cdot(W_{i/a} - W_{i/Hg})/gr\rho \qquad (1)$$

where g is gravity acceleration, r is the capillary radius, ρ is the density of mercury, $W_{i/a}$ is the surface energy of the ice/air interface, and $W_{i/Hg}$ is the surface energy of the ice/Hg interface. When h is measured, eqn. (1) can be used to calculate $W_{i/Hg}$, and hence the adhesion of ice to the liquid metal. A low DC bias was applied across a stainless steel mesh electrode and the mercury. The capillary's radius, r, was 0.25 or 0.5 mm.

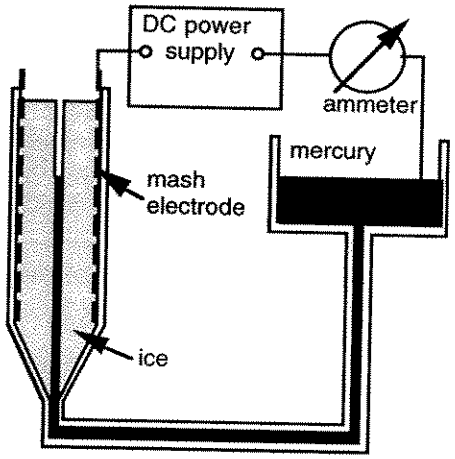

Figure 1. Ice manometer used in measurements of ice/mercury interfacial energy.

We used polycrystalline ices grown from: 1) very pure deionized water; 2) distilled water; 3) untreated tap water; or 4) deionized water doped with small concentrations of NaCl or KOH or HF. The experiments were performed inside a cold room in the temperature range –20°C to –5°C. On the doped ices we found that DC bias had a strong effect on the ice/mercury interfacial energy. The magnitude and sign of the energy change $\Delta(W_{i/a} - W_{i/Hg})$ depends on the bias polarity and magnitude and on the type and concentration of dopant. Figure 2 shows $\Delta(W_{i/a} - W_{i/Hg})$ versus bias V, measured at T = –10°C for ice doped with 0.5% NaCl. As can be seen in Figure 2, the bias can reduce or enhance adhesion of ice to mercury. The effect becomes very pronounced for NaCl concentrations above 0.05%.

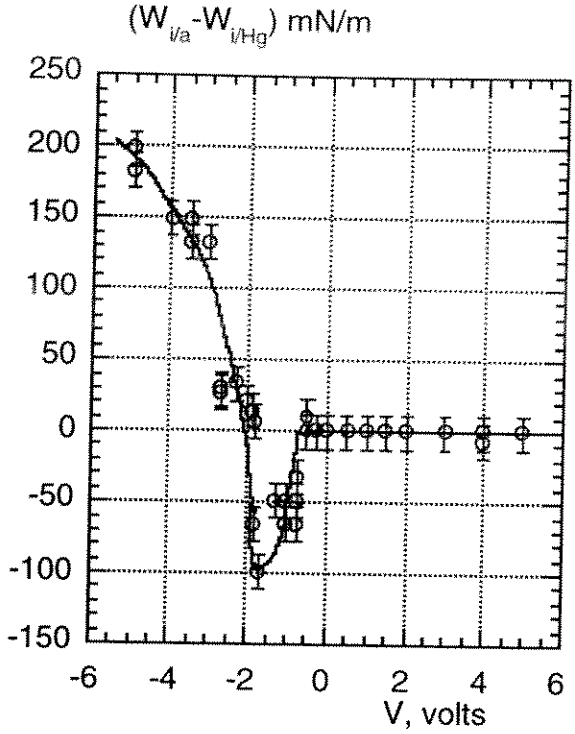

Figure 2. Effect of DC bias on the ice/Hg interfacial energy. Ice doped with 0.5% NaCl, T = –10°C.

At lower concentrations of NaCl or with ice grown from tap water the effect is small, poorly reproducible, and characterized by a long "waiting" time or delay (minutes), while in ice doped with 0.5% NaCl the mercury begins to move immediately after the bias is applied. The effect was completely reversible; i.e., $W_{i/Hg}$ was restored after the bias was shut off. The phenomenon is very reproducible and easy to observe. The maximum change in h was 12 mm for r = 0.25 mm.

Measurements of current-voltage characteristics showed that it was the voltage, not the current, that caused the changes. Typically current was measured in tens of μA and the estimated rate of the temperature change was less than 10^{-6} °C/s. In ice doped with KOH or HF, the application of a DC bias caused an almost symmetrical decrease in $W_{i/Hg}$ which was comparable in magnitude with that found on NaCl-doped ice. Application of AC voltage up to 40 V in amplitude and in the frequency range 10 Hz to 10 kHz didn't produce any noticeable changes in $W_{i/Hg}$. In pure deionized or distilled water, the application of a DC bias up to 40 V did not produce noticeable changes in $W_{i/Hg}$ either. As was shown earlier (Petrenko, 1994), it takes 1 kV to 3 kV to change the adhesion of very pure ice to a metal. We attributed the different reactions of pure and doped ice to a DC bias to their differences in screening length and electric relaxation time.

The described phenomenon is very new and will require intensive and rigorous investigation before it can be fully interpreted. However, what this phenomenon confirms is the essential role played by electrical double layers on ice/metal interfaces in ice adhesion. Although the absolute magnitude of $W_{i/Hg}$ can differ in the case of solid mercury, the electrostatic interactions are essentially the same in both cases (for liquid Hg and solid Hg). Now that we have found ranges of DC voltage and dopant concentrations for which the effect was observed, we are planning to carry out experiments on the effect of DC bias on adhesion strength of ice to solid metals.

How the electrical interactions work

Figure 3 illustrates how molecular polarization P and space charge density ρ vary with distance in the vicinity of an ice/metal interface. An electrical charge induced in a metal is equal in magnitude and opposite in sign to the charge in ice. An electrical charge similar to the one shown in Figure 3d, but with lesser magnitude, is also induced in any dielectric material brought in contact with ice.

The "reflection coefficient" of electrical charges in dielectrics is:

$$r = \frac{\varepsilon - 1}{\varepsilon + 1} \qquad (2)$$

where ε is the relative dielectric permittivity of a solid material. Since for most solids $\varepsilon \geq 3$, the induced electric charge is close to or comparable with the one induced in metals.

In our opinion, an interaction between the ice surface charge and the charge induced in a solid may strongly affect the strength of an ice/solid interface. To justify this assumption, we can first estimate that interaction in the following way. The electrostatic attraction (negative pressure P_{el}) of two plane surface charges:

$$P_{el} = \frac{\varepsilon_0 \varepsilon E^2}{2} \qquad (3)$$

where ε_0 is the dielectric permittivity of the vacuum, and E is the electric field strength in the space between the charges. Since the charge distribution shown in Figure 3d determines the contact potential V_c of the two materials, we can estimate E as V_c/L, where L is the distance between the plane charges located in the ice and in the solid. V_c for ice/metal interfaces varies from a few tenths of a volt to about 1 V (Buser and Jaccard, 1978). Taking L ≈ 1 nm (the main screening length in our doped ice), ε = 3.2 (the high-frequency dielectric constant of ice) and V_c = 0.5 V (the typical magnitude of a contact potential), we find from eqn. (3) that $P_{el} \approx$ 3.3 MPa and that this magnitude is comparable with, but exceeds, the macroscopic tensile strength of ice, 1.5 MPa (see Schulson et al., 1984). Much more sophisticated calculations of the energy of the electrostatic interaction between the ice surface charge and a metal (Ryzhkin and Petrenko, 1997) showed that at −10°C this energy is 0.01 to 0.5 J/m^2. Real space-charge distribution and charge relaxation were used in those calculations. The lower limit corresponds to pure ice while the upper one corresponds to heavy doping. Compare these values with the experimental (0.08 ± 0.012) J/m^2 determined with SFM (Petrenko, 1997).

One more evidence of the role that electrostatic interactions play imortant role in ice adhesion came from experimental result by Petrenko (1994) who found that an application of relatively weak electric fields E ≈ 10^3 V/cm (weak in comparison with $V_c/L \approx 10^7$ V/cm) increases the ice/steel shear adhesion strength by 20%.

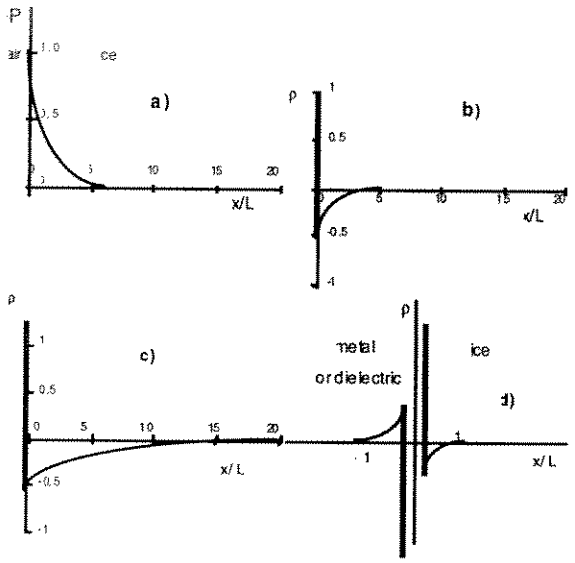

Figure 12. Schematics of spatial distribution of an electrical charge ρ(x) near the ice/air and ice/metal interfaces. L is a shorter screening length. a) Water molecule polarization P near the surface. b) Density of the polarization charge ρ(x) = −dP/dx without screening. c) The same as (b) but with additional screening by minority charge carriers. d) Electrical charge in ice near the surface and its image in the metal.

References

Buser, O. and Jaccard, C. (1978) Charge Separation by Collision of Ice Particles on Metals: Electronic Surface States. *Journal of Glaciology,* 21(85): 547-57.

Petrenko, V. F. (1994) The effect of static electric fields on friction of ice. *J. Applied Physics,* 76(2) : 1216-19.

Petrenko, V. F. (1997) Study of ice surface, ice/solid and ice/liquid interfaces with SPM. *J. Phys. Chem.* In press.

Petrenko, V.F. and Ryzhkin, I.A. (1984) Dielectric Properties of Ice in the Presence of Space

Ryzhkin, I. A. and Petrenko, V. F. (1997) Physical mechanisms responsible for ice adhesion. J. Phys. Chem. in press.

Schulson, E. M., P. N. Lim and R. W. Lee (1984) A brittle to ductile transition in ice under tention *Phil. Mag.*, 49, 353-63.

ACKNOWLEDGMENTS: This work was supported by the ARO.

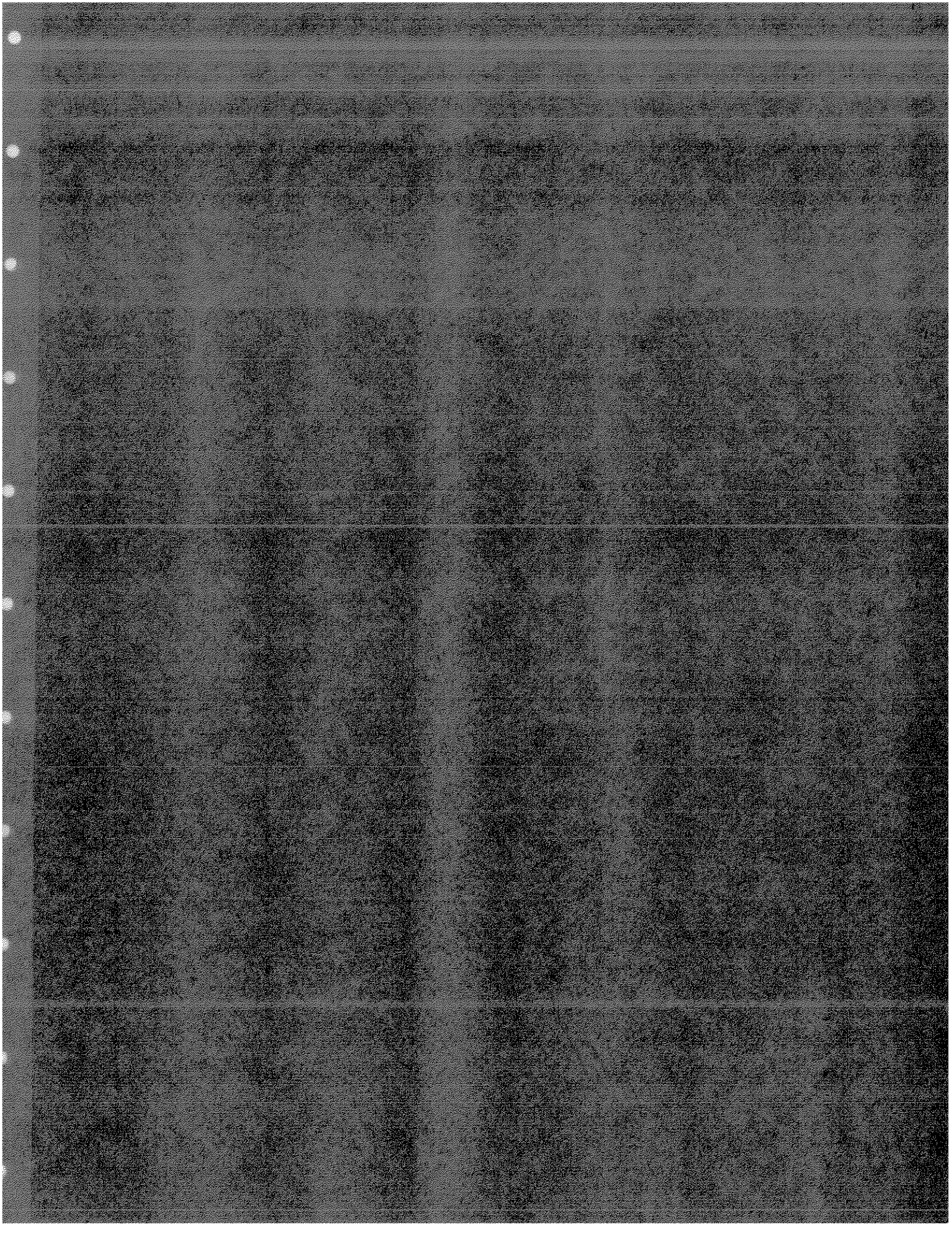

PHYSICAL MECHANISMS RESPONSIBLE FOR ICE ADHESION

Victor F. Petrenko and Ivan Ryzhkin

Thayer School of Engineering, Dartmouth College
Hanover, NH 03755

We studied an electrostatic model of ice adhesion based on the existence of the surface states of protonic charge carriers on the surface of ice. At distances greater than one intermolecular distances the model gives an order of magnitude for the adhesive energy which is significantly greater than both chemical bonding energy and van der Waals forces. It also provides an understanding of the time- and temperature-dependent phenomena that explain the difference between adhesive properties of ice and water.

All possible mechanisms of ice adhesion can be classified into one of three groups: a covalent or chemical bonding mechanism, a dispersion of or fluctuation in electromagnetic interaction (van der Waals forces), or a direct electrostatic interaction (1).

The first mechanism corresponds to the chemical reactions and the formation of interfacial compounds. In covalent or chemical bonding the adhesive energy results from lowering of the quantum-mechanical energy of the system due to overlap of the wave functions of the interacting solids. Such an interaction is essential only at a distance on the order of 0.1–0.2 nm. In addition, this type of adhesion is very sensitive to the chemical nature of adhesive solids. In a perfect contact, the chemical bonding mechanism can provide adhesive energy of ≥ 0.5 J/m^2. The latter value has been obtained from the definition of chemosorption (bonding energy higher than 0.5 eV per molecule (2)), so it can be considered the lowest value of adhesion energy for the chemical bonding mechanism.

In contrast to chemical bonding, van der Waals forces are long-range and act between all substances. These forces are defined only by the macroscopic characteristics of a solid (dielectric function at different frequencies), and for this reason they are rather insensitive to experimental conditions (3, 4). This circumstance, together with the availability of an advanced theory of dispersion forces formulated by Dzyaloshinskii et al. (5), accounts for the ubiquity of this mechanism. In the case of ice this mechanism has been studied by Elbaum and Schick (6) and by Wilen et al. (7).

In addition to chemical bonding and dispersion forces, two solids that contain noncompensated or spatially separated charges will also generate electrostatic forces. Historically this is probably the oldest mechanism recognized; it has been known for more than 2,000 years. Its importance has been rediscovered by Stoneham and Tasker (8) rather recently. A detailed review of the role of electrostatic in adhesion has also been given by Hays (9). To the best of our knowledge, there have been no studies of the electrostatic contribution to ice adhesion. In this paper we describe a simple model that is based on a theory of the electrical properties of the surface of ice (Petrenko and Ryzhkin (10)). The model reveals a connection between the ice adhesion problem and other properties of ice. We compare our model with van der Waals forces, the chemical bonding mechanism, and with experimental results.

The main conclusion is that the electrostatic interaction plays a significant, if not major, role in ice adhesion. The key point of our model is the ordering of water molecules adjacent to the ice/solid interface or, in other words, the appearance of the surface states for protonic charge carriers. So the problem is reduced to the study of water molecule behavior at the solid surface, which can be done by computer simulation. However, in the following sections we will simply assume that there exist surface states that can be occupied by protonic point defects. The occupancy of these surface states is defined by the interplay between the coulomb energy of captured charge carriers and the energy depth of the surface states. Then, either the occupancy coefficient of a surface state (in the nonequilibrium case) or the energy depth of the surface state will be taken as a parameter.

Finally, we shall study the effect of surface charge density on the energy of the interaction between ice and a metal plate. This electrostatic mechanism will be compared with others and ways to improve our model in future studies will be discussed.

Model and basic results for electrostatic mechanism

Ice consists of polar water molecules that strongly interact with any solid substrate which has dielectric permittivity different from that of ice. In addition, there is a great deal of theoretical and experimental evidence for the existence of a surface charge in ice (10, 11). This surface charge can also interact with the substrate. Here we assume that the surface charge originates from the capture of protonic charge carriers by the ice surface. The captured defects are presumably D defects, H_3O^+ ions, or protons. Actually, positive ions are smaller in size than negative ones, because they have fewer electrons or do not have them at all and exist as protons. Thus we can use the image charge theory for smaller distances, where the potential energy of the charge and its image may be less than the charge energy within the ice. For negative ions of larger size it is much more difficult to reach this. At thermal equilibrium the occupancy of surface states cannot be perfect, because the gain in energy due to captured charge carriers is compensated for by the rise in electrostatic energy. However, the electrostatic energy itself can be reduced significantly by charge redistribution inside the substrate (by induced charges). This could lead to perfect occupancy of the surface states and rather high adhesion energy (close to the electrostatic energy).

The spatial distribution of charge carriers in the subsurface layer of ice has been calculated by us previously. Thus, we will use some results from that paper (10). The first integral of Poisson's equation can be written in the following form:

$$E = \frac{\sigma_0}{\varepsilon\varepsilon_0} f(V) \tag{1}$$

Where E and V are the electric field strength and electrostatic potential, respectively (both are functions of the space coordinate z); $\sigma_0 = e_B \cdot \lambda \cdot N$; e_B is the effective charge of Bjerrum defects; N is the concentration of water molecules; λ is the screening length given by $\sqrt{\varepsilon\varepsilon_0 kT / e_B^2 N}$; ε and ε_0 are the dielectric permittivities of ice (≈ 3.2) and a vacuum, and k and T are the Boltzmann's constant and the temperature respectively. The function f(V) is defined by the following equations:

$$f(V) = \sqrt{\ln(a(V) \cdot a(-V) \cdot b^2(V) \cdot b^2(-V))} \tag{2}$$

$$a(V) = \frac{\exp(E_i / 2kT) + (4/3)\exp(e_i V / kT)}{\exp(E_i / 2kT) + 4/3} \tag{3}$$

$$b(V) = \frac{\exp(E_B / 2kT) + \exp(e_B V / kT)}{\exp(E_B / 2kT) + 1} \tag{4}$$

Here we used Bjerrum defects as charge carriers being captured in the surface states. Equation (1) holds at any point of the ice crystal. Applying it to the ice surface, we get the relationship between the surface charge density σ_s and the surface potential V_s: $\sigma_s = \sigma_0 f(V_s)$.

It is now easy, using equations (1) through (4), to calculate the electrostatic contribution to the adhesion energy of ice. First, let us calculate the electrostatic energy of the screening layer of ice as a function of the surface potential. This energy is very important, because it gives the upper limit for the adhesion energy. Using the definition of electrostatic energy and equation (1) we get:

$$W(V_s) = \int_0^{\infty} \frac{\varepsilon\varepsilon_0}{2} E^2 dx = -\frac{\sigma_0}{2} \int_0^{\infty} f(V) \cdot \frac{dV}{dx} dx = \frac{\sigma_0}{2} \cdot \int_0^{V} f(V) dV \qquad (5)$$

The graph of W_e vs. V_s is pictured in Fig. 1. Perfect occupancy by Bjerrum D defects, positive ionic defects H_3O^+, or protons gives the values of the surface potential $V_s \approx 1.47$ V, 2.50 V, and 5.13 V respectively. According to Fig. 1, complete occupancy of the surface states by Bjerrum defects, H_3O^+ ions, and protons would correspond to an upper limit of adhesion energy of 0.8 J/m^2, 0.32 J/m^2, and 1.35 J/m^2 respectively. The smaller values are for imperfect occupancy. Using the relationship between the surface charge density and surface potential it is easy to recalculate this energy vs. surface charge density.

Now let us consider a metallic plate at a distance d from an ice surface. The non-uniform charge distribution in the ice will induce a surface charge on the metal and, therefore, an electric field between the ice and the metal plate. The total electrostatic energy of the system per unit area can be written in the following form:

$$W_e(d,V) = \frac{\sigma_0^2 \cdot d}{2\varepsilon\varepsilon_0} \cdot \left[f(V) - \frac{\sigma}{\sigma_0} \right]^2 + \frac{\sigma_0}{2} \int_0^{V} f(V') dV' \qquad (6)$$

However, V in equation (6) is the surface potential of ice, which has to be found from minimization of the energy for each value of distance d. Note that at this time we consider surface charge density to be a constant. Physically, that could correspond to a non-equilibrium occupancy of the surface states. Performing a minimization procedure for W_e (d,V),we arrive at the adhesion energy per unit area as a function of d:

$$W_a(d) = W_{min}(d) - W_{min}(\infty) \qquad (7)$$

This function is pictured in Fig. 2 for the same cases of perfect occupancy by the Bjerrum D defects, positive ionic defects H_3O^+, and protons, shown as curves 1, 2, and 3 respectively.

Under equilibrium conditions the surface charge density of ice, σ, increases with a decrease in the distance, d, because of screening of the ice surface charge by an induced charge on the metal plate. Indeed, in this case the coulomb energy of captured charge carriers decreases, so higher occupancy becomes possible. In considering this case one first has to sum up the electrostatic energy, the energy gain due to occupancy of the surface states, and the entropy contribution of the surface defects:

$$F = \frac{d\sigma_0^2}{2\varepsilon\varepsilon_0} \cdot \left[f(V) - \frac{\sigma}{\sigma_0} \right]^2 + \frac{\sigma_0}{2} \cdot \int_0^{V} f(V') dV' - \frac{\sigma}{e} \cdot E_0 + \frac{kT}{e} \left[\sigma \cdot \ln\left(\frac{\sigma}{\sigma_m}\right) + (\sigma_m - \sigma) \cdot \ln\left(1 - \frac{\sigma}{\sigma_m}\right) \right] \qquad (8)$$

Here E_0 is the energy of surface states (assuming $E_0 = -0.5$ eV), $\sigma_m = e/S$, and S is the surface area of one water molecule. Then the free energy F has to be minimized over V and σ. This procedure also assumes that the chemical potential of the ice bulk is kept constant and equals zero. Doing so for every value of d, we arrive at the equilibrium free energy as a function of the distance or equilibrium adhesion energy. This is pictured in Fig. 2 (curve 4, for protons).

A similar procedure enables us to find the equilibrium occupancy of the surface state or the surface potential of ice as a function of the energy of surface states E_0 or temperature. Let us assume that the metallic plate is infinitely far from the ice surface. Then, to minimize the first positive element in equation (8), we have to assume $\sigma = \sigma_0 f(V)$. Then F becomes a function of only one parameter, either V or σ. It is somewhat easier to perform the final minimization over V, but the results can be recalculated as a function of σ as well. The occupancy coefficient of the

surface states with D defects plotted versus surface state energy is shown in Fig. 3. The surface state energy level is measured with respect to the chemical potential of D defects in the bulk.

Discussion

As can be seen from our results, typical values of the adhesion energy are located between 1.3 J/m^2 and 0.08 J/m^2, depending on the type of charge carriers and the energy of their surface states. This magnitude is comparable to or even higher than the experimentally measured surface energy of ice (about 0.1 J/m^2). In fact, it is as high as values for the chemical bonding mechanism. However, in contrast to the latter, the electrostatic mechanism remains significant up to a larger distance (about $10 \cdot r_{oo}$; $r_{oo} = 0.276$ nm). Thus, at distances larger than r_{oo}, the electrostatic mechanism is significantly more important than the chemical bonding one. Our calculations also show that at distances greater than r_{oo}, the electrostatic energy exceeds that of the van der Waals forces, if the Hamaker constant equals $3 \cdot 10^{-20}$ J (1). Note that the last estimation concerns an ice/ice (or water/water) interface, but not an ice/metal interface, as do curves 1, 2, 3, and 4 in Fig. 2. The van der Waals interaction between ice and metal has not been considered and this will be the subject of our future research.

We should emphasize the long-range character of the electrostatic mechanism: the adhesive energy equals 0.01 J/m^2 even at $z \approx 90 \cdot r_{oo}$ for the maximum density of a surface charge. Note also that the adhesive energy for a non-equilibrium detaching experiment should be higher than that for an attaching one. The latter can be explained by the almost perfect screening of electrostatic energy by a metallic plate when ice and metal are in contact. It is rather easy to understand the behavior of adhesion energy with distance in equilibrium experiments. At small distances a metallic plate screens the electrostatic energy and we have high adhesive energy, because the occupancy of surface states is high. However, when the distance increases, the electrostatic energy increases as well, and we arrive at the lower occupancy coefficients and a lower surface charge density. Compare curves 3, 2, and 1 in Fig. 2. These are equivalent to the more rapid decay of free energy with distance than in the case of constant occupancy.

We also studied the behavior of the occupancy coefficient (for the model of the surface states for D defects) as a function of the surface state energy, E_s. The occupancy coefficient is close to zero when $E_s \approx 0.1$ eV, Fig.3. One reason for the charge carriers being captured into the surface states with positive energy has to do with the entropy gain in the free energy. For the same reason, defects exist in the ice bulk. Note that for the bulk D defects the "creation energy" equals 0.34 eV per defect, and this energy is significantly greater than 0.1 eV. Eventually this leads to an "occupancy coefficient" for the bulk states on the order of $3 \cdot 10^{-7}$.

We did not consider any time-dependent phenomena associated with ice adhesion; however, we should note here that such phenomena are inherent in our model. In order to enter or leave the surface state, defects have to overcome some electrostatic barrier, and this leads to non-equilibrium situations and time-dependent phenomena.

Conclusions

The electrostatic model of ice adhesion reveals the relationship between the electrical properties of the surface of ice and ice adhesion. The model gives a correct order of magnitude for the adhesive energy. The electrostatic interaction between ice and metals supplies energy which is significantly higher than chemical bonding energy and van der Waals forces at distances greater than intermolecular ones. It also provides an intuitive way to understand the time- and temperature-dependent phenomena that help explain the difference in adhesive properties of ice and water.

ACKNOWLEDGMENTS

This work was supported by the ARO.

References

(1) Israelachvili, J.N. *Intermolecular and Surface Forces*, 2nd ed.; Academic Press: London, 1991; Chapter 2.
(2) Spanjaard, D.; Desjonqueres, M.C. In *Interaction of Atoms and Molecules with Solid Surfaces*, Eds. Bortolani, V.; March, N.H.; Tosi, M.P.; Plenum Press: New York, 1990; Chapter 9.
(3) Mahanty, J.; Ninham, B.W. *Dispersion Forces*; Academic Press: London, 1976; Chapter 9.
(4) Barash, Y.S.; Ginzburg, V.L. In *The Dielectric Function of Condensed Systems*, Eds. Keldysh, L.V.; Kirzhnitz, D.A.; Maradudin, A.A.; Elsiever Science: Amsterdam, 1989; Chapter 9.
(5) Dzyaloshinskii, I.E.; Lifshitz, E.M.; Pitaevskii, L.P. *Adv. Phys.* **1961**, *10*, 165.
(6) Elbaum, M.; Schick, M. *Phys. Rev. Lett.* **1991**, *66*, 1991.
(7) Wilen, L.A.; Wettlaufer, J.S.; Elbaum, M.; Schick, M. *Phys. Rev. B*. **1995**, *52*, 12426.
(8) Stoneham, A.M.; Tasker, P.W. *J. Phys. C: Solid State Physics*. **1985**, *18*, L543.
(9) Hays, D.A. In *Fundamentals of Adhesion*, Ed. Lee, L.H.; Plenum Press: New York, 1991; Chapter 8.
(10) Petrenko, V.F.; Ryzhkin, I.A. *J. Phys. Chem.* **1997**, this issue.
(11) Petrenko, V.F. *The Surface of Ice*, USA CRREL Special Report, 94-22.
(12) Dash, J.G.; Fu, H.Y.; Wetlaufer, J.S. *Rep. Prog. Phys.* **1995**, *58*, 115.

Figure Captions

Fig. 1. Graph illustrating the electrostatic energy of the screening layer of ice per surface unit, W_e, vs. surface potential, V_s ($T = -10°C$).

Fig. 2. Graph illustrating the adhesive energy of the ice/metal interface per surface unit, W_a, as a function of distance, z. Curves 1, 2, and 3 correspond to perfect occupancy by D defects, H_3O^+ ions, and protons respectively (fixed occupancy curves). Curve 4 depicts the equilibrium dependence of adhesion energy on distance for proton surface states ($T = -10°C$).

Fig. 3. Graph illustrating the occupancy coefficient of the surface states for D defects, f, as a function of surface states energy, E_s ($T = -10°C$).

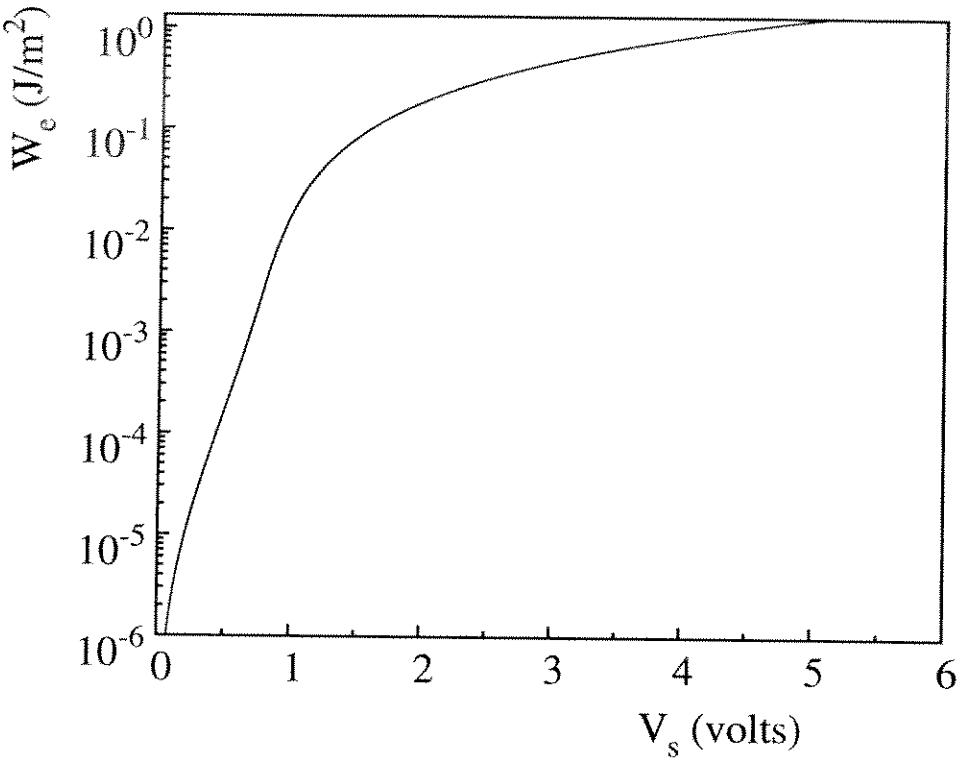

Figure 1

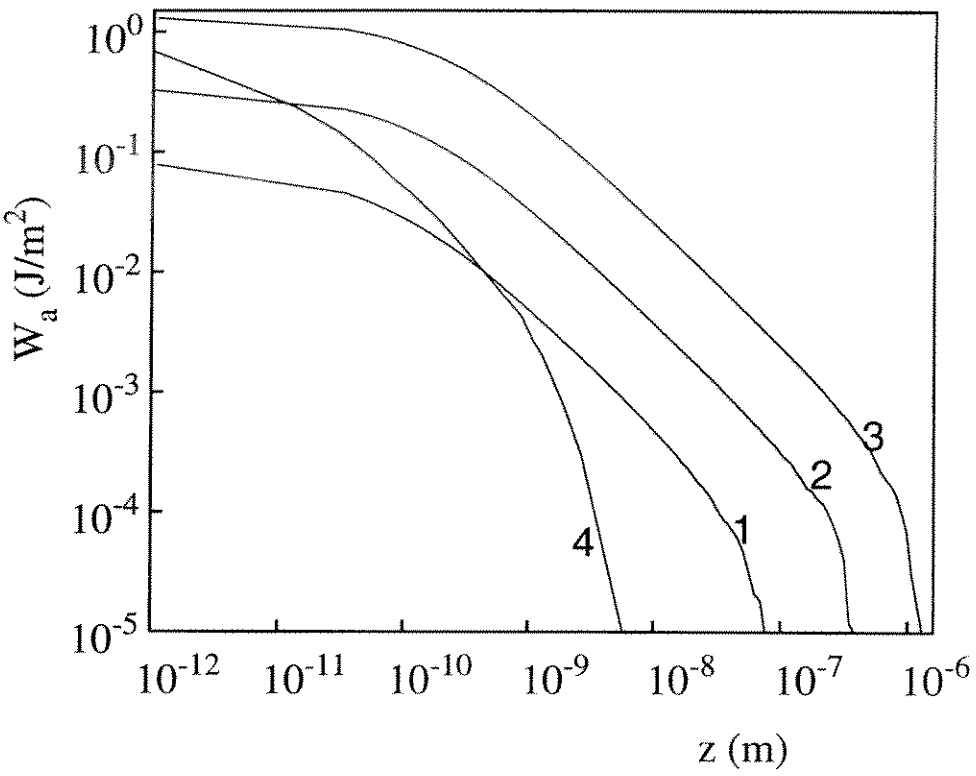
10^{0}
10^{-1}
10^{-2}
10^{-3}
10^{-4}
10^{-5}
W_a (J/m^2)
10^{-12}
10^{-11}
10^{-10}
10^{-9}
10^{-8}
10^{-7}
10^{-6}
z (m)
1
2
3
4

Figure 2

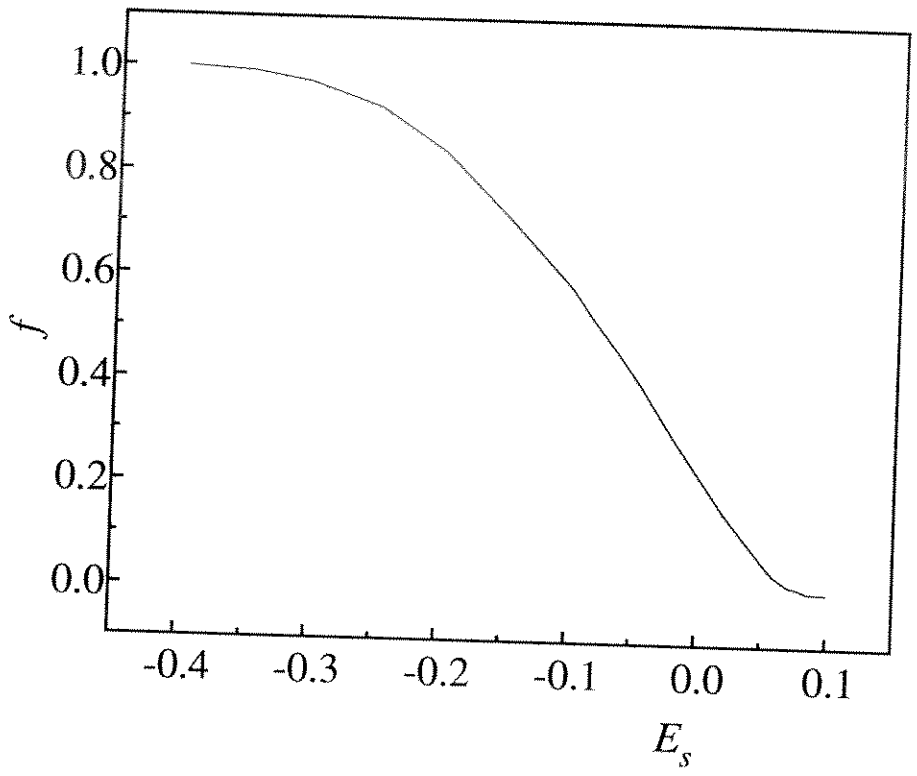

Figure 3

THE EFFECT OF HCL ON THE MECHANICAL BEHAVIOR OF ICE

D. Cullen and I. Baker

Thayer School of Engineering, Dartmouth College, Hanover, NH 03755, USA

Following the work of S. Jones[1], J. Glen[2], R. Whitworth[3] and K. Jia[4], the effect of HCl on the mechanical properties of ice, particularly the dislocation velocity, is being investigated. New testing equipment has been developed to facilitate this research. Growth of suitable low dislocation density single crystal samples has been troublesome and new methods of growth are being explored as well as modifications to the present methods. In addition, experiments that do not require a very low dislocation density (i.e., non-topographic) are being undertaken.

The new testing equipment consists of a computer controlled stress-strain jig based on a stepper motor design and a modified 35 mm camera. The stress-strain jig has been constructed to test ice samples mechanically under either uniaxial tension or compression. The software that governs the stepper motor system can be set to run under load or displacement control, in tension or compression, or to do fatigue testing. The jig is portable and can be transported to the National Synchrotron Light Source at Brookhaven National Laboratories (BNL). A 35 mm camera has been modified to take x-ray photographs using the synchrotron light source. The camera is remotely operated from outside the x-ray safety hutch which permits a series of photographs to be taken in rapid succession. The camera can also be set to take double exposures allowing accurate determination of dislocation movement and, hence, dislocation velocity. The camera has been tested during a research trip this past February and performed without any problems.

---

[1] Jones, S. and Nakamura, T., *Softening Effect of Dissolved Hydrogen Chloride In Ice Crystals*, Scripta Metallurgica, **4**,1970, pp. 123-126

[2] Jones, S. and Glen, J., *The Effect of Dissolved Impurities on The Mechanical Properties of Ice Crystals*, Phil. Mag. **19**, 1969, pp. 13-24

[3] Shearwood, C. and Whitworth, R., *The Velocity of Dislocations in Crystals of HCl-Doped Ice*, Phil. Mag., **65**, 1, 1992, pp. 85-89

[4] Jia, Kunlun, et. al., *Dislocation Mobility in HCl Doped Ice*, Mat. Res. Soc. Proc. Vol. 375, MRS, 1995, pp. 287-292

Unfortunately, the growth of highly-doped, low-dislocation-density, single-crystal ice samples containing HCl has proved to be difficult. The method currently being used was developed by Khusnatdinov and Petrenko[5] and consists of drawing a vacuum through a pair of cold fingers on a container of water. The vacuum deaerates the water and the water vapor freezing to the cold fingers cools the water to form ice. This method seems to work well for pure or lightly doped ice, but the dislocation density for the highly doped ice (5 ppm HCl or greater) is very high in a significant proportion of the samples. A photograph and video of the best samples to date will be shown. In correcting this problem the biggest hurdle has been that the dislocation density could only be determined from a visit to the synchrotron at BNL, which is undertaken but 3 or 4 times a year. Recently the Army's Cold Regions Research Lab has donated a Lang camera to the Thayer Engineering School. This camera, which is currently set-up and being evaluated in the Materials Science Laboratory, should allow immediate determination of the dislocation density of the ice samples. Not only will this prevent wasted trips to BNL, since all samples will be tested good beforehand, but it will provide a means for immediate feedback to the sample growth and preparation process. This should make the modifications to the current growth method much easier to accomplish.

Besides the above growth method other methods are also being evaluated for their suitability to grow heavily-doped single-crystal ice. Knight using a simple method involving an air pocket mechanism for pressure relief is growing ice single crystals 21 cm in diameter and as thick as 5 to 6 cm[6]. The conventional growth method of starting from a seed crystal is being examined along with a modified technique of Whitworth's where ice growth is started in a corkscrew-shaped device that "selects" a single crystal orientation for further growth[7]. Additionally, experiments that do not require as low a dislocation density as topographic experiments are being evaluated.

---

[5] Khusnatdinov, N. and Petrenko, V., *Express Method of Single Crystal Ice Growth for Pure and Undoped Ice I_h*, Physics and Chemistry of Ice, Ed. Maeno, N. and Hondoh, T., Hokkaido University Press, Sapparo, 1992, pp. 395-397

[6] Knight, C. A Simple Technique for Growing Large, Optically "Perfect" Ice Crystals, J. Glaciology, 1997, pp. 585-587

[7] Ohtomo, M., Ahmad, S. and Whitworth, R., *A Technique for the Growth of High Quality Single Crystals of Ice*, Journal de Physique, Colloque C1, Supp. 3, 48, 1987, pp. C1-595 - C1-598

These involve the mechanical testing of single crystal and polycrystalline ice doped with HCl and other impurities.

X-ray Topography of Notched Ice

X. Hu and I. Baker

Abstract

Cracking is a very important issue in Material Science and the study of the transition from brittle to ductile fracture of crystalline solids is one of the classical approaches to study cracking. Therefore, tremendous work has been devoted to observing and modeling the processes involved. In order to relate the macroscopic fracture behavior to a microscopic deformation mechanism, many theories seek to describe the brittle-to-ductile transition in terms of dislocation activity in front of a crack tip. In this talk, previous work on the x-ray topography of notched ice is reviewed. Study of the effect of crystal orientation on the dislocation structures in notched ice crystals under constant stress indicated that the dislocation/crack tip interaction mechanism depends strongly on the crystal orientation relative to the loading direction and the crack plane; study of the effect of temperature on the dislocation structures in notched ice crystals in constant strain rate tests has shown that there is far more dislocation activity around notches at high temperature (-7.8˚C) than at lower temperatures (-40˚C and -60˚C). The extension of the above temperature-effect study to the brittle to ductile transition in ice is discussed. New results from strain- controlled deformation tests, used to locate the brittle-to-ductile transition point for ice single crystals, are reported. Different test methods (such as load-controlled and strain-rate controlled tests) to carry out experiments on the X-ray topography of brittle-to-ductile transition in notched ice single crystals are discussed.

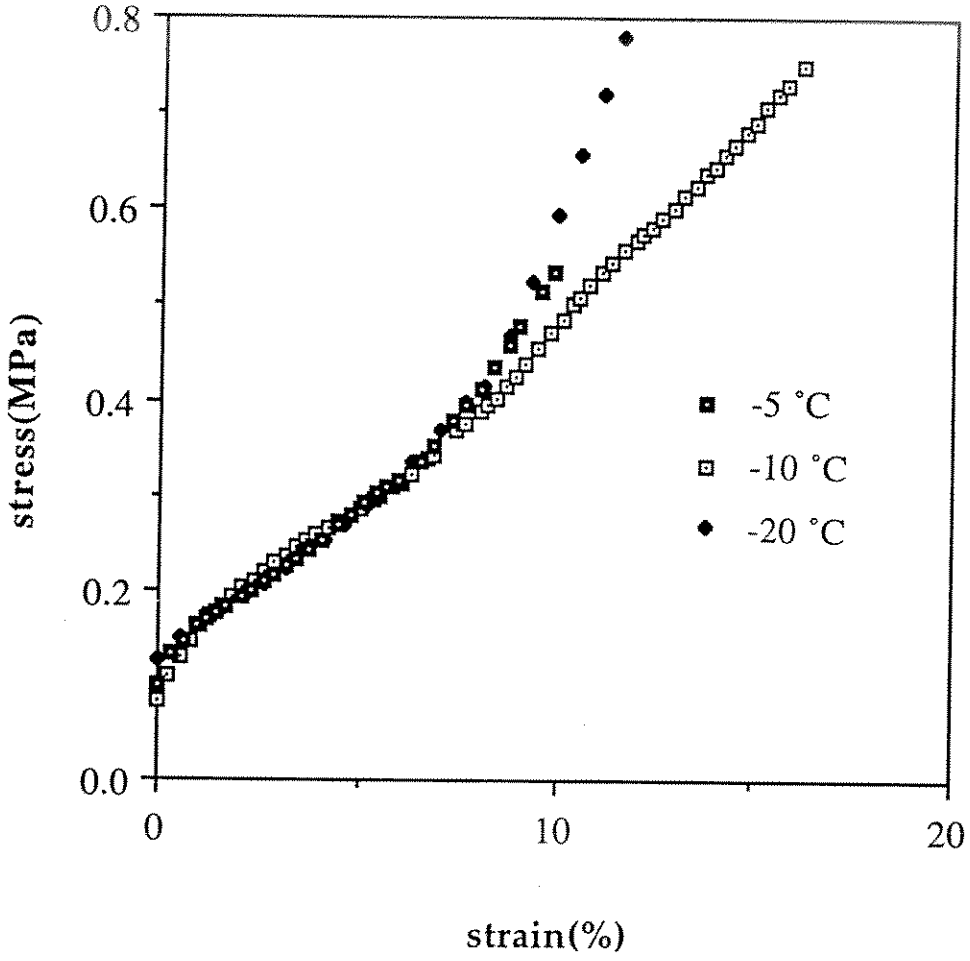

Stress_strain deformation curves of ice single crystals at a constant strain rate of 10^{-5}/sec under three different temperatures. For all the specimens here, cross section = 2 mm x 11 mm and the length is 21 mm.

Topograph at -7.8°C showing the dislocation configuration around the notch in an ice single crystal during *in-situ* deformation at a constant strain rate of 1×10^{-8} s^{-1}.

Study of Photoplastic Effect in Ice

by

Niyaz Khusnatdinov and Victor Petrenko

Thayer School of Engineering, Dartmouth College, Hanover, NH 03755

Abstract

The illumination of ice with UV light below 300 nm leads to its hardening [1], i.e. to the photoplastic effect. The observed change in the creep rate of different crystals of pure ice under UV illumination scattered from 60% to 0 %. The effect has reversible and irreversible components, and after a prolonged irradiation with an exposure of about 10^{-5} J/cm^2 at λ = 260 nm diminishes to zero. No change in electric conductivity is observed under irradiation.

This effect cannot be explained by the Glen's model [2], which was successfully used in case of doping with HF and HCl. Indeed, Glen supposed that proton disorder can be the obstacle for dislocation glide in ice, and the dislocation velocity should be proportional to the ice's high–frequency conductivity. In the experiments no photoconductivity (change of electric conductivity) was observed in the range of 185–300 nm, while the ice was hardening. That is in contradiction to the Glen's model. Thus, another mechanisms not related to the proton disorder should be involved.

This study is devoted to the investigation of the effect of oxygen dissolved in ice on the photoplastic effect. We found that oxygen enhances the photoplastic effect and may play a key role in its mechanism.

Experimental techniques

We have used pure, filtered deionized water from a "Milli–Q Water System," model ZD40 115 95 of Millipore Corp. The specific resistance of water was $\rho = 1.83 \cdot 10^7$ ohm·cm at room temperature. For doping of water we have used a pure grade of 30% hydrogen peroxide solution, H_2O_2. The crystals were first cut by a band saw and then thinned with a microtome.

The preliminary UV irradiation of ice samples doped with hydrogen peroxide, H_2O_2, was used to produce the oxygen dissolved in ice. The hydrogen peroxide H_2O_2 decomposes with the production of oxygen atoms and water molecules. The hydrogen peroxide concentration was determined by the calorimetric technique developed by Ghormley and described in [3]. The sensitivity of the method is $5 \cdot 10^{-8}$ mol/l. The concentration of oxygen accumulated in ice was estimated from the difference of the concentrations of hydrogen peroxide before and after the UV irradiation. A xenon lamp was used as a source and typical expositions varied from 1 to 24 hours.

Ice samples were deformed in the creep regime using a four–point bend deformation geometry (Fig.1) and under uniaxial compression (Fig.2), both under constant stress. Ice samples, 1x7x20 mm and 8x8x15 mm, were used for a four-point bending and for an unixial compression, respectively. Displacements were measured with a strain gauge with sensitivity of k = 0.25 μm/mV. A set of weights from 10 g to 2 kg was used to produce constant stress. All the measurements were performed at low strains $1\% < \varepsilon < 5\%$.

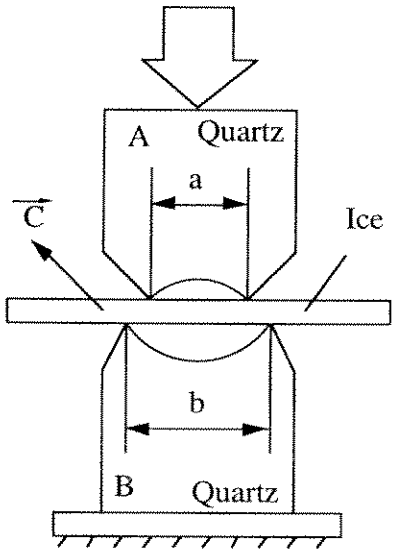

Figure 1. Experimental setup for four-point bending of ice samples: a = 9 mm, b = 15 mm, [1]. Ice samples of 1x7x20 mm were used.

For calculation of strain ε in a four-point geometry we used the following approximate expression:

$$\varepsilon = \frac{4 \cdot h}{b^2 - a^2} \cdot \xi \qquad (1)$$

where ξ is the displacement of the upper quartz plane, h is the thickness of a crystal (~ 1mm).

Two sources of light were used for excitation of photoplastic effect (PPE): the deuterium lamp, L2196 from Hamamatsu Corp., with a window that is transparent to UV

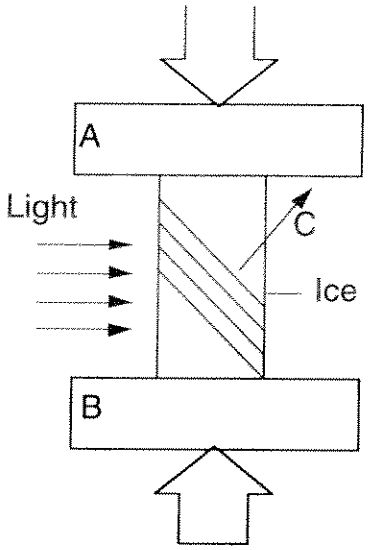

Figure 2. Setup for uniaxial compression. Ice samples of 8x8x15 mm were used.

light with a wavelength $\lambda > 160$ nm, and the 75Wt xenon lamp, model 6251, from Oriel Corp. Two optical filters were used with the transmittances at 180 nm and 240 nm.

Experimental Results.

Ice samples doped with hydrogen peroxide, H_2O_2, and subjected to the preliminary UV irradiation become harder. In other words, the larger stress is required to initiate the plastic deformation. We did not find any noticeable hardening of ice due to the doping by hydrogen peroxide itself. Thus, we relate the hardening to the oxygen accumulated in ice. Indeed, the longer ice samples were irradiated, i.e. the higher the concentration of oxygen in ice, the harder the ice samples became. At the same time the concentration of hydrogen peroxide diminishes. Figure 3 shows the dependence of the ratio of the initial strain rate to the applied stress vs. oxygen concentration in the ice samples.

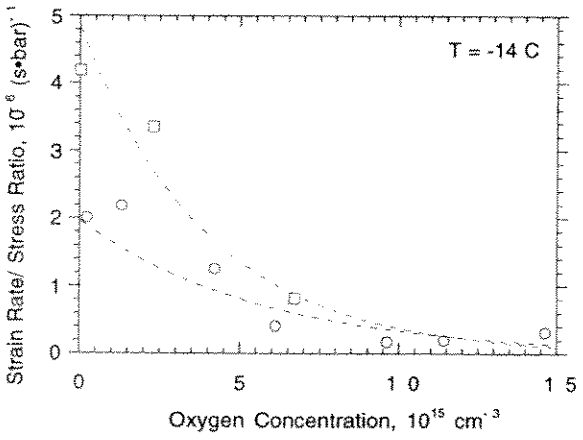

Figure 3. Dependence of the Strain Rate/ Applied Stress ratio on the oxygen concentration. Ice is doped with hydrogen peroxide. Four-point bend geometry results are shown by circles; uniaxial compression results are shown by square figures.

Figure 4 shows the dependence of the photoplastic effect, $\Delta\dot{\varepsilon}/\dot{\varepsilon}$, vs. the oxygen concentration in the ice samples. Here $\dot{\varepsilon}$ is the strain rate; $\Delta\dot{\varepsilon}$ is the change in the strain rate due to the UV irradiation.

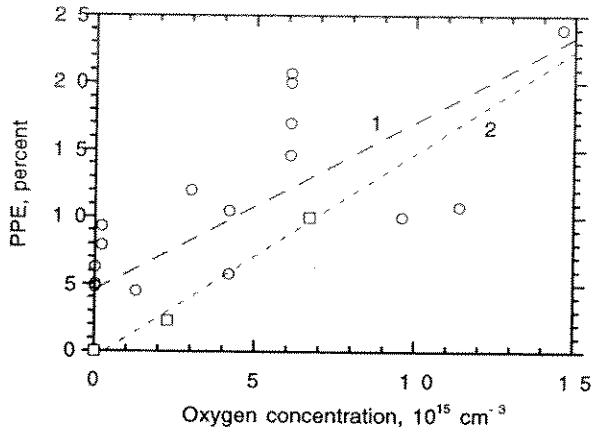

Figure 4. Dependence of the photoplastic effect on the concentration of oxygen dissolved in ice. Circles- four-point bend test; squares- uniaxial compression.

The higher the concentration of oxygen in ice the larger is the PPE. Four-point bend tests demonstrate significant data scattering. We relate this to the low accuracy of the four-point bend technique and to the non-uniform distribution of hydrogen peroxide in ice resulting in the non-uniform distribution of oxygen.

References

1. Khusnatdinov N.N. and Petrenko V.F., "Photoplastic Effect on Ice," Phys.Rev. Lett., **72**, 3363-66 (1994).
2. Glen J.W.,"The effect of hydrogen disorder on dislocation movement and plastic deformation of ice", Phys. Kondens.Materie, **7**, 43-51 (1968).
3. C.J. Hochanadel,"Effects of cobalt γ-radiation on water and aqueous solutions", J. Chem. Phys., **56**, 587-594 (1952).

FLOW & FRACTURE OF ICE ON SCALES SMALL AND LARGE

Erland M.Schulson
Thayer School of Engineering
3 June 1997

Is the behavior of small, laboratory-sized specimens related to the failure of floating ice sheets and other large,natural features?

In particular, does the crushing strength of ice decrease as the size of the feature or of the contact area increases?

The Observations

1. Kry (1981) measured penetration pressure during continuous crushing of S2 fresh-water ice sheets, in the lab and in the field, using indentors whose contact area varied over an order of magnitude.

He found that the high-speed crushing strength is lower by a factor of two (6 MPa vs 3.5 MPa) at the highest rate versus the lowest rate.

2. Iyer (1983) reviewed data from lab and field, including Arctic Petroleum Operators Association.

He noted that barring the possibility of an overriding influence of boundary conditions, the high-strain-rate compressive strength appeared to decrease with increasing size.

3. Sanderson (1988) plotted pressure-area data then available and noted that indentation pressure decreased with increasing area.

4. Tucker and Perovich (1992) and Richter-Menge et al. (1995) made in-situ stress measurements which indicate that the Arctic pack ice fails under compressive stresses considerably lower than in the lab.

5. Chen and Lee (1986) and Wang and Poplin (1986) reported the uniaxial compressive strength of first-year sea ice, in the field on large blocks (3 x 5 x 1 m) and in the lab.

They found that the strength of the larger blocks was indistinguishable from that of the smaller blocks, at $8 \times 10^{-5}\ s^{-1}$.

6. Kuehn et al. (1993) measured the compressive strength of ice cubes, 1cm on edge to 15 cm on edge.

They found that size had no effect at low rates where the ice is ductile. At high rates where the ice is brittle size again was not a factor provided the loading boundaries were flat. When bumpy, the larger cubes were weaker.

What do we believe?

-Kry studied transitional behavior.

-Iyer noted brittle behavior.

-Sanderson gave no description of behavior.

-Tucker-Perovich and Richter-Menge et al. note that the in-field stresses oscillate rather wildly, indicative perhaps of brittle failure.

-Chen-Lee and Wang-Poplin observed ductile behavior.

-Kuehn et. al found no effect when the ice is ductile.

Conclusion

Size is probably not a factor when ice is deformed slowly enough to allow creep deformation to impart macroscopically ductile behavior.

Size may be a factor when creep deformation is suppressed to the point that the ice exhibits brittle behavior.

****

"It seems like something is there, but we need to understand more about it." (Roy Johnson)

.